

Chapter 6

EXPERIMENTS ON BUBBLE CLOUDS CHARACTERISTICS

6.1 Experimental Equipment

Video imaging technique was employed in this study. The discussion in Chapter 4 proves that this technique is suitable for the measurement of bubble clouds in laboratory tanks and the photographs in Figure 3.9 made by Lamarre (1993) eloquently support this choice.

6.1.1 Wind-Wave-Current Research Facility

The experiments on bubble clouds characteristics were performed in the Wind-Wave-Current Research Facility in Air-Sea Interaction Laboratory. To prevent damage of the supporting instruments the tank is filled with filtered tap water to a depth of 0.75 m and an air column above of 55 cm. The tank has an effective length of 37 m from overall length of 42 m and width of 1 m (Figure 6.1a) . A wave-damping beach with a slope of 1/10 is located at the downwind end of the tank.

Figure 6.1 Wind-Wave-Current Research Facility in Air-Sea Interaction Laboratory.
Schematics of the water tank (a) and temperature control unit (b) .

The Facility comprises two flow loops: one is the wind tunnel above the water surface and the another is for the water circulation. A variable speed fan with a capacity flow rate of $567 \text{ m}^3 \text{ min}^{-1}$ generates wind with speeds from 1 to 18 m s^{-1} . Currents in the water from 1 to 32 cm s^{-1} are generated by a variable speed water pump with a capacity of $15 \text{ m}^3 \text{ min}^{-1}$.

The air and water temperatures can be independently changed and controlled from 5 to 40°C (Figure 6.1b) . Cold or hot mixture of water and coolant is circulated by pumps through a core pipe located in the center of the water circulating system, or through a serpentine located in the air temperature control unit. The necessary circulating system, for water or air, is chosen with a switch key and is set in open/close mode by an electromagnetic valve. The cooling of the core mixture is rendered by an air conditioning unit with a capacity of $9 \times 10^7 \text{ cal hr}^{-1}$. The heating of the core mixture is realized by boilers working on propane gas.

6.1.2 Photographic System

Video recording with digital image processing was the basic technique in this study. The bubble cloud dimensions along the tank – length and depth of penetration – are well revealed in a side view of the water body. The bubble cloud dimensions across the tank – width and length – are observable from a top view.

A 30 frames per second (fps) video camera (Burle TC355AC series) was used to track the bubble cloud once in a side and then in a top view. The camera

features: interline transfer CCD black and white imager with 768 x 494 active picture elements (pixels) in EIA RS-170 format; enhanced sensitivity for scene illumination as low as 0.1 lx at lens number f/1.4; variable speed electronic shutter providing time openings from 1/60 to 1/10000 s. In side view setup a second standard video camera (Panasonic AG-160) was employed with smaller field of view (FOV) in order to provide images of the individual bubbles within the cloud. The camera is with a 1/2-inch CCD sensor, a set of lenses from 9 to 54 mm providing power zoom 6:1, shutter speed of 1 ms, and minimum required scene illumination of 7 lx.

Bubble clouds were visualized on a color video monitor (Panasonic CT-1920M) . Images of bubble clouds were recorded on VHS video cassettes (JVC or Maxell) with a video cassette recorder (Panasonic NV-8350) . Proper illumination was provided by lamps, located differently for each, side or top, view.

6.1.3 Image Processing Acquisition

Images of interest were digitized with a frame grabber (Epix Inc., 4MEG VIDEO Model 10) and analyzed with a specialized image processing package (4MIP) . This frame grabber is a typical representative of current digitizing techniques. The board is installed in a single slot of a computer with a Pentium processor and PCI bus. Those are recent technological advances that has improved the data transfer speed of the new high level frame grabbers. However, 4MEG VIDEO does not use these advantages. It features the most common design with *on-board* image memory of 4 Mbytes which does

not allow transfer of data in real time. Instead, with this memory, 11 interlaced 752 x 480 pixels images can be captured at a time and then stored in the computer. A special feature of the frame grabber is the so called Horizontal Control Memory which allows the image memory to be configured by redistributing the memory in different number of buffers provided different image sizes. Non-interlaced format, giving each field of the image instead frame with time interval $1/60$ s, is also provided. In noninterlaced mode 23 buffers, hence images, are available for a sequential capturing, but at the expense of less vertical spatial resolution (752 x 240 pixels) . These 23 image buffers, used in a sequence, assure a time interval of only 767 ms to be digitized and/or displayed with video rate of 30 fps. Longer periods can be captured at the expense of time resolution (digitize each n-th frame) or spatial cropping (digitize a window from the whole image) . As it will be shown later (§6.4.3), the observed bubble cloud lifetime rarely exceeds 1 s, so that an appropriate image size, providing enough image buffers in a sequence, allows the whole process to be captured with the highest possible time resolution ($1/30$ s \cong 33 ms) . Therefore, the major limitation of the board can be overcome.

All specialized 4MEG VIDEO features are realized and controlled by an interactive imaging software named 4MIP. The work with this package requires the usage of two monitors. One monitor is that of the computer which displays the menus of the software, another monitor is necessary for image display. In this study the images were displayed on a black&white video monitor (Sanyo VM 4209) . In the mode of digitizing images from the video cassettes a third video monitor, mentioned in §6.1.2, was a necessity. The software provides image processing functions as simple as these for

image examination (e.g., zooming), morphological functions (dilation, erode), and advanced special procedures such as filtering, FFT, convolution. Special measurements as subpixel measurements, size measurements by rulers, blob analysis are also provided. The image processing can be facilitated and accelerated by using macros – a sequence of commands necessary for the accomplishing of a given task. To summarize, the frame grabber is completely capable of meeting the analysis requirements for this study.

6.1.4 Auxiliary Instrumentation

The wind velocity was monitored with a pressure anemometer (Pitot tube). The probe consists of two concentric tubes pointed in the air flow (Dobson et al., 1980). The inner tube has a small dynamic pressure port at the end, while the outer tube is closed at the end and has a ring of small static pressure ports a short distance back. The pressure and velocity are related by Bernoulli's equation. The readings of the instrument (the heights of a viscous liquid in a U-shaped capillary) for wind speeds from 9 to 16 m s⁻¹ were calibrated in a small reference tunnel with air flow controlled by a variable speed fan. Because of its simplicity and lack of moving parts, this anemometer is known for its reliable maintenance of the calibration. Indeed, during the experiments the readings showed excellent repeatability. In order to prevent blocking of the ports by moisture, even flying drops at high winds, the probe was located at fetch shorter than the actual measurements (12 m) and a bit higher than the middle of the wind tunnel. This installation introduces negligible error (< 1%) in wind speed measurements since the

design of the instrument tolerates misalignment from the average wind path up to 17° (Dobson et al., 1980) .

Three-minute wave gauge records were made for each of the six experiments (two different camera views for three different water temperatures) for each of the eight wind speeds. The wave characteristics were derived from the time series of a fluctuating voltage recorded with a capacitance wave gauge. The device consists of a tantalum wave height sensor and a wave gauge electronic package. The tantalum wire sensor has a tantalum oxide coating (Ta_2O_5), which is a good insulator with a high dielectric constant. The tantalum wire (metal), tantalum oxide (dielectric) and the water form a capacitor which translates by a frequency–voltage detector the water surface fluctuations into a fluctuating voltage. The sensitivity and linearity of the device depend strongly on the coating quality: it should be very thin and uniform. The effects of surface wetting and meniscus on the sensor response are also important as they tend to reduce the frequency response. Those effects are relatively small for the tantalum oxide coating. The output of the wave gauge was digitized by a 12-bit analog-digital converter (ADC) and furnished to a computer. The dynamic range and sampling frequency can be controlled by a software written in the laboratory. Those were set to ± 10 V and 100 Hz, respectively. With this sampling rate (10 ms) the ADC memory (2000 points) was full for 20 s and the

data transferred into the computer. Thus, nine cycles each of 2000 points were done for the three-minutes records and time series of 18000 points for each wind speed were

stored in a binary file for later processing. Calibration of the sensor was performed at the beginning and at the end of each of the six experiments. Each calibration line gave transformation coefficient, in cm V^{-1} , using voltage averaged from the before and after experiment readings. Constant visual control of the surface elevations during the experiments was provided by an oscilloscope.

6.2 Experimental Conditions

The bubble clouds in side view were well visualized by a 500-W lamp shining from above through an opening in the middle of the tank cover into the water body. The length of the illuminated area was roughly 1.2 m along the tank and the width across the tank was around 70 cm. In this way the bubble clouds formed at the tank walls were shadowed and appeared gray in the images, thus they were easily distinguished from those formed in the central part of the water by intensity. The frequent generation of large bubble clouds at the tank walls when such are not present in the middle can be explained with the theoretical consideration proposed by Longuet-Higgins (1990) . He showed that, surprisingly at first glance, the waves near the wall may be significantly steeper than those along the center line, by a factor of $2^{1/2}$. Hence, they may break and produce bubble clouds even at conditions that are not suitable for this process in the middle of the channel. The bubble clouds in a top view were illuminated by a 600-W lamp located next to the tank wall and lower than the water surface. In this way

reflections from the water surface were avoided and only bubbles, reflecting specularly, were bright in the images.

The cameras' settings were adjusted for best size of the FOV and best contrast by several trials and image digitizing. The side view camera with large FOV (Burle) used a lens with focus length of 12.5 mm and an aperture of 5.6. Sharp focus at the middle of the water body was obtained at a distance of 0.35 m. A working distance (the distance between the tank wall and the rim of the camera lens) of 1.145 m provided horizontal and vertical scales of 1 mm pxl^{-1} and 2.5 mm pxl^{-1} , respectively. Therefore, the FOV covered with the camera's sensitive area was 76.8 cm x 61.8 cm. The camera was positioned at water surface height and perpendicular to it.

The side view camera with small FOV (Panasonic) used focus length of 50 mm focused at the middle of the tank at distance 1.2 m. The small FOV (14 cm x 11 cm) was obtained at working distance 72 cm. The camera was a bit lower than the water surface level and looked at the individual bubbles within the cloud slightly from below. This was dictated by the desire the camera with small FOV to look at the same place as the side view camera with large FOV and at the same time not to obstruct its view. The difference in the perspective was large enough to reach this goal but small enough not to change the bubbles sizes significantly.

In top view setup the camera with focus length of 12.5 mm was again used (Burle) with best focusing on the water surface at distance of 0.35 m and aperture of 5.6. The camera looked down vertically towards the water. A working distance (from the

tank cover to the lens' rim) of 94.2 cm assured a FOV on the tank cover with size 42 cm x 36 cm. The perspective projection of this FOV 57 cm down provided an actual FOV on the water surface of 67 cm across the tank and 58 cm along the tank. The size across the tank matched well the width of illuminated area (70 cm) in side view and hence provided credible values for the bubble cloud width. The size along the tank is somewhat short, i.e., the cloud length, especially at higher wind speeds, cannot be extracted from the top view images but only from those in side view. However, this length was not critical for tracking the temporal evolution of cloud width from above.

For all records both cameras were set at 1 ms shutter speed. Preliminary experiments had shown that this shutter speed effectively freezes the fast moving object within the scene. Table 6.1. gives a summary of the parameters mentioned above.

Table 6.1

Parameter Camera	Side view, large FOV Burle	Side view, small FOV Panasonic	Top view Burle
focus length mm	12.5	50	12.5
focus distance m	0.35	1.2	0.35
aperture	5.6	Auto	5.6
shutter speed ms	1	1	1
working distance m	1.145	0.72	0.94
inclination angle	0°	< 5°	90°

Records were made for wind speed from 9 to 16 m s⁻¹ at three different water temperatures (13, 20 and 27°C) . The fetch of 26 m was enough long for the waves

to grow and break frequently in the FOV of the cameras. In order to extract statistically sound data, bubble clouds were imaged for 15 minutes for each wind speed. A set of three video cassettes, two for side view (large and small FOV) and one for top view, at each water temperature is provided. Overall, nine video cassettes with data on bubble clouds are available. Initially the water depth was set to 73 cm in order to avoid instruments' wetting, especially at high wind speeds. During the heating of the water to 27°C the depth dropped to 72 cm since enhanced evaporation took place due to intensified condensation of water vapors on tank walls, and consequent decreasing of humidity. Similarly, during the cooling of the water to 13°C, the depth decreased to 71 cm due to increased evaporation. To have the water surface tension unchanged, no water was added. A summary of the experimental conditions is given in Table 6.2.

Table 6.2

Water Temperature °C	Camera FOV	Wind speeds m s^{-1}	Record min.	Surface Tension mN m^{-1}	# of video cassettes
13	side large	9, 10, 11, 12, 13, 14, 15, 16	15	74.79	1
	side small		15		1
	top		15		1
20 (room)	side large	9, 10, 11, 12, 13, 14, 15, 16	15	72.75	1
	side small		15		1
	top		15		1
27	side large	9, 10, 11, 12, 13, 14, 15, 16	15	72.09	1
	side small		15		1
	top		15		1

6.3 Data Processing

6.3.1 Digitizing

Sequences of images from side and top views were digitized in noninterlaced mode, i.e., fields were captured instead of frames with time interval of 1/60 s. However, the digitizing period (an input parameter in the software which was set to 2) provided each consecutive frame (1/30 s time interval) from the video.

From the large FOV imaged by the camera in side view (76.8 cm x 61.8cm) a window of 672 x 150 pixels was cropped and digitized. With horizontal and vertical scales of 1 and 2.5 mm pxl^{-1} , respectively, the physical sizes of the window are 67.2 cm x 37.5 cm. The later was chosen by two considerations: 1) to cover the cloud size displayed on the monitor, while the pixels beyond the monitor size in horizontal direction and noninformative pixels in vertical direction be disregarded; 2) to allow sequences of 41 images to be captured, which in all cases was more than enough to register the entire cloud lifetime. There was some trade off using FOV of 67.2 cm x 37.5 cm. On the one hand, the horizontal size covered one wavelength for winds up to 11 m s^{-1} , and about 80% of the wavelength for higher wind speeds. This was limitation for viewing the whole cloud length only in some cases. On the other hand, larger FOV would give very coarse scales in both directions which would influence the accuracy in determining the cloud parameters. Indeed, the photographs shown by Koga (1982) of bubble clusters at 16 m s^{-1} wind speed in laboratory tank have a FOV enough big to cover about one and half wave length, however the clouds (clusters) even at this high wind

speed are evident as streaks; only qualitative conclusions can be made from these photographs as the quantitative results would be very crude.

The images in top view were digitized in a window of 672 x 240 pxl (equivalent to FOV of 69 cm x 57 cm with horizontal and vertical scales of 1.03 mm pxl⁻¹ and 2.4 mm pxl⁻¹, respectively) . This FOV used all available vertical pixels and discarded the pixels beyond the monitor size in horizontal direction. Sequences of 26 images were available, which again assured the bubble cloud width to be traced from its appearance in the FOV to its almost complete decaying or at least to the moment when meaningful values can be extracted.

Close observations of the video records show that although there are many bubble cloud events, it is not easy to chose and digitize an event qualified for analysis. In side view records, the event may start out of the camera FOV and only the later stages of the process to be available, and vice verse, the event may start somewhere in the middle of the FOV and only the beginning to be observable. It was possible to track the whole process only if the event started at the most right edge of the FOV. Frequently large “beautiful” clouds formed at the walls hid the clouds formed behind, at the middle of the tank. Fortunately, the two types of clouds were distinguishable (see §6.2 and an example in Figure 6.2a) and these cases were not digitized. Another interesting observation concerns the position of the water meniscus at the front wall. When the meniscus was low the wavy surface was evident as if from above. The clouds protruding in the water though well evident were masked from the water surface in their upper side

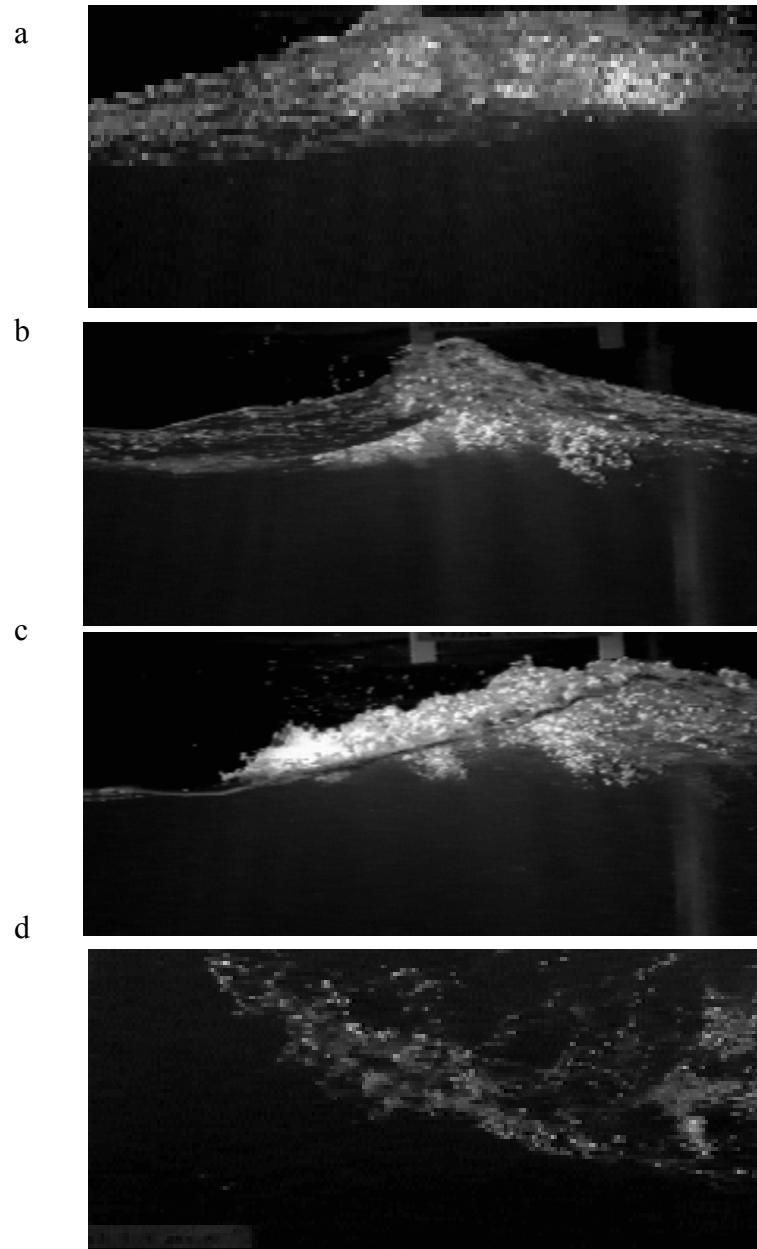


Figure 6.2 Choice of an image qualified for analysis; examples of: a) overlapping of a cloud formed in the middle of the channel by a cloud formed on the tank wall — gray patches over the bright cloud; b) hiding the upper part of a cloud by the low position of the water meniscus; c) cloud qualified for digitizing and further analysis; d) cloud in top view coming from right.

(e.g., Figure 6.2b), which would mislead the length and penetration depth values. These cases were also not digitized. The cloud was well revealed only when the view angle was as if from below, i.e., the meniscus was at high position. Such appearance of a bubble cloud, appropriate for digitizing and further analysis, is shown in Figure 6.2c. In top view records observations were similar. In order to track the entire process the cloud should appear in the upper edge of the FOV and approximately parallel to it. The events for which the cloud appeared somewhere from left or right (Figure 6.2d) were excluded from consideration because they might be caused by reflections from the walls. In addition, it turned out that at high wind speeds ($>13 \text{ m s}^{-1}$) however large the FOV in horizontal direction was, it was not enough to accommodate the entire cloud width. Actually, at high wind speeds the entire width of the tank would be not enough as the cloud would spread until it reached the walls and would stay restricted in this size by them. Hence, it would be true to say that from some point on the cloud width was equal to the FOV horizontal size and remained with this or wider size until decay started. This restriction could not be avoided for high wind speeds. Thus, there are such images occupying several frames in the top view sequences for high winds.

From the small FOV, sequences of images with temporal evolution of bubble clusters in a close view were digitized for wind speeds 10, 13 and 16 m s^{-1} . The entire sensitive area imaged by the camera was digitized (752×240 pixels) which, with a scale values of 0.3 and 0.77 mm px^{-1} in horizontal and vertical directions respectively, gave a FOV of $22.56 \text{ cm} \times 18.48 \text{ cm}$.

6.3.2 Parameters to be Determined

The clouds projected below the water surface are considered in the study. In the side view images, a convenient guide for separating the bubbles in the water and the foam on the surface is the meniscus formed on the front tank wall usually seen as a sharp dark line. As the waves in water channels are very close to two-dimensional, the meniscus delineates the wave profile at any position inside the tank closely and this allows the cloud to be tracked relative to the wave phase. The distinguishing of the bubbles below the water in top view images was assured by the lighting (see the beginning of §6.2) .

The parameters necessary to be determined are bubble cloud dimensions – length, l , depth of penetration, d or h , width, w – and void fraction, α_{side} or α_{top} . Temporal and spatial evolutions of these parameters are of interest. The brightest object in the image in Figure 6.3a is the bubble cloud seen from a side view. The observable parameters are depicted. The bubble cloud length, l , is defined as the distance between the vertical lines passing through the left and right cloud edges. The bubble cloud penetration depth can be defined either as the distance from the highest to the lowest edges of the cloud, which can be also called cloud thickness, d , or from the still water level (swl) to the lowest point, h . The terms “penetration depth” and “cloud thickness” are used interchangeably for the parameter d throughout the text. The bubble cloud void fraction from side view, α_{side} , is defined as the ratio of the bright pixels (representing the air) to all pixels (representing the mixture of air and water) within the cloud volume. In the images the cross section of the cloud volume is seen. It is irregular in shape and can be traced with a

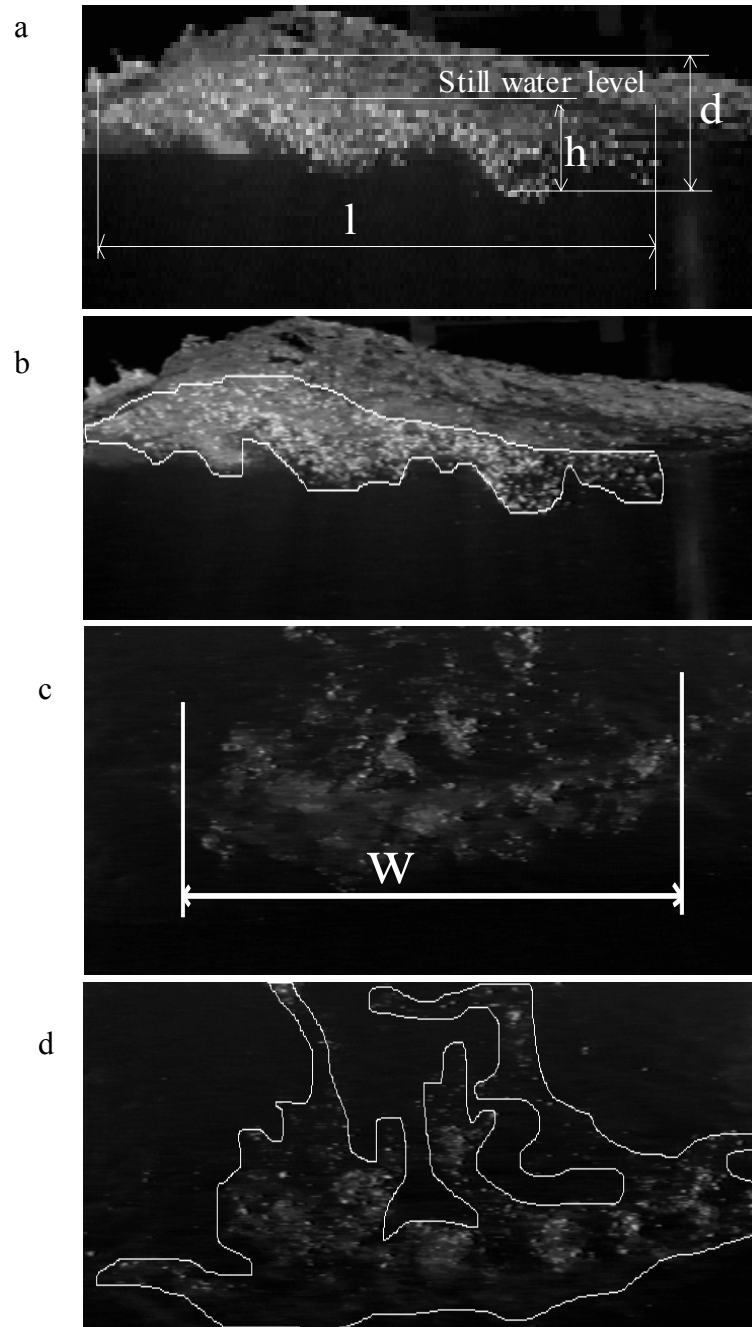


Figure 6.3 Definition of the bubble cloud parameters: a) parameters observable in side view: length (l), thickness (d), penetration depth (h); b) cloud volume in side view traced with free-hand drawing; c) cloud width (w) from top view; d) cloud volume in stop view traced with free-hand drawing.

freehand drawing in the image software (Figure 6.3b) . The irregularity of the cloud shape and its overlapping on the wave, also bright in the images, raise the question of the repeatability of this freehand drawing. Two rules are proposed and the experience shows that if they are followed the cloud can be framed with more than 99% repeatability by one or another operator. These are: 1) the cloud is represented by the brightest pixels below the meniscus; and 2) the bubbles within the cloud, i.e., the bright pixels, should be *homogeneously* distributed. For example, a group of two – three bubbles (bright pixels) could not represent homogeneous mixture and they should be dropped from consideration. Such cases were encountered usually in the latest stages of the cloud lifetime when most of the bubbles disappeared but a few lasted giving a notion of a plume. The operator's subjective decision to drop those plumes or not introduces an error less than 2%.

The bubble cloud width, w , is defined from top view images (Figure 6.3c) as the distance from the most left to the most right edge. The bubble cloud void fraction from top view, α_{top} , is defined similarly to the side view case: the ratio of the bright pixels to all pixels within the cloud volume, whose irregular shape is traced by freehand drawing (Figure 6.3d) .

For the size distributions of the bubbles within the cloud the parameters necessary to be determined from the images were: the number of bubbles in the measuring volume; their position, for possible determination of the vertical distributions, i.e. the distribution of bubbles in depth; and the major axis of the ellipsoids representing the bubbles for calculating their equivalent diameter.

6.3.3 Procedures

The procedures necessary for a complete analysis of the data include obtaining the wave field characteristics from wave gauge measurements, extraction of bubble clouds and bubbles parameters' values from the digitized images and statistical approaches for analyzing these values.

6.3.3.1 Wave Field Characteristics

Time series of a fluctuating voltage giving the water surface elevation changes were recorded with a wave gauge (§6.1.4) for 3 minutes in each experiment. Binary files were processed in Matlab. The long time series (18000 points) were divided in 18 shorter ones, each of 1000 points. For each of this 18 series the power spectra were calculated with Fourier transformation, then the 18 spectra were averaged. The peak of the averaged power spectrum is reported as the dominant wave frequency, f (Hz), and used to find the dominant wave period T (s) . Finally, the wave length L (m) and phase velocity c (m s^{-1}) were calculated with the dispersion relation: $L = gT^2/2$ and $c = L/T$. In addition, the time series were used to find the significant wave height, H_s (cm). This was calculated as the average of the 1/3-d highest waves amplitude.

6.3.3.2 Bubble Cloud Parameters

Once sequences of bubble clouds from side and top views were digitized and stored in the computer, extraction of the clouds parameters' values from each image was pursued. The procedures for both type of images, from side or top view, were similar and followed the steps illustrated in Figure 6.4. First, from the raw images (Figure 6.4a) an initial FOV (Figure 6.4b) without bubble clouds was subtracted in order to remove the background lighting; this improved the contrast of images (Figure 6.4c) . Then, a rectangular window circumscribed the cloud and its horizontal and vertical coordinates of the upper left and lower right corners were used to calculate the parameters l , d , and h or w in top view images (Figure 6.4d) . Next, the irregular shape of the cloud was delineated by a freehand drawing and all pixels within counted (Figure 6.4e) . The same contour was used for second counting, this time of the pixels with intensity higher than a threshold. The ratio between the values resulting from the two countings gave the void fraction (from side or top view) . The intensity threshold (10 arbitrary units) was chosen enough low to count even faint pixels representing the very small bubbles or these deep in the water volume. In some occasions this threshold was not enough high to reject the intensity of the wave laying behind the cloud, hence, some overestimation of the bright pixels number occurred. However, since the cloud/wave overlying area was usually less than the remaining cloud area, this overestimation introduced less error (5%) than would introduce the underestimation of the bubbles with low intensity (up to 50%) . Finally, the extracted data were written in a file for further calculations, statistical analysis and/or graphing.

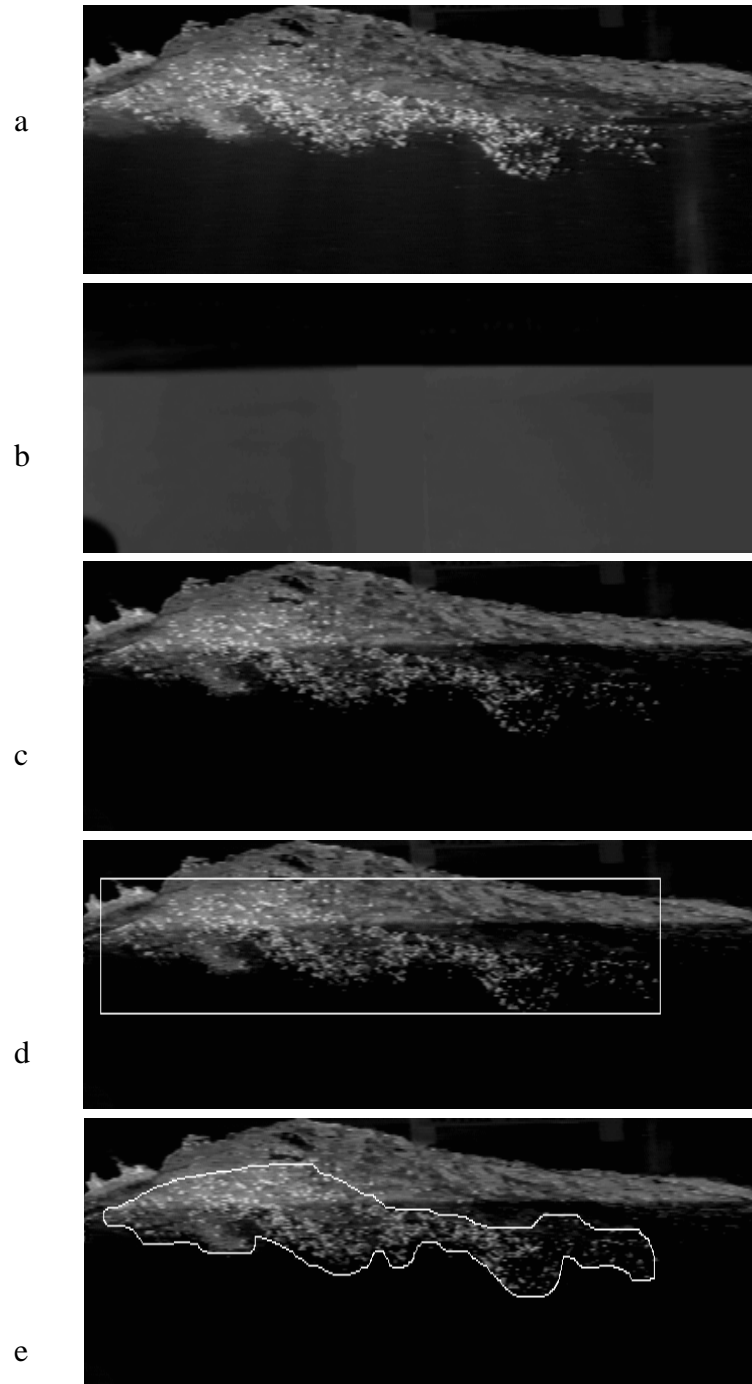


Figure 6.4 Procedure for cloud parameters extraction: a) raw image; b) initial FOV; c) image with subtracted initial FOV; d) rectangle window for l, d, h; e) cloud volume.

For the bubble size distributions one sequence was considered for each wind speed. Three images separated by time interval $(2 - 3)\Delta t$, $\Delta t = 33$ ms, were used from each sequence. In each image bubbles were counted, and their coordinates and major axes were extracted with a command “Blob analysis” available from the imaging software. The bubbles’ equivalent diameter, d , was determined using the horizontal, x , and vertical, y , axes of the ellipse, by setting its area $(= \pi xy/4)$ equal to the area of a circle and calculating an equivalent diameter, $d = (xy)^{1/2}$, for each bubble (Kalvoda, 1992). Then the number of bubbles $N(d, \Delta d)$ with a diameter d in a band $[d, d + \Delta d]$, where $\Delta d = 450 \mu\text{m}$, over the range 1 to 10 mm was found. The bubble size distribution was calculated from $N(d, \Delta d)/(\Delta d \cdot V)$, in $\mu\text{m}^{-1} \text{m}^{-3}$. The measuring volume, V , was calculated from the area of the FOV and the focus depth (Geißler and Jähne, 1995). As the maximum size of a bubble diameter observed was about 10 mm, the focus depth was taken to be 20 mm. The probability density was found by normalizing the bubble distributions with the total number of bubbles in a cubic meter (Wu, 1988a).

6.3.3.3 Statistical Approaches

The bubble cloud production is a random process in both time and space, hence cloud parameters are random variables. Moreover both, the process and variables, are nonstationary. Therefore, the conventional statistical techniques and formulae do not apply for such data and special considerations and procedures are required.

Bendat and Piersol (1966) outline some of the possible approaches for dealing with nonstationary data, though a totally adequate methodology does not exist. Usually the characterization begins by studying the type of nonstationarity. Three basic types representing physically occurring nonstationary data are time-varying mean value, time-varying mean square value, and the combination of these two. The case in hand represents the third type: combination of time-varying mean and mean square value. The probability structure of nonstationary data is characterized with probability density function (PDF), as for the stationary case, however the random variables (the cloud parameters in particular) and the formulae are time dependent. The most rigorous way to find the mean value of nonstationary data is to determine an ensemble average at a fixed moment over N time-varying records, each consisting of M points, by adding them and dividing by N . The estimation of the mean differs over different choices for these N records and large number of records are necessary to reduce the estimation error to an acceptable level.

The time varying records in this study represent the temporal evolution of cloud parameters depicting the appearance, growth and decay of the cloud. It is discussed later (§6.4.4) and illustrated in Figure 6.5a, that the time span of different cloud events varies, thus the realizations with parameter values have different lengths: some may have $M = 12$ points, others reach $M = 33$ points. This, unfortunately, means that the procedure of ensemble average proposed by Bendat and Piersol (1966) can not be applied so that special approaches should be considered. In the hunt for best statistics of cloud parameters three methods are tried.

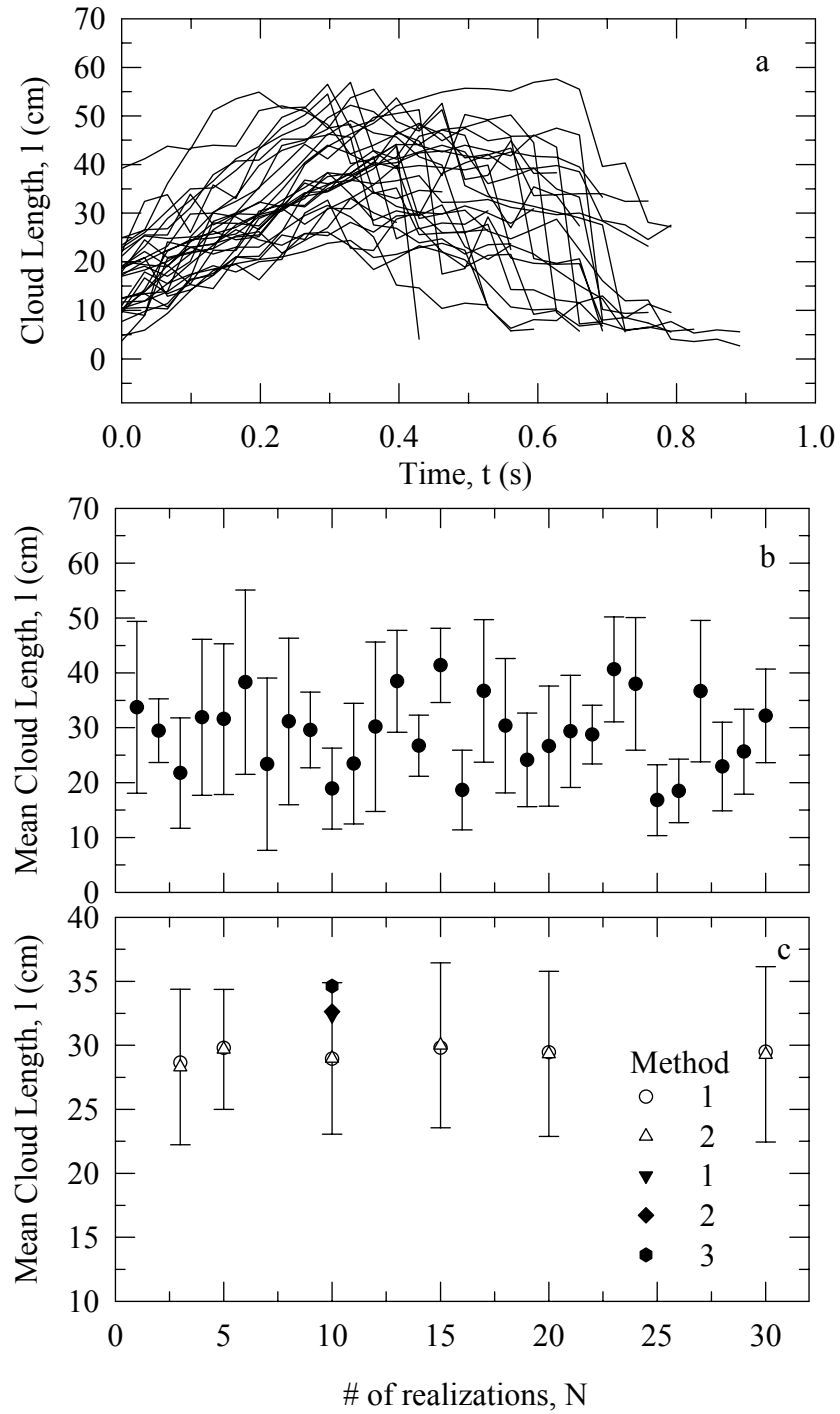


Figure 6.5 Illustration of the second averaging method (the example is for the bubble cloud length, l , wind speed 13 m s^{-1}): a) time evolutions of 30 events; b) the means of the 30 realizations; c) the means obtained by three methods (solid symbols) and from different number of realizations (open symbols) .

In the first method the values for a given cloud parameter from several realizations are piled in one long realization and the PDF, mean and variance of this realization are found. Some mean value found for each parameter is considered as a generalizing number for this parameter which can be assigned for a given wind speed. The PDF gives an idea for the probability with which the registered parameters will assume values within some defined ranges. For each parameter the range of values (from minimum to maximum) was divided in 12 bins, which for l gave approximately a bin of 5 cm, for d – 1 cm, for h – 2 cm and for w around 5 cm.

In the second method the mean and variance of each of several realizations with the values for a given cloud parameter are found. A new realization is formed from these means and its mean and variance calculated. Figure 6.5b shows the realization of 30 cloud length means with their variances (the bars in the figure) obtained for each individual cloud length time evolution plotted in Figure 6.5a. The trials of this procedure for different number of realizations ($N = 3, 5, 10, 15, 20$ and 30) showed that the mean of the realization of means is quite stable (open triangles in Figure 6.5c). The figure illustrates the fact that if the means of three or thirty time records are used, respectively the realization of means has 3 or 30 points, the resulting means differ at most 6%. In Figure 6.5c the means from different number of realization N obtained by the two described methods are compared (open circles for method 1 and open triangles for method 2). The error from method to method at a fixed N is at most 1% (the biggest difference between the means is for $N = 3$). The same trials for the other cloud

parameters (d , h , α_{side}) returned similar results. This consideration gave confidence to the decision that all statistical values for cloud parameters be obtained from $N = 10$ time evolutions. So, from the 30 realizations archived for wind speed 13 m s^{-1} ten were selected for deriving the ultimate mean values and comparing them with those for other winds. The means obtained with the two methods from the new combination of ten realizations are compared with these from the initial combination in Figure 6.5c (the solid diamond and inverted triangle) . While the means for bubble cloud length from the initially used 10 realizations is around 29 cm, the means obtained by applying the both methods to the new set are around 32 cm, i.e. 10% bias. The reason is that the newly selected realizations were not drawn completely arbitrarily. The realizations showing extremely strong oscillations for some of the parameters due to intensity instability when the bubbles went in and out of the illuminated area were avoided. That is, the clouds well revealed in the FOV from the beginning to the end of the process were considered. It is believed that this selection is justifiable as only about 15 % of the realization showed such instability.

In the third method the parameter values observed for several time realizations are sorted according their relevance to the wave phase and the mean of each “phase” group is found. The generalizing number for a given wind speed is the mean of those several ‘phase’ means. The trial of this method on the 10 newly selected realizations for 13 m s^{-1} -wind gave the most deviated mean (the hexagon in Figure 6.5c), yet the bias is not dramatic (17%) .

The sorting in the third method was used to establish the changes of the cloud parameters relative the wave phase which gives a notion for their spatial evolution. The bubble clouds usually appeared at the front wave slope. Using the wavelength of the dominant wave for a given wind (Table 6.3) and the physical size of the FOV (67.2 cm) it was estimated that the place of the cloud generation relative the wave phase is around $\varphi = 45^\circ$ (the wave crest is chosen as a reference point and is accepted to be at $\varphi = 90^\circ$). For example, at wind 10 m s^{-1} the clouds are mostly generated at $\varphi = 45^\circ$, while at 16 m s^{-1} wind the wave phase is approximately at 33° . The cloud images in one sequence were roughly separated in six groups. The groups, each covering 45° , are centered at $\varphi = 45^\circ$, 90° , 135° , 180° , 225° , and 270° and represent specific wave phases that can be illustratively called “before the crest”, “beneath the crest”, “back of the crest”, “passing the zero”, “before the trough”, and “the trough”. Usually 2 - 3, occasionally 5, cloud images from one sequence were assigned for one ‘phase’ group. It seems fair since it is evaluated (with the dominant wave period and the time interval of 33 ms) that from frame to frame the wave phase changes with about 16° , so that for three images the wave phase would cover 45° . For each parameter (l , d , h , or α_{side}) the values for ten time evolutions were sorted in this way and the mean and variance of each group were found. The trend of these means with the wave phase ultimately yields the spatial evolution.

6.4 Results and Discussion

6.4.1 Wave Characteristics

The averaged power spectra of the water surface for wind speeds 10, 12, 13, 14, and 16 m s⁻¹ are plotted in Figure 6.6a. With increasing wind speeds the spectral peak moves toward lower frequencies as the waves become longer and more energetic. The surface elevation power spectra for the experiments with side and top views for 13 m s⁻¹ wind are compared in Figure 6.6b. As expected, the repeatability of the wave field, revealed from the coincidence of peaks, is remarkable. The differences at low frequencies are due to nonstationary processes in the tank with a time frame of order of a few seconds, thus much slower than the studied events. In Figure 6.6c the wave spectra at 13 m s⁻¹ and three different water temperatures are compared. The place of the frequency peak, hence dominant wave period and length, does not change with temperature: at high wind speeds ($> 10 \text{ m s}^{-1}$) the temperature has little effect on the wave field. The wind dependence of all wave characteristics (f , T , L , c , and H_s) is documented in Figure 6.7 a - e, respectively. With the frequency peak moving to lower values (Figure 6.7a), the wave period T (Figure 6.7b), the wave length L (Figure 6.7c), and phase velocity c (Figure 6.7d) slightly increase. The significant wave height H_s increasing is the most noticeable change brought by the wind (Figure 6.7e). The wave characteristics for different wind speeds and water temperature of 20°C are listed in Table 6.3.

The probability density of the wave amplitude for non-breaking waves is given by the Rayleigh distribution (Longuet-Higgins, 1975; Walker, 1994). Indeed, the

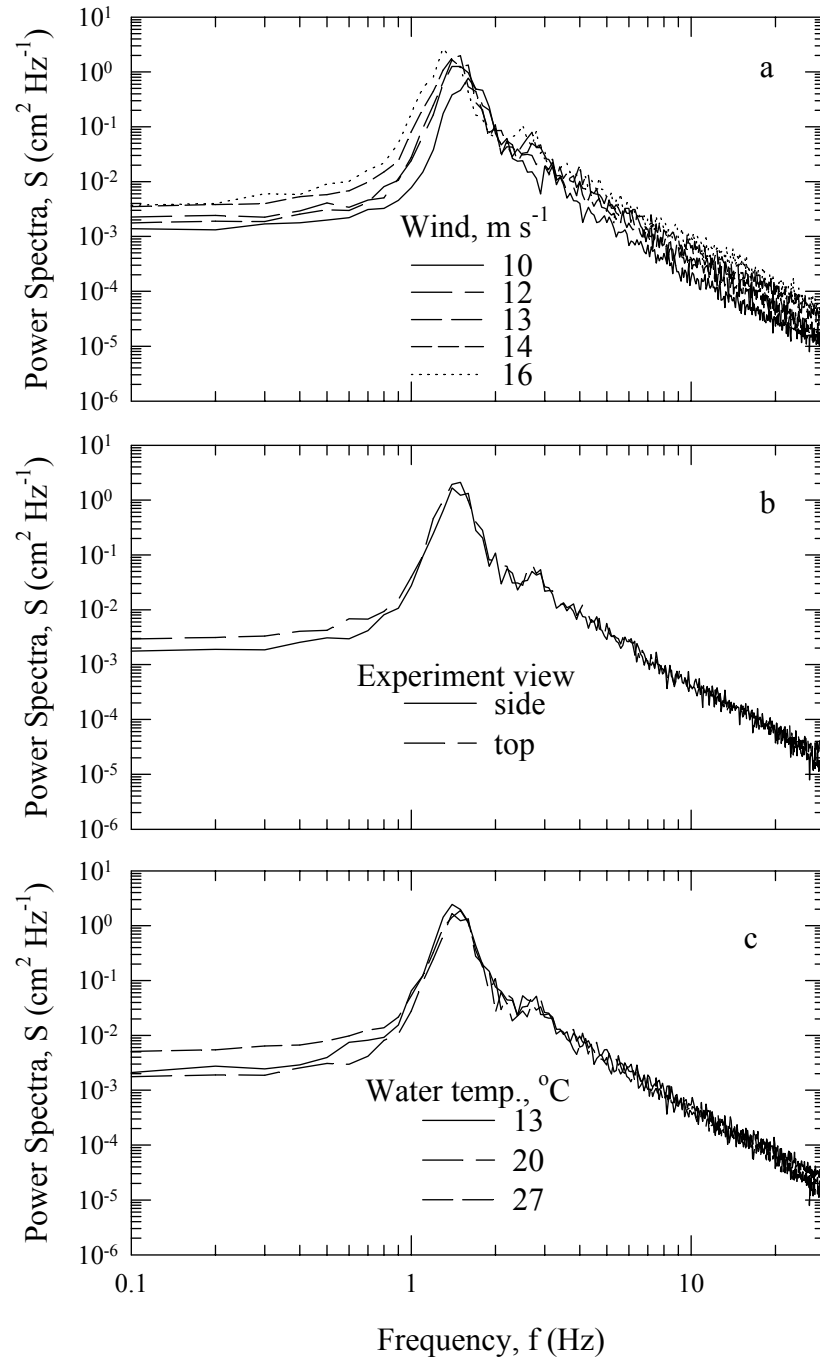


Figure 6.6 Power spectra of surface elevation: a) wind speeds from 9 to 16 m s^{-1} (side view, water temperature 20°C); b) spectra for the experiments with side and top views (wind 13 m s^{-1} , water temperature 20°C); c) spectra at different water temperatures (wind 13 m s^{-1} , side view, air temperature 20°C).

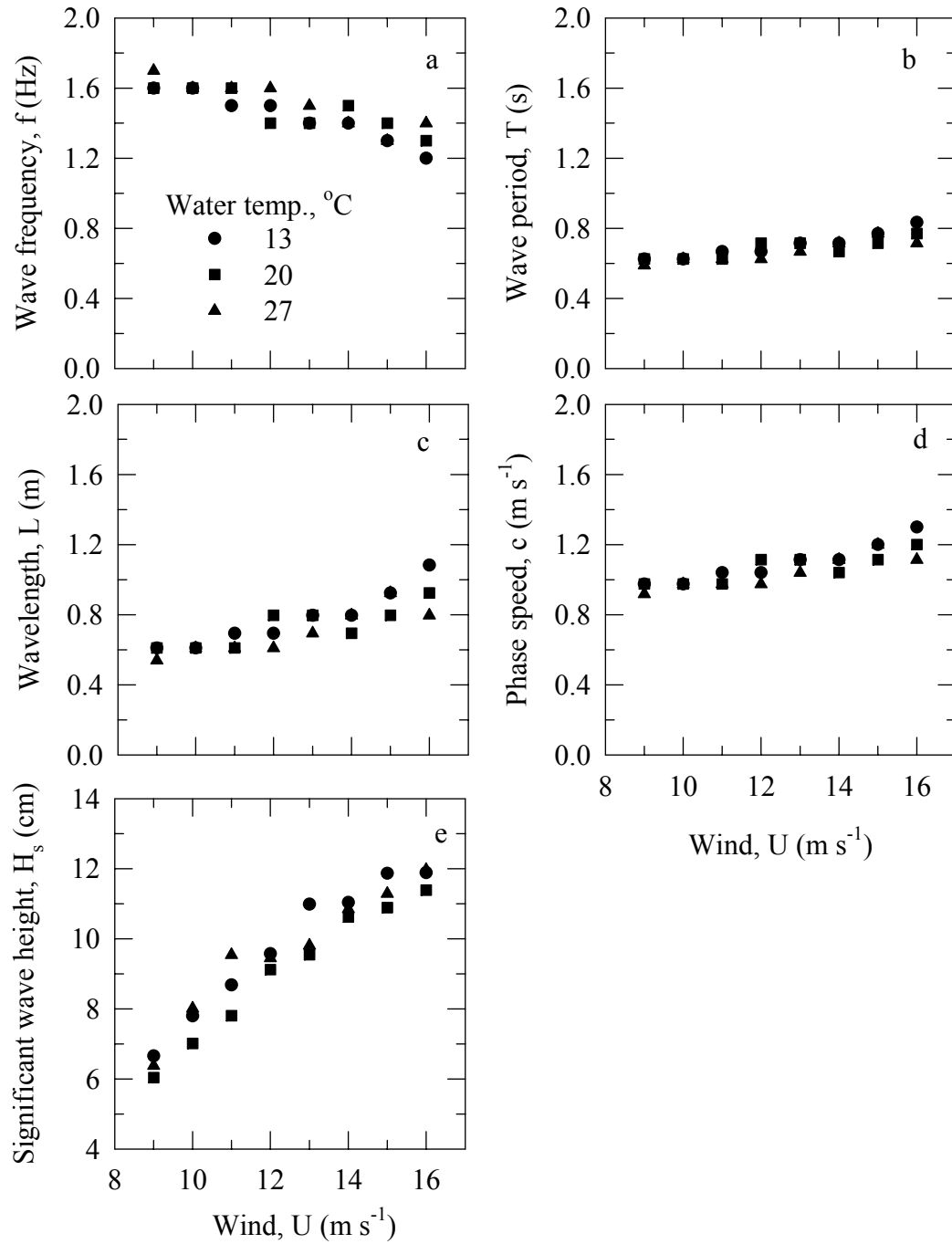


Figure 6.7 Wave characteristics vs. wind speed at three water temperatures (runs for side view): a) wave frequency, f ; b) wave period, T ; c) wave length, L ; d) phase speed, c ; e) significant wave height, H_s .

Table 6.3

View	Wind m s^{-1}	Wave characteristics @ 20 °C				
		Frequency f, Hz	Period T, s	Wave length L, m	Phase speed c, m s^{-1}	Sign.wave heigth H _s , cm
side	9	1.6	0.63	0.61	0.98	6.04
	10	1.6	0.63	0.61	0.98	7.013
	11	1.6	0.63	0.61	0.98	7.801
	12	1.4	0.71	0.8	1.11	9.118
	13	1.4	0.71	0.8	1.11	9.541
	14	1.5	0.67	0.69	1.04	10.62
	15	1.4	0.71	0.8	1.11	10.89
	16	1.3	0.77	0.92	1.2	11.39
top	9	1.7	0.59	0.54	0.92	6.748
	10	1.7	0.59	0.54	0.92	7.715
	11	1.5	0.67	0.69	1.04	9.148
	12	1.5	0.67	0.69	1.04	9.646
	13	1.5	0.67	0.69	1.04	10.97
	14	1.4	0.71	0.8	1.11	11.09
	15	1.4	0.71	0.8	1.11	11.9
	16	1.3	0.71	0.92	1.2	11.95

Rayleigh equation fits acceptably well to the wave amplitude distribution for 9 and 10 m s^{-1} (Figure 6.8, top panels) . With increasing the wind speed, however, the discrepancies between the Rayleigh curve and the observed distribution increase because of the process of waves' breaking. Srokosz (1986) developed an extension of the non-breaking waves

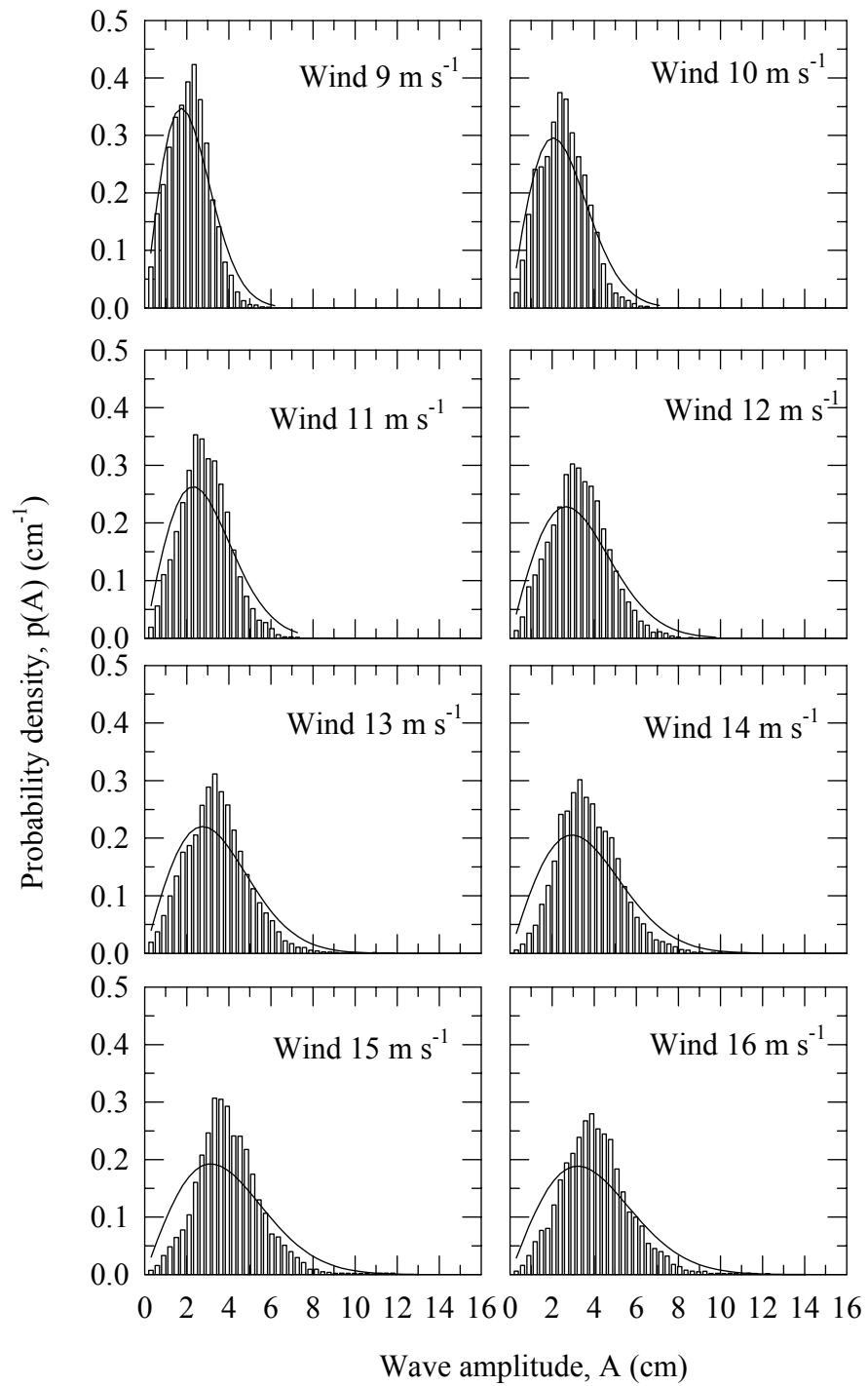


Figure 6.8 Wave amplitude distributions (runs for side view, water temperature 20 °C) . Solid lines represent the Rayleigh distribution.

theoretical model and established a probability density function for the amplitude of breaking wave crests.

6.4.2 Bubble Cloud Description

The bubble clouds are produced when the waves break. Not all waves break even at high wind, and also not all breaking waves produce bubbles. With some patience the cloud events N_c for different winds ($9 - 16 \text{ m s}^{-1}$) and in different time intervals (1, 3, 5, 10, 15 minutes) were visually counted from the video tapes. The approximate result, graphed in Figure 6.9a, shows that for 10 minutes about hundred events might happen at 10 m s^{-1} and more than 300 at 16 m s^{-1} . The production rate P (the number of events per unit time interval) increases steadily with increasing wind speeds (Figure 6.9b) and does not depend on the time interval. The collapse of the production rates for different time intervals is to be expected when the ratio of observational period Δt to that of the wave period T is large (i.e., $\Delta t/T \gg 1$).

Typical images of bubble clouds from side and top views at wind speeds 10, 12, 13, 14, and 16 m s^{-1} are shown in Figure 6.10a and b. The anticipated increasing of cloud dimensions and amount of air entrained is qualitatively observed. Generally, with increasing the wind speed the clouds become longer and wider, penetrate deeper and perhaps contain more air.

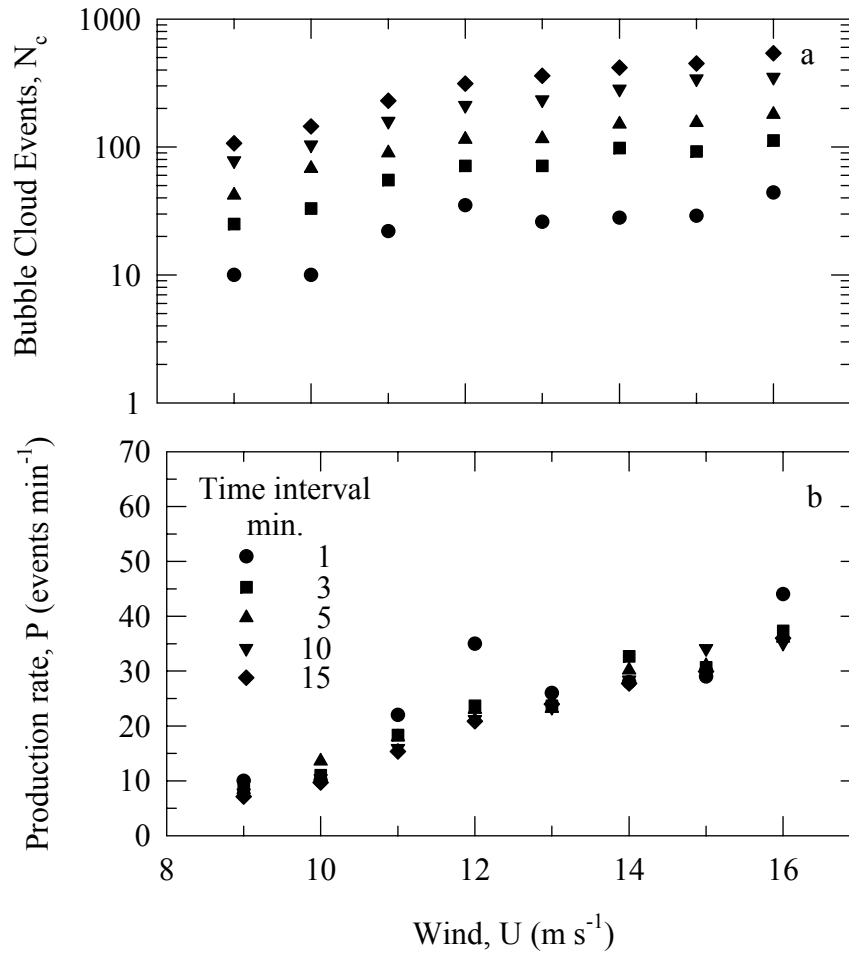


Figure 6.9 Bubble cloud production: a) number of the events in different time intervals; b) production rate of events.

A sequence of bubble cloud images representing the cloud time evolution from side (time interval $\Delta t = 167$ ms or each 5-th frame) and top (time interval $\Delta t = 100$ ms or each 3-th frame) views are shown in Figure 6.11a and b. Careful examination of the side view sequence (Figure 6.11a) reveals a trait common for all cases: the cloud starts with a plume and develops through several consecutive plumes. Each of these plumes, and

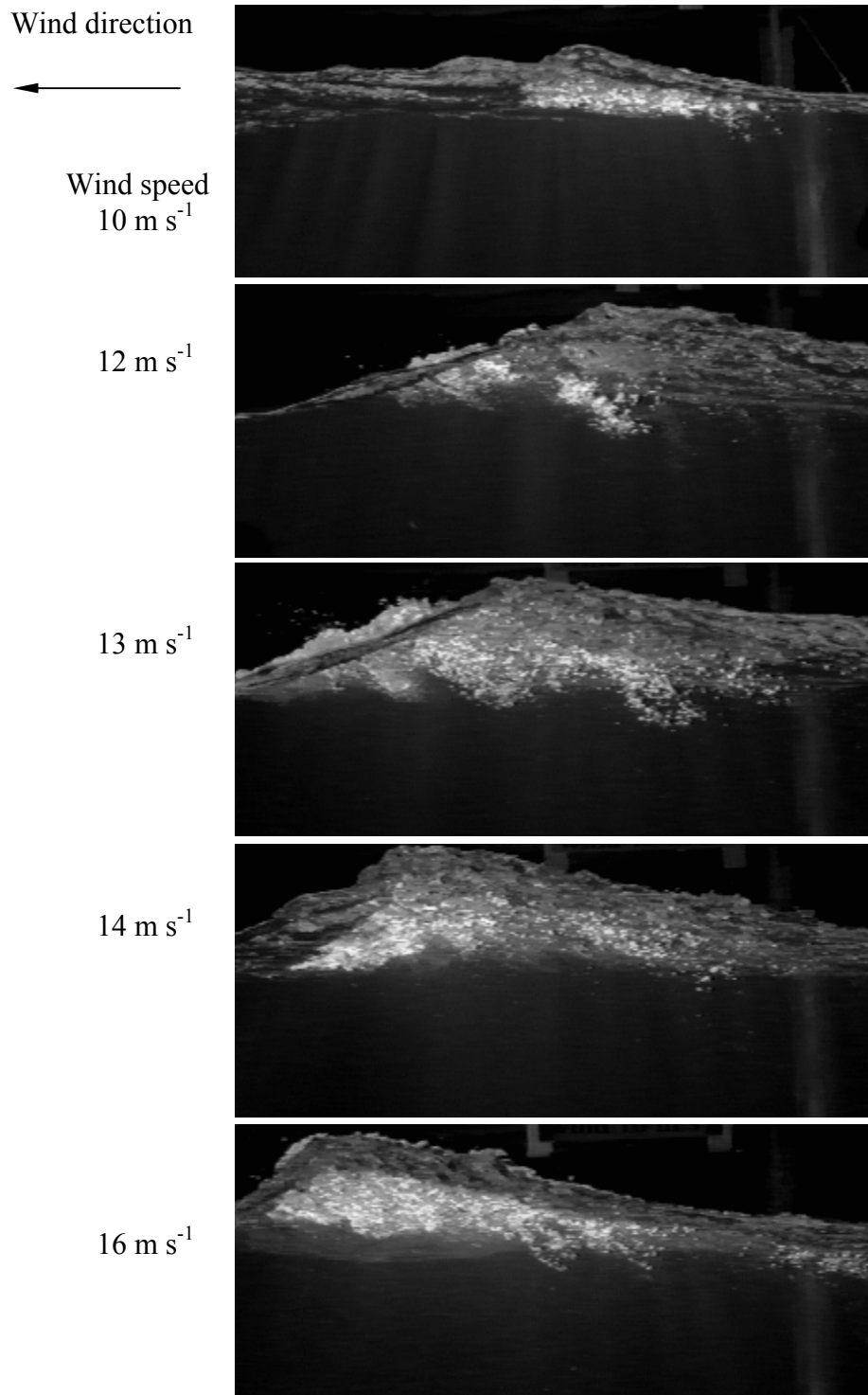


Figure 6.10a Bubble clouds at different wind speeds, side view. In visualizations bubble clouds appear to be relatively brighter.

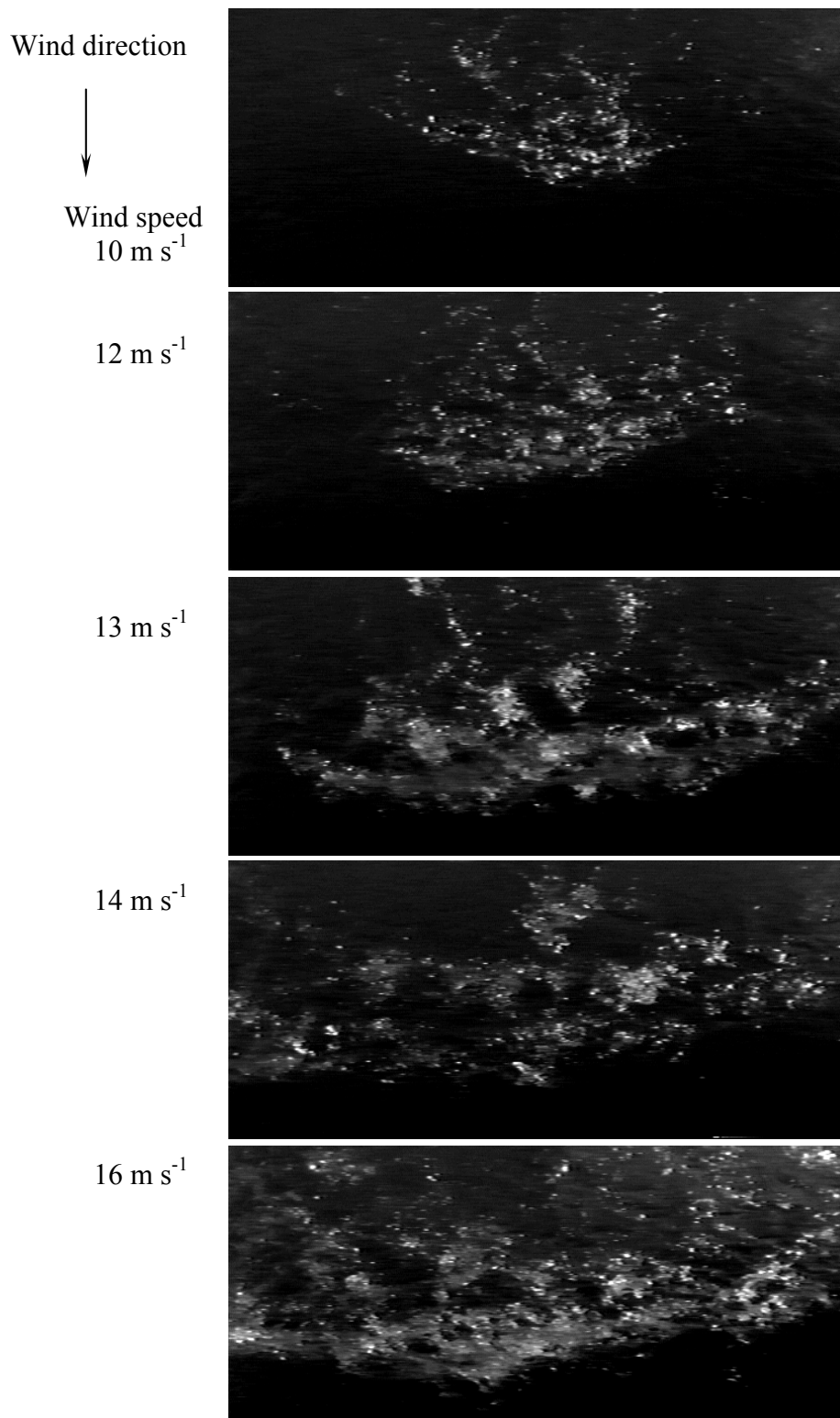


Figure 6.10b Bubble clouds at different wind speeds, top view.

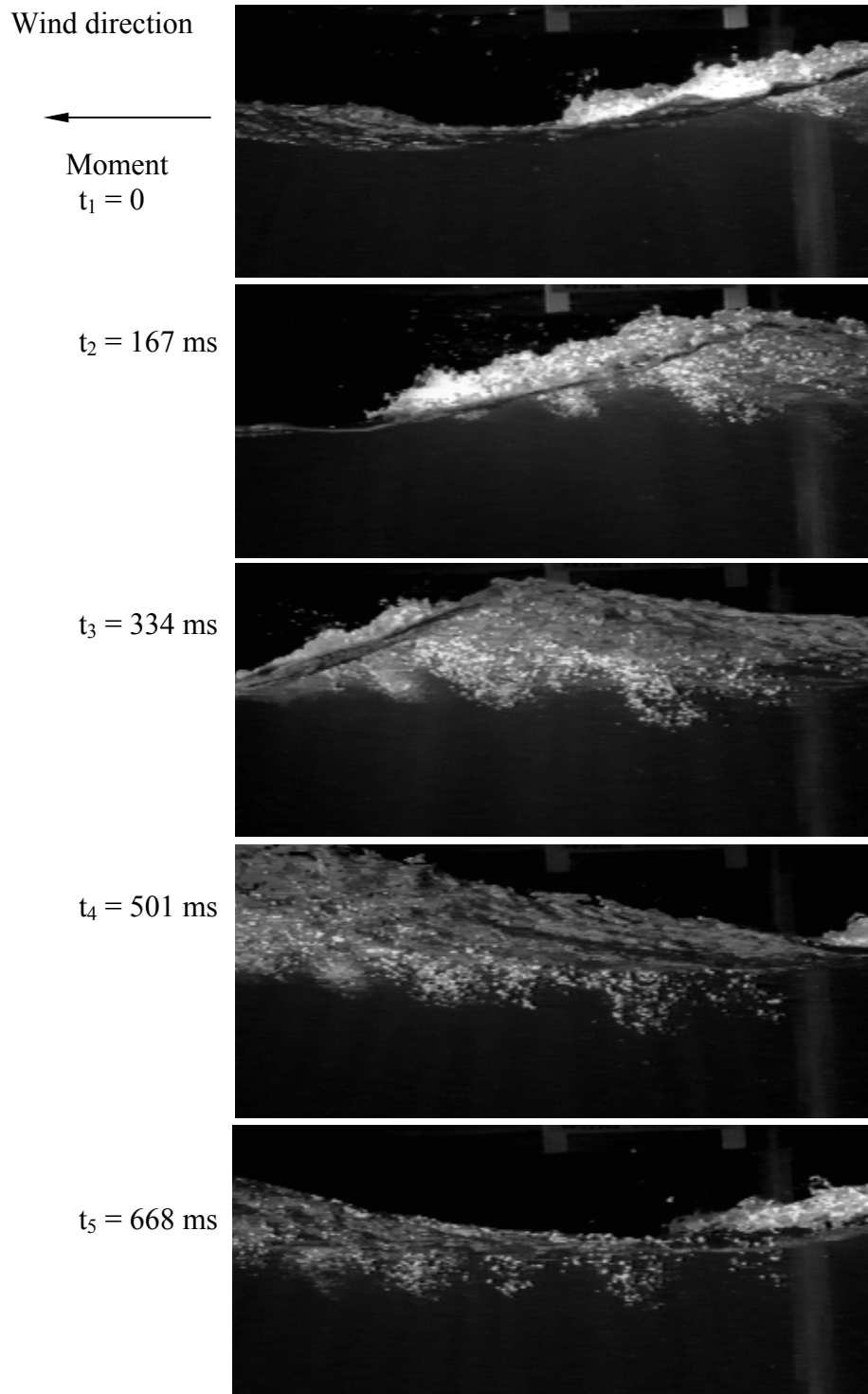


Figure 6.11a Bubble cloud at different moments ($\Delta t = 167 \text{ ms}$): side view, 13 m s^{-1} .

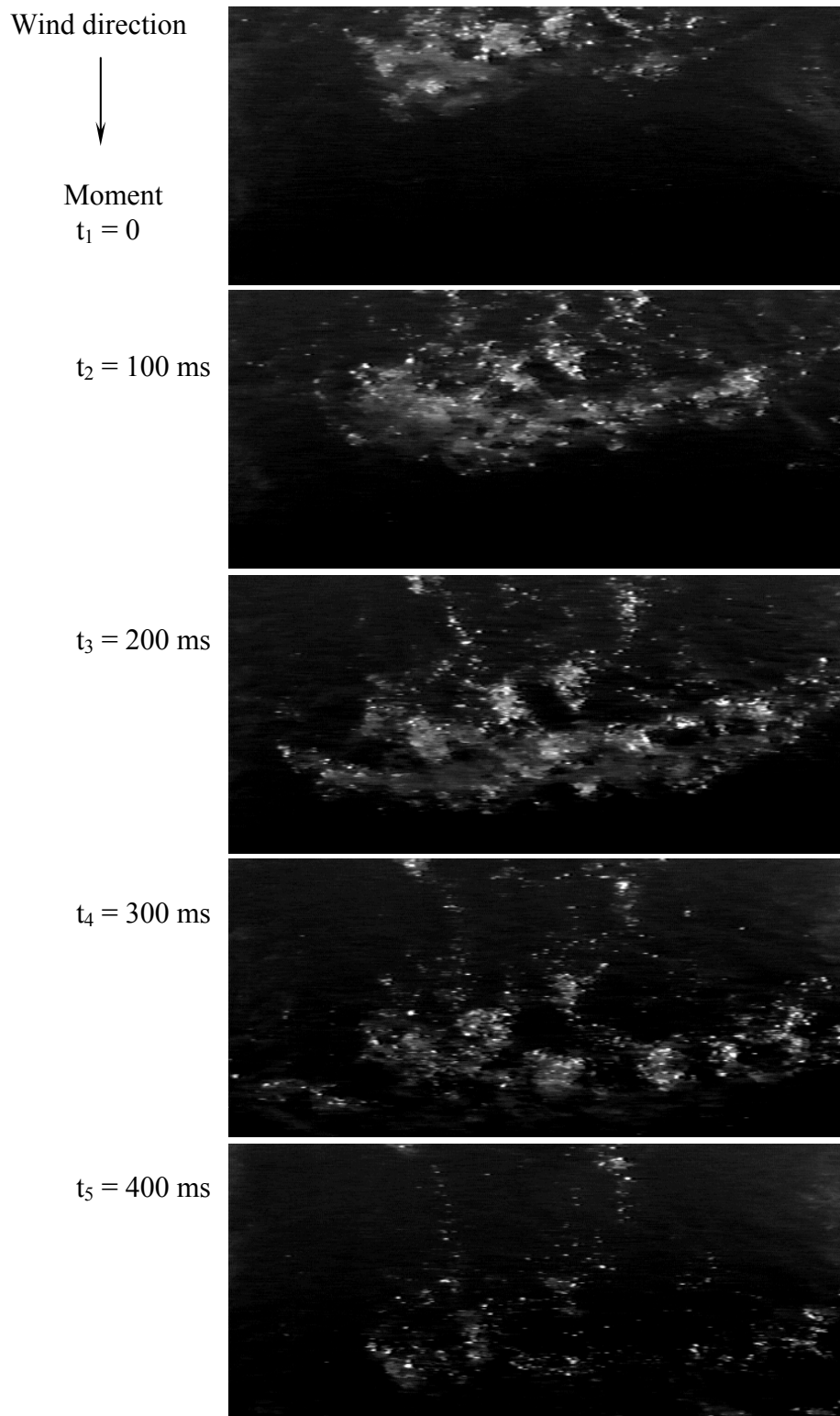


Figure 6.11b Bubble cloud at different moments ($\Delta t = 100$ ms): top view, 13 m s^{-1} .

the cloud as a whole, grows quickly, reaches some maximum size and then decays, usually for a time span less than one wave period. Further, while one plume is in its most developed stage, there are also decaying and forming plumes, so that within the cloud all three stages might be present at one moment; an example of this is the image at moment t_3 in Figure 6.11a. The growing stage of the plumes, and the cloud in its integrity, is usually faster than the decaying stage. Sometimes a group of slowly decaying plumes may linger for more than one wave period, making the cloud residual quite persistent. This residual bubble population is overlapped by the new one produced by the next wave. When some of these remnants decayed to 2 - 3 bubbles and the requirement for homogeneity was not fulfilled any more, the plume was abandoned from consideration, which caused a sudden change in the cloud length (recall the strong oscillations of the cloud parameters mentioned in §6.3.3.3) .

One might expect that this finger-like structure remains typical for the cloud inside the tank. However, the consideration of the top view sequence (Figure 6.11b) exhibit another peculiarity. The plumes in the side view are observable from top view as the ends of several streaks (lines), following a winding course, at several different places across the cloud width. The initial compact bow-like form of the cloud quickly (less than 100 ms, refer to Figure 6.11b) disintegrates into such lines. At the end of each streak the bubbles are confined in a circular patch, which sometimes seems to rotate. Compared with the initial form, these features are longer lasting; sometimes they are overlapped by the next wave. Similar observations are documented by Boundur and Sharkov (1982) . They analyzed aerial photographs and reported area values of shortly

living foam patches, which they called “dynamic” foam, associated with the moment of wave breaking and more durable “static” foam that follows the breaking event.

Once created at the front slope of the wave (at approximate wave phase of 45°), the bubble cloud has a complex motion resulting from the wave enforcing and the movement of the bubbles within. This motion can be followed via registering the distances traveled by the center of mass of one plume within the cloud from frame to frame (time interval of 33 ms) . In a coordinate system fixed with the observer and oriented along the wind direction (x is positive from right to left) and down into the water (z is positive from up to down) the cloud position in the tank is given in Figure 6.12a. It is seen that in vertical plan after the plume is formed ($t = 0$), it goes slightly deeper, then starts an excursion up and finally sinks ($t \approx 700$ s) . In horizontal plan the plume travels some distance forward and then it stays almost at one place. In a coordinate system moving with the wave and oriented the same way as the fixed coordinate system the cloud seems to travel constantly backward. The lag of the cloud behind the wave and its vertical motion relative the wave phase are illustrated in Figure 6.12b and c, respectively. The parallel between Figures 6.12a and 6.12c shows that the initial deepening of the cloud is related to wave phase range of $45 - 70^\circ$. The following upward motion is caused by the wave crest and its back ($80 - 125^\circ$). Finally, the constant sinking is a tribute of the wave trough ($135 - 300^\circ$) . The cloud horizontal and vertical positions in Figures 6.12b and c are closely spaced up to about 125° and then rarefy, which implies that the cloud motion is

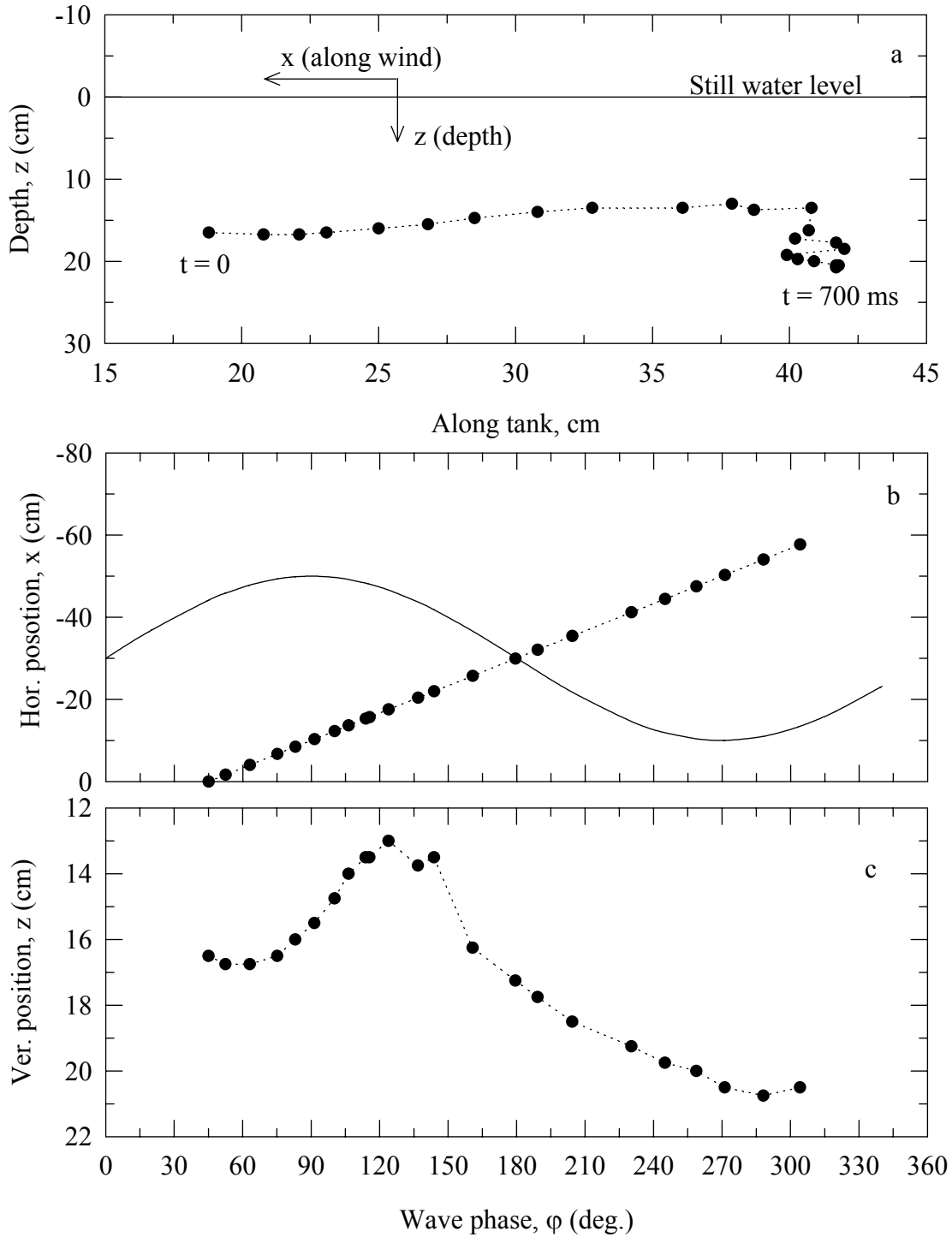


Figure 6.12 Cloud horizontal and vertical positions in space: a) relative to a fixed coordinate system; b) and c) relative to wave phase in a moving coordinate system. The solid line in b) is a reference wave profile. (Wind speed 13 m s^{-1} , water temperature 20°C .)

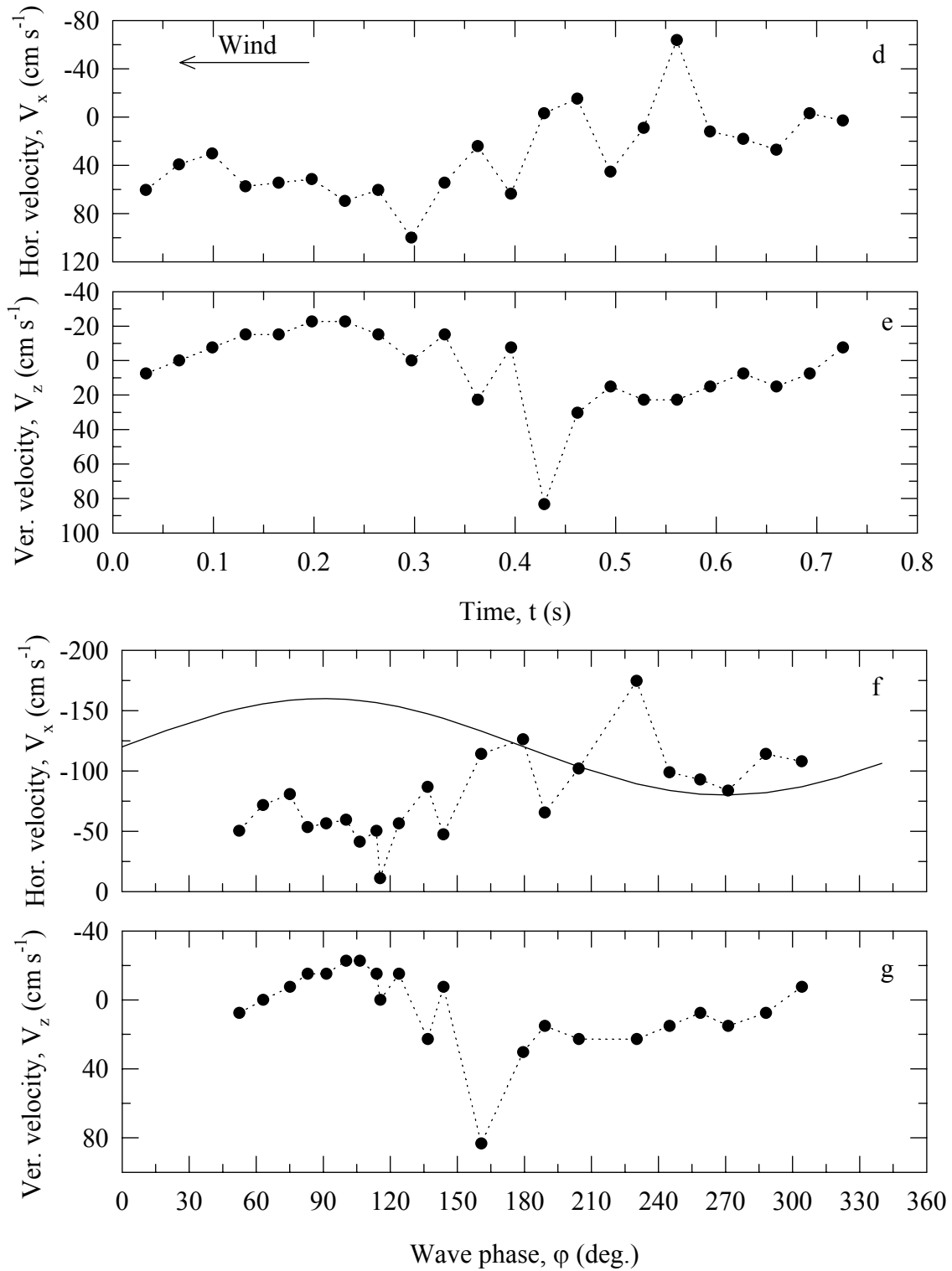


Figure 6.12 (cont.) Cloud velocity in time: d) horizontal velocity; e) vertical velocity.
 Cloud velocity relative to the wave phase: f) horizontal; g) vertical.

fast with the wave crest and its back, then it slows down with the wave trough. Indeed, it is confirmed in Figure 6.12 d and e where the temporal changes of the cloud velocities along the tank and in depth, i.e., the horizontal, V_x , and vertical, V_z , speeds, are given, respectively. The plume enters the water with a horizontal speed about 60 cm s^{-1} ($\approx 0.5c$), Figure 6.12d, and a vertical speed about 10 cm s^{-1} ($\approx 0.1c$), Figure 6.12e. The horizontal speed is quickly decelerated to a of about 20 cm s^{-1} ($\approx 0.2c$) during the first 120 ms, while the downward speed decreases to zero and upward motion starts (sign minus in Figure 6.12e notes that) . A look at the void fraction temporal changes in Figure 6.14a shows that around this time (0.12 s) the cloud has its maximum amount of air, hence it is very light and is quickly decelerated. When the degassing starts and the relative amount of water within the plume increases, it is easily dragged by the wave and its horizontal movement increases again, Figure 6.12d (time range 0.12 - 0.3 s) . After that the horizontal velocity decreases and has an average value around zero for the rest of the time. The vertical velocity increases in upward direction up to about 220 ms, then the cloud moves down and finally assumes a speed around 20 cm s^{-1} , which is comparable with the rise velocity of the individual bubbles. (From the size distributions measured in this study the mean bubble size is 5 mm and the rise velocity of such a bubble is about 25 cm s^{-1} .) Figure 6.12 f and g shows the velocities relative to the wave phase. The initial deceleration is associated with the phase range $45^\circ - 70^\circ$. The increase of the motion forward and upward is related to the wave crest and back ($80^\circ - 125^\circ$). The cloud sinks with the wave trough ($125^\circ - 225^\circ$) and at the end of the cycle has only a vertical motion

with a velocity close to the rise velocity of the bubbles. The observations of another three events at 13 m s^{-1} wind, and other winds (10 and 16 m s^{-1}) as well, repeat the same trends in space, time and relative to the wave phase.

6.4.3 Temporal and Spatial Evolutions of Cloud Parameters

The procedure for extracting the cloud parameters values from the image sequences is outlined in §6.3.3.2. Result of this image processing are time series showing the temporal changes of the cloud parameters, i.e. parameters' time evolutions. Time evolution of the cloud length (l), penetration depth (d or h), and width (w) for wind speed 13 m s^{-1} are presented in Figure 6.13a-d. For less than 800 ms the cloud parameters grow to their maximum values and then decay. In this example the cloud length, l , changes from about 7 cm to maximum 60 cm; the cloud penetration depth (or thickness), d , increases from approximately 4 cm to about 18 cm; the maximum penetration depth relative the still water level, h , reaches about 24 cm; and the cloud width quickly fills the entire FOV (about 67 cm) with streaks spread over 60 cm width. The void fractions observed from side and top view (Figure 6.14 a and b) are close to unity at the beginning reflecting the initial dense bubble population, and then gradually decrease to about 20%. The rate of decrease of the cloud void fraction α_{top} is faster (Figure 6.14b) than α_{side} (Figure 6.14a) due to larger cross section area of the cloud (several meandering streaks) in the top view compared with the area in side view. The variability in the last stages of α_{top} are caused by the shrinking of the cloud to one-two streaks, which decreases the cross section of the

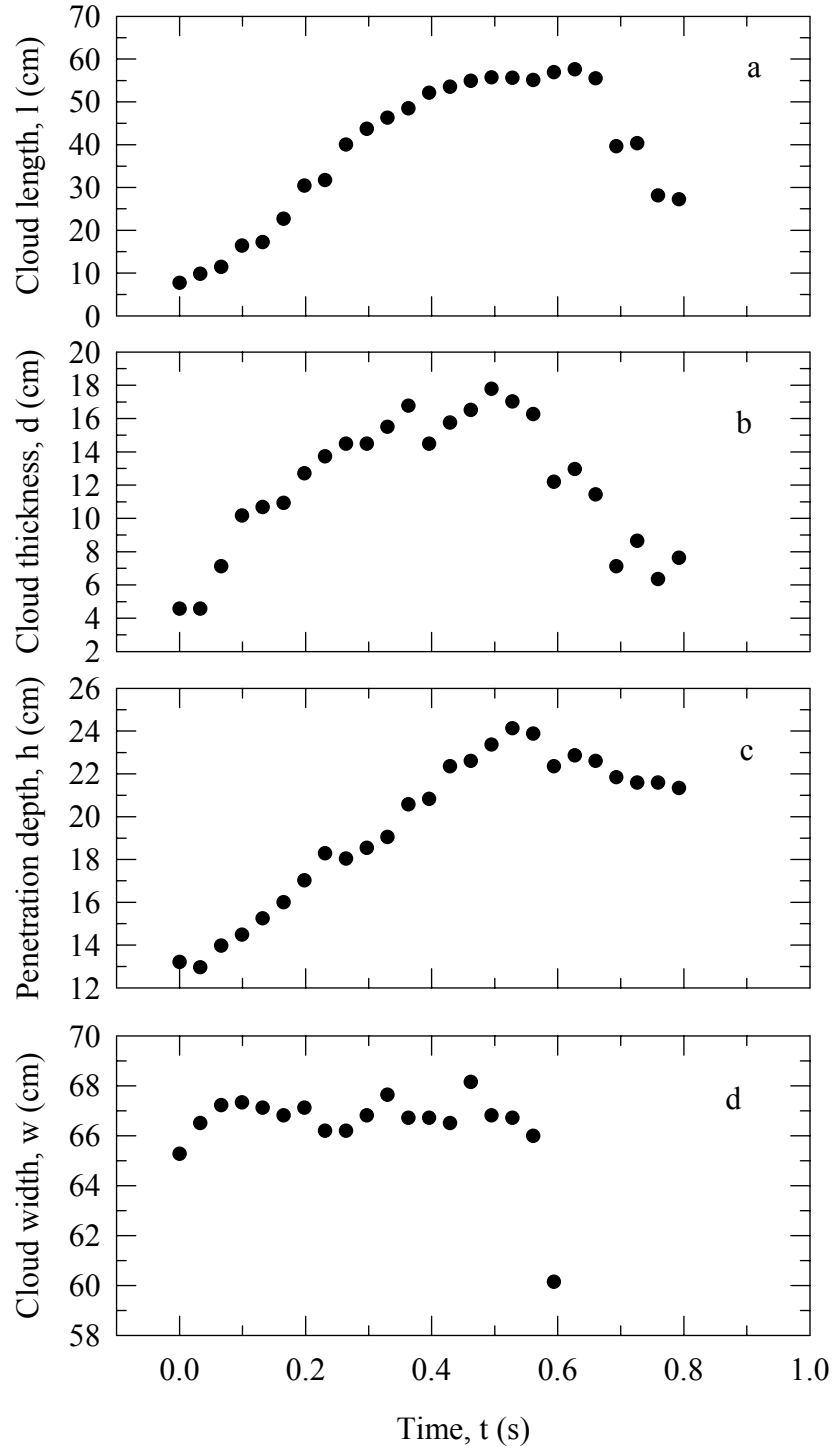


Figure 6.13 Time evolution of the bubble cloud parameters length l (a), thickness d (b), penetration depth relative to still water level h (c) and width (d) . (Wind speed 13 m s^{-1} , realizations #6 for side view, and #5 for top view.)

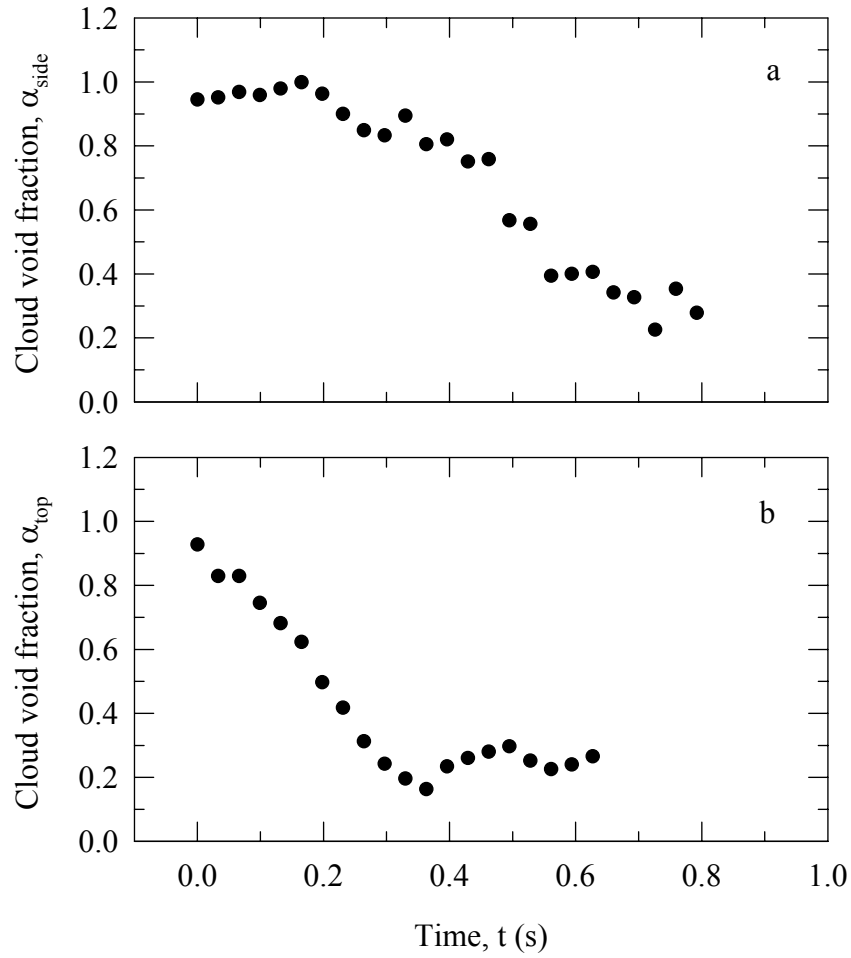


Figure 6.14 Time evolution of the void fraction: a) side view (realization #6); b) top view (realization #5). (Wind speed 13 m s^{-1} .)

cloud and renders a small increase in the void fraction. A summary of the values assumed by the cloud parameters for different winds at 20°C is given in Table 6.4. The numbers in the table are obtained using the second method of averaging.

Sets consisting of ten time evolutions of the clouds parameters are derived

Table. 6.4

Cloud parameters		Wind, m s ⁻¹ (Water temperature 20°C)				
cm		10	12	13	14	16
l	min	0.521	0.900	3.700	1.800	3.578
	max	48.036	57.100	57.600	65.900	67.200
	mean	19.474	29.625	32.634	37.315	38.875
	σ_l	8.798	10.678	6.277	9.08	11.215
d	min	0.983	1.966	3.810	2.458	2.755
	max	10.078	17.698	18.288	18.435	21.288
	mean	6.267	10.121	10.521	11.318	11.964
	σ_d	1.230	1.992	1.312	1.615	1.831
w	min	10.879	13.752	6.979	4.105	9.750
	max	53.470	66.094	68.146	66.915	68.967
	mean	33.959	46.682	51.567	47.344	53.715
	σ_w	8.963	8.457	11.663	8.421	7.482
α_{side}	min	0.040	0.043	0.110	0.010	0.053
	max	1.000	0.991	1.000	0.996	0.999
	mean	0.666	0.664	0.658	0.656	0.689
	σ	0.088	0.088	0.061	0.089	0.086
α_{top}	min	0.003	0.011	0.123	0.157	0.057
	max	0.895	0.979	0.979	0.989	0.997
	mean	0.369	0.5	0.428	0.49	0.532
	σ	0.049	0.027	0.035	0.073	0.028
process time s	min	0.396	0.561	0.627	0.462	0.462
	max	0.792	0.858	0.924	0.858	1.089

for different wind speeds. For all sequences and all wind speeds (with one exception for 16 m s⁻¹-wind) the duration of the process of cloud growing and decaying is less than a

second (see also Table 6.4, bottom) . However, the consideration of each individual time history shows that the process duration varies widely from one wind to another and from one sequence for a given wind to another sequence in the 1-s span. This fact is illustrated in Figure 6.15. In the figure the cloud lengths of two different events at winds 10, 13 and 16 m s⁻¹ are compared. For both, lowest and highest wind speeds, it is possible to observe the full cloud development for 800 ms and for 400 ms as well. The results for the other dimensional parameters (d, h, w) and at other winds speeds are the same. Most probable reason for this result is that the wave field comprises of a band of wave frequencies: not only biggest waves produce bubble clouds. A long and high wave may pass the camera FOV without breaking or cloud generation, while a lower and shorter but enough steep wave may bring the event. Therefore, bubble clouds with different sizes and lifetime intervals associated with different wave frequencies may exist at one or various winds.

The cloud development in time, described for one wind speed until now, exhibits the same traits with increasing the wind speed but the parameters' values change. Figure 6.16a - d illustrates this fact for the bubble cloud length l (a), bubble cloud thickness d (b), bubble cloud width w (c), and side void fraction α_{side} (d) at winds 10, 13 and 16 m s⁻¹.

The spatial evolution of the parameters defined from side view records for wind speed 13 m s⁻¹ is presented in Figure 6.17 a-d. For the figure the sorting of cloud parameters according to the wave phase, used in the third method of averaging, is employed. The means of each “phase” group (recall §6.3.3.3) are plotted versus the wave

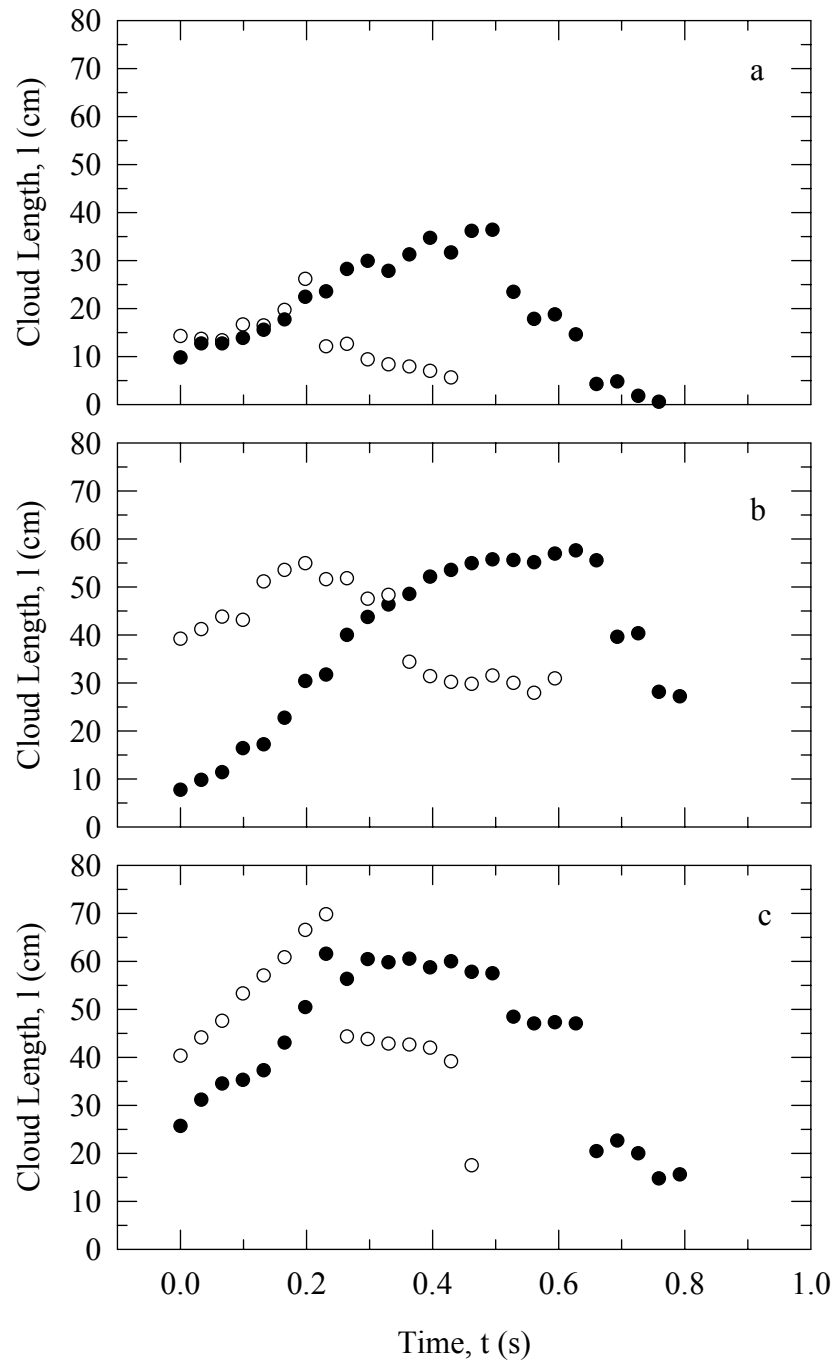


Figure 6.15 Bubble cloud length time evolutions for two realizations: a) wind speed 10 m s^{-1} , realizations ##6 and 7; b) wind speed 13 m s^{-1} , realizations ##6 and 23; c) wind speed 16 m s^{-1} , realizations ##12 and 16.

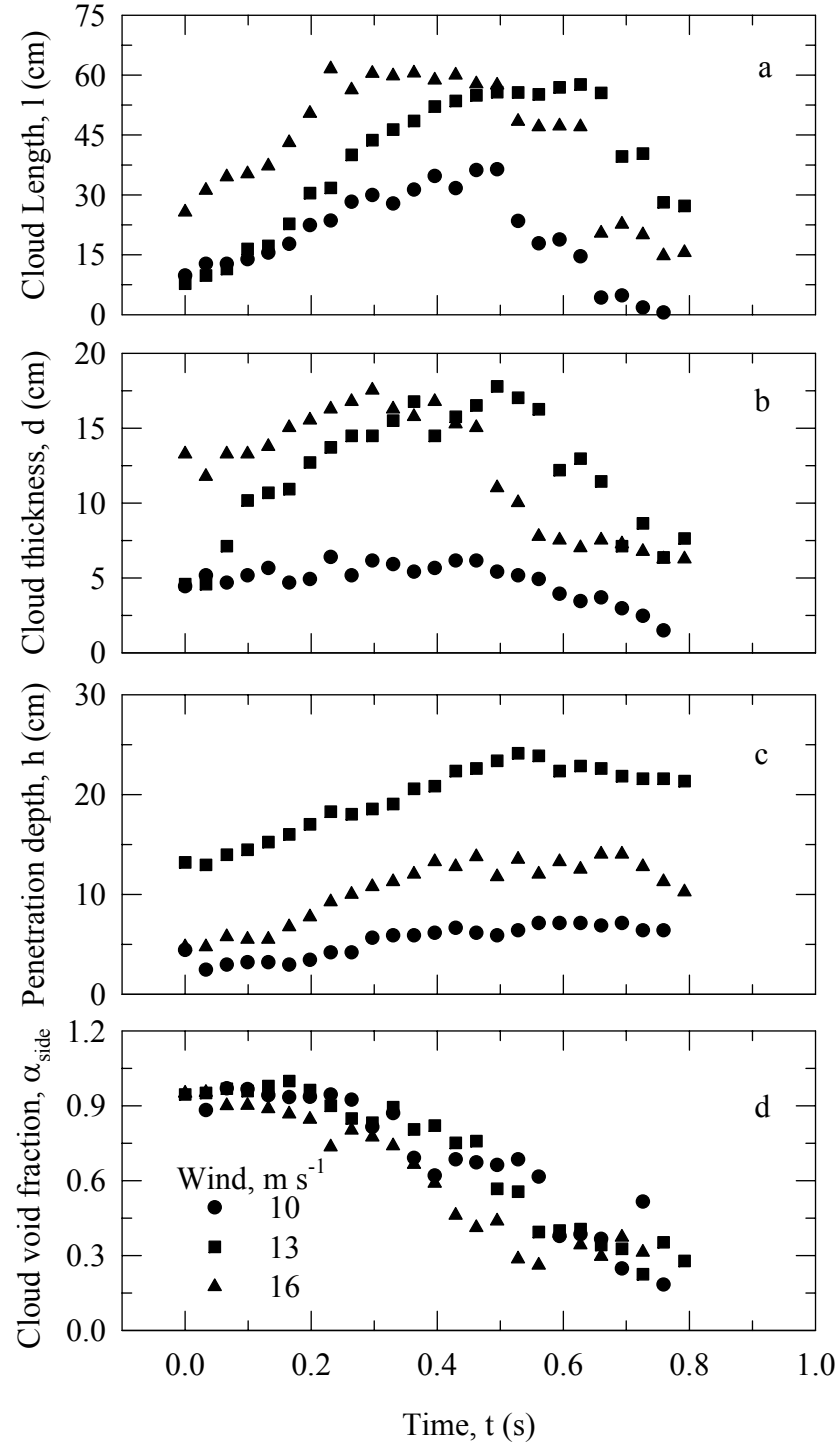


Figure 6.16 Time evolution of bubble cloud parameters in side view at different wind speeds: length l (a), thickness d (b), penetration depth relative to the still water level h (c) and void fraction (d) .

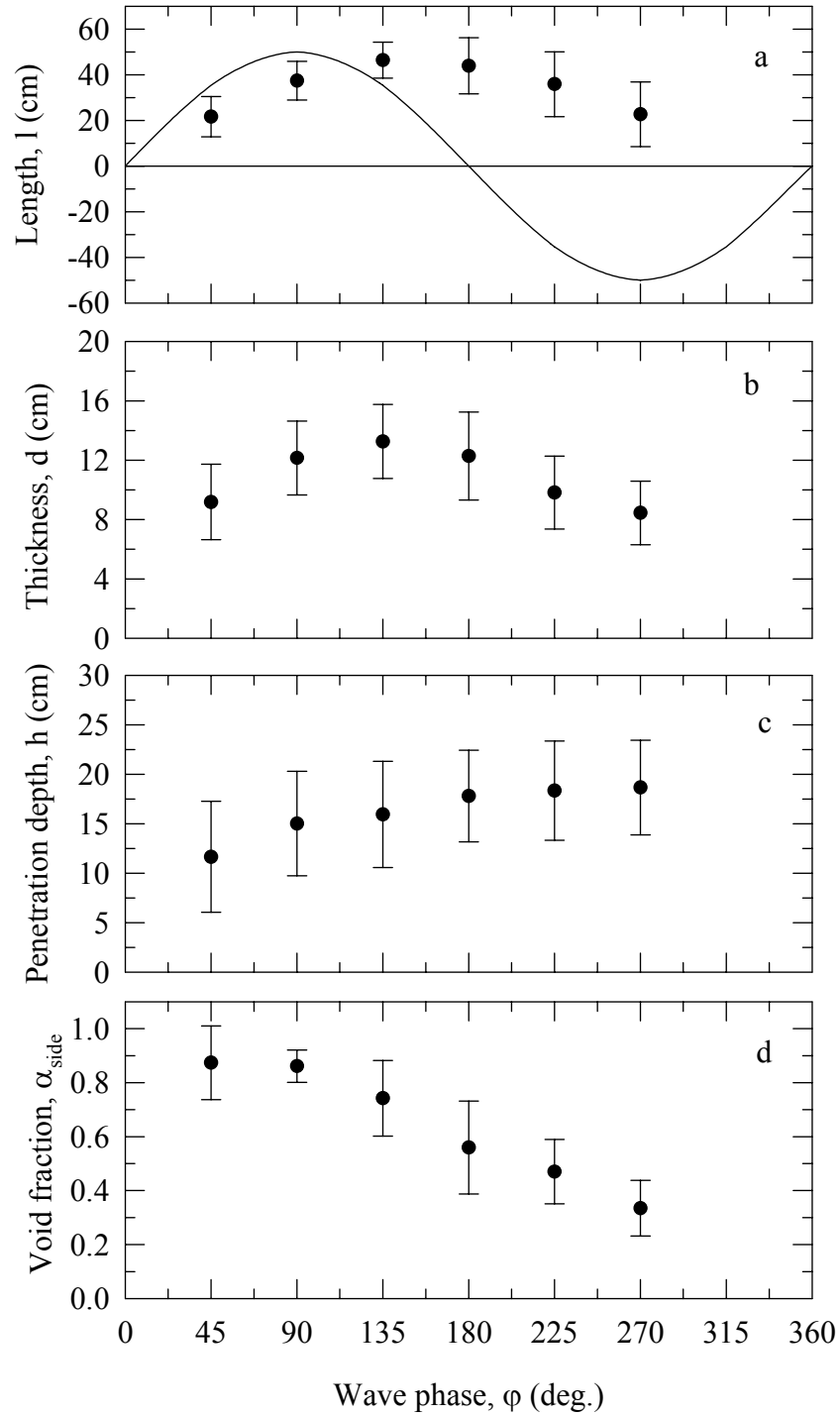


Figure 6.17 Bubble cloud parameters in side view relative to the wave phase: bubble cloud length l (a), thickness d (b), penetration depth h (c) and void fraction α_{side} (d). (Wind speed 13 m s^{-1} .)

phase ϕ ; a reference wave profile is given in a panel (a) . The cloud usually appears at around $\phi = 45^\circ$. The cloud length l and thickness d reach their maximum values around 135° (at the back of the crest), then decrease over the next 135° (Figure 6.17 a and b respectively) . The penetration depth relative to the still water level h increases constantly with the wave phase (Figure 6.17c), while the void fraction α_{side} decreases (Figure 6.17d) . In this example about 30% from the initially entrained air remain in the wave trough until the next wave comes. The bubbles comprising this residue of the cloud exemplify those oceanic bubbles that join the background population. The behavior of cloud parameters relative to the wave phase is repeated for all wind speeds. In Figure 6.18a-d the same parameters are plotted versus wave phase for winds 10, 13, and 16 m s^{-1} . The long lasting voids reach a value of 40% at 16 m s^{-1} and are often added to the newly entrained air by the next wave. Of course, there are cases, especially for low wind speeds ($10 - 12 \text{ m s}^{-1}$) the bubbles completely disappear before the next wave produces bubbles.

6.4.4 Statistical Cloud Characteristics

6.4.4.1 Probability Density Functions

As the bubble cloud parameters are random variables, it is interesting to find out how the observed values are statistically distributed. For this purpose the probability density functions (PDFs) of cloud parameters at various wind speeds are calculated. As was mentioned earlier (§6.3.3.3), all parameter values from the 10

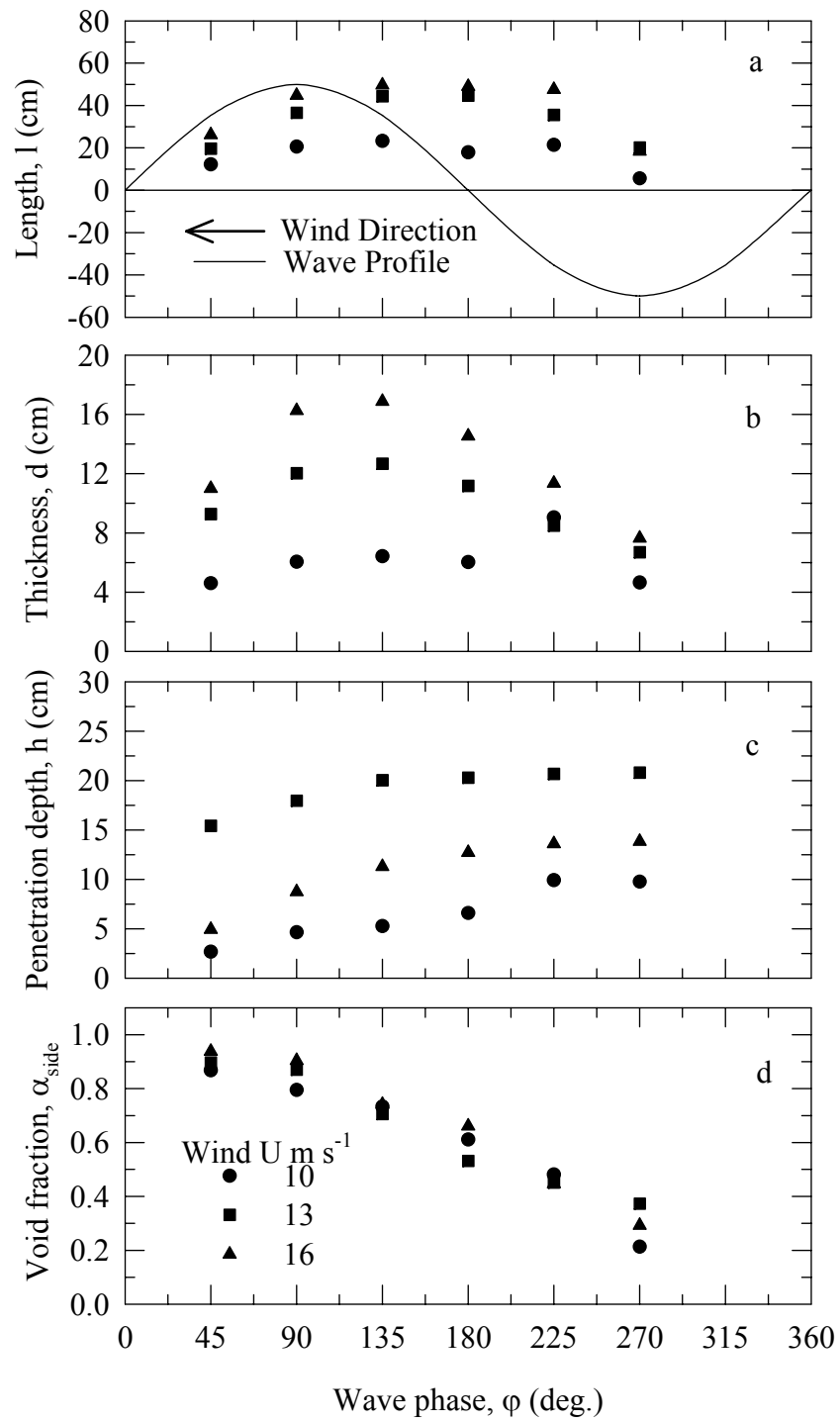


Figure 6.18 Same as in Figure 6.17 at different wind speeds. (For clarity the variances are omitted.)

realizations were used for PDF calculations. The resulting PDFs for 13 m s^{-1} wind speed are plotted in Figure 6.19 a - d. In panel (a) the PDF of bubble cloud length l is given:

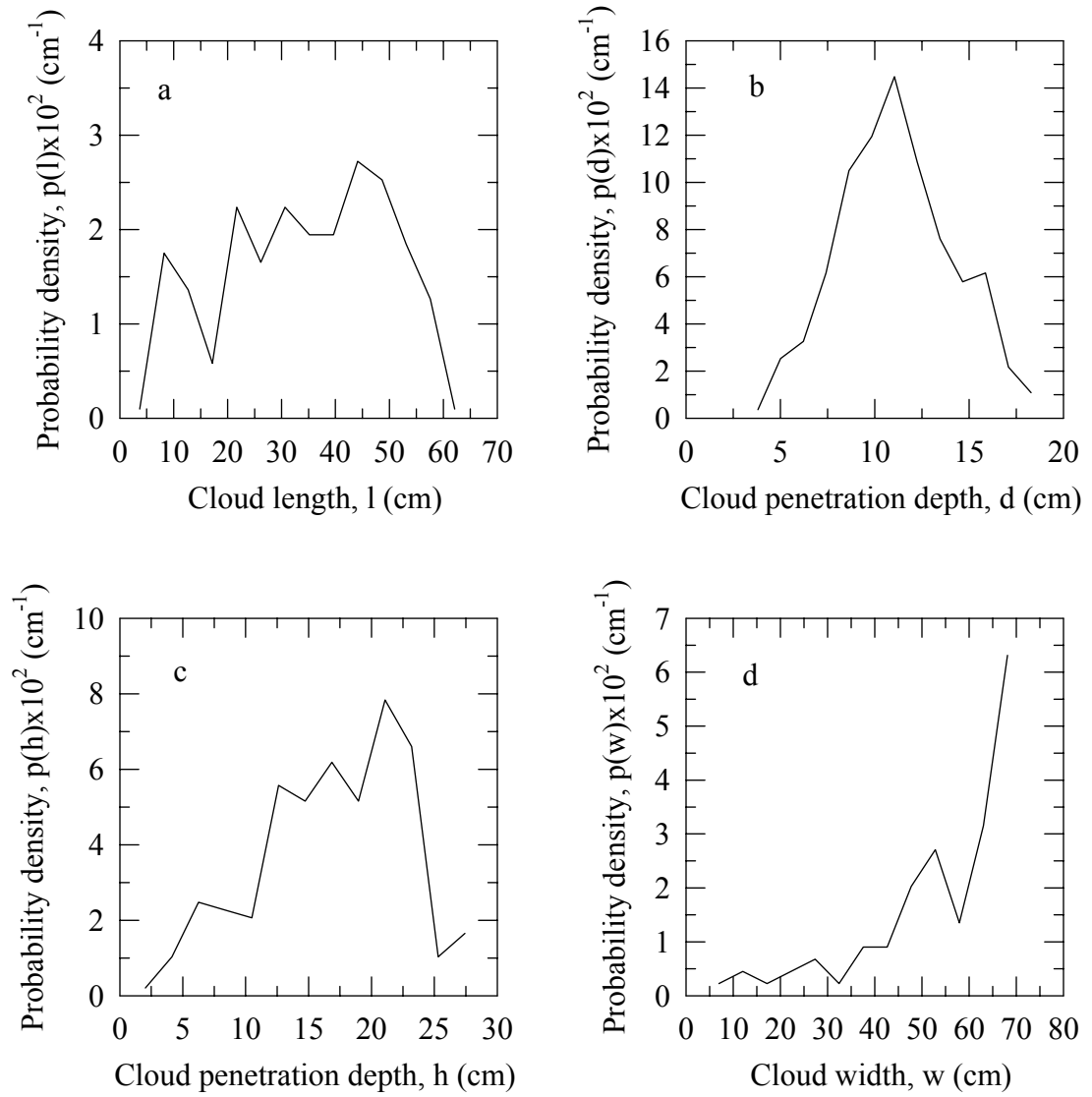


Figure 6.19 PDFs for bubble cloud parameters l , d , h , and w . (Wind speed 13 m s^{-1} ; 10 realizations, 12 bins.)

lengths around 45 cm are observed with maximum probability of 13.5% (given by the area of the corresponding band = 2.7×5 cm) . Other cloud lengths, around 10, 20 or 30 cm, are encountered with comparable probability (8.5 - 11.5%) . Bubble cloud thicknesses, d , around 10 cm (Figure 6.19b) are 1.4% (= 1.4×1 cm bin) probable, while the probability for values around 5 and 15 cm is approximately 4%. Cloud penetration depths, h , around 5 to 20 cm are observed with probability from 4 to 16 % (bin 2 cm) . The widest clouds (around 60 cm) are observed with highest probability (30 %), while widths up to 40 cm are less than 5% probable, Figure 6.19d. This PDF structure of cloud width reflects the short-living initial stages of the cloud and long-lasting streaks of bubbles formed tens of milliseconds later. The void fraction PDFs are plotted in Figure 6.20. The “side” void fraction PDF (Figure 6.20a) has two characteristics peaks: void fractions around 0.9 are observed with 21% (= $3 \times 7.1\%$ bin) probability, and the voids lingering in the wave

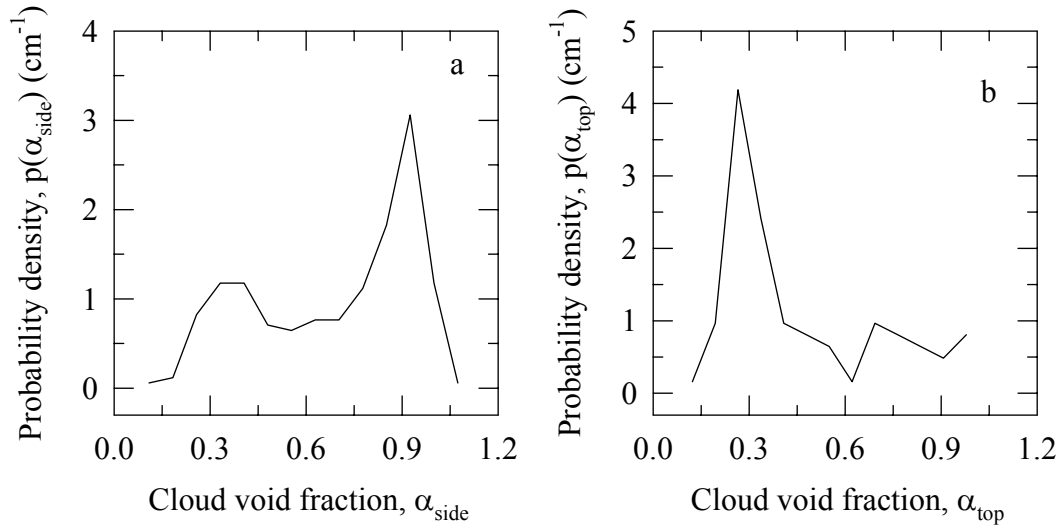


Figure 6.20 PDFs for bubble cloud void fractions observed from side (a) and top (b) views. (Wind 13 m s^{-1} ; 10 realizations, 12 bins.)

trough (around 0.3) have 7% probability. The PDF shape implies the possible equal importance of bubble population in the initial moment (narrow but high peak) and the residual bubbles (lower but broad peak) . This interpretation is additionally confirmed by the PDF shape for “top” void fraction (Figure 6.20b) . The high peak around 0.3 in the view from above emphasizes the high probability most bubbles to reside in the streaks, hence to live longer, and the fast disintegration of the initial cap (less than 7% probability for void around 0.9) .

The PDFs of bubble cloud parameters at different wind speeds are compared in Figure 6.21. In the figure all curves with solid line are for wind speed of 10 m s^{-1} , the dotted lines are for 13 m s^{-1} , and dashed lines are for 16 m s^{-1} . The first observation is that the PDFs behavior for the different parameters, described for wind speed 13 m s^{-1} in Figures 6.19 and 6.20, is generally the same for the other winds: Values in almost the entire range of lengths can be assumed with comparable probability, Figure 6.21a. The values for bubble cloud penetration depth are concentrated around some specific number (at least for lower winds), Figure 6.21b. The cloud spreading over a wide size is most probable to be observed, Figure 6.21c; and, the “side” void fractions assume most probable values around 0.9 and 0.3, Figure 6.21d. The second observation is the effect of wind speed increase: for all parameters with increasing the wind speed the range of possible observable values becomes wider and consequently, the probability of the specific values decreases. For example, in Figure 6.21a the range of lengths assumed by the cloud at 16 m s^{-1} is from 5 to 67 cm, while at wind speed of 10 m s^{-1} values higher than

40 cm are not observed. The cloud penetration depth concentrates around 5 cm with 22% probability for wind speed of 10 m s^{-1} (Figure 6.21b), which is in strong contrast to the penetration depth values from 2.5 to 20 cm with probability less than 7 - 10 % at 16 m s^{-1} wind. At 10 m s^{-1} wind the cloud width does not exceed 55 cm (Figure 6.21c) and it is

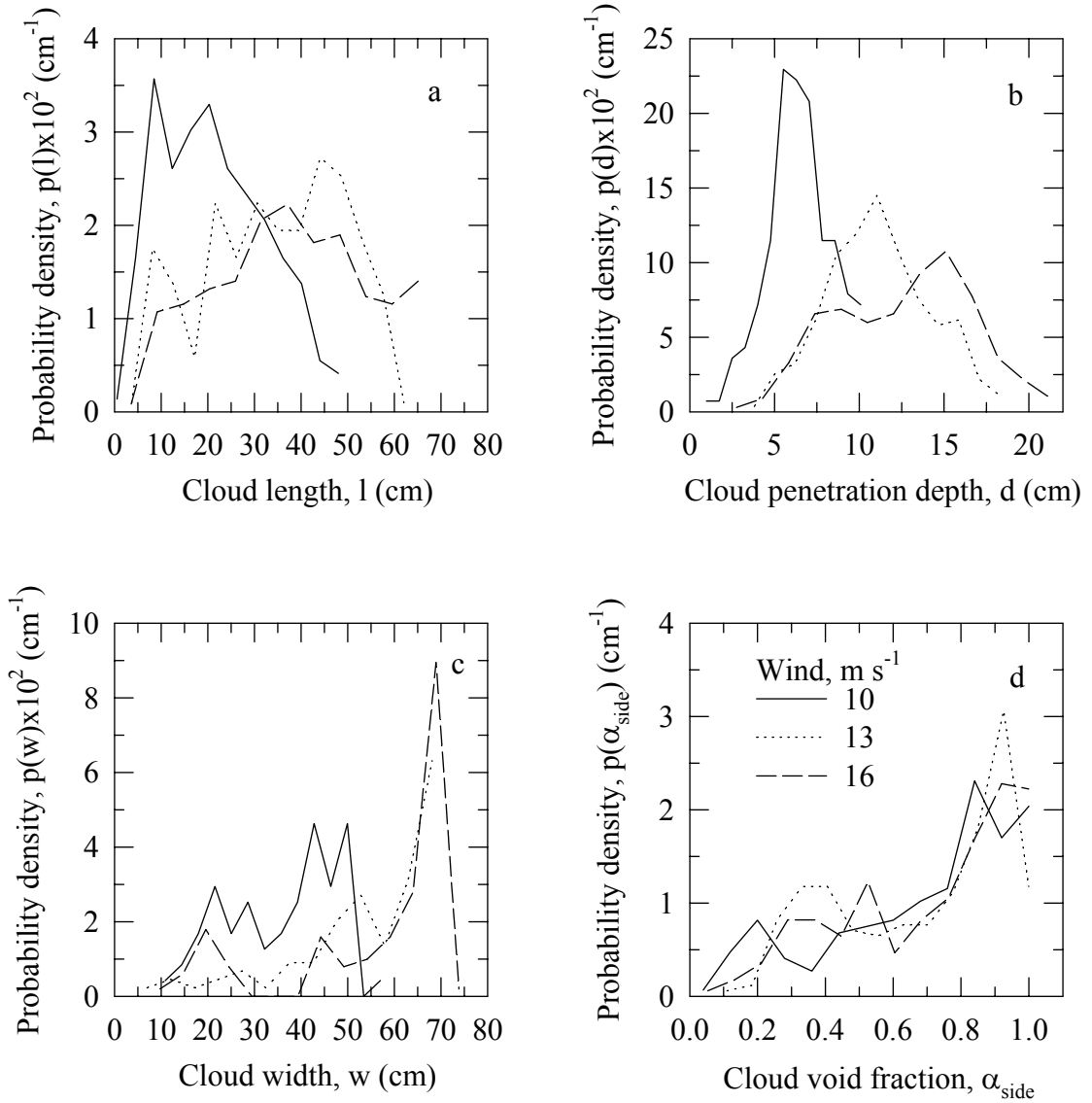


Figure 6.21 Cloud parameters' PDFs at different wind speeds (10, 13, and 16 m s^{-1}), 10 realizations: a) PDF for cloud length l ; b) PDF for cloud penetration depth d ; c) PDF for cloud width w ; d) PDF for cloud void fraction in side view α_{side} .

almost equally probable to observe less values (around 20 and 30 cm) . However, for wind 16 m s^{-1} it is four times more probable to detect wide clouds (16% for values around 65 cm) than clouds with width around 20 cm (4%) . With increasing wind speed the values of initial and residual voids (Figure 6.21d) increase from less than 0.8 and 0.2 for wind 10 m s^{-1} to about 0.9 and 0.3 for 16 m s^{-1} .

The main features of the PDF for a given parameter discussed above do not change dramatically if another 10 events, different from those used for the PDFs in Figures 6.19 and 6.20, are used (recall §6.3.3: the bias from using different selections is $\approx 10 \%$) . For example, comparison of the bubble cloud length PDF at wind 13 m s^{-1} obtained from 10 events in Figure 6.19a and another 10 events in Figure 6.22c, shows that despite some understandable difference in the shape, there is also some similarity. In both cases three peaks (around 10, 30 and 45 cm) are evident and the general behavior – wide length range (5 - 60 cm) with comparable probability (8.5 - 15%) – is the same. This statement is also true for the comparison of the void fractions α_{side} in Figure 6.20a and 6.23c. Another interesting result is that the typical PDF shape is recognizable even if only a few cloud realizations are used. In Figure 6.22 a – f the bubble cloud length PDFs, obtained from different number of realizations, are compared. The main three peaks around 10, 30 and 45 cm lengths are noticeable already in the panel (a) where 3 time evolutions of l are used giving totally only 72 points in the long realization. The increase of the number of values piled in the long realization only smooths the PDF shape but continues to exhibit the same main peaks. This observation is confirmed by Figure 6.22 where the length PDF from 5,

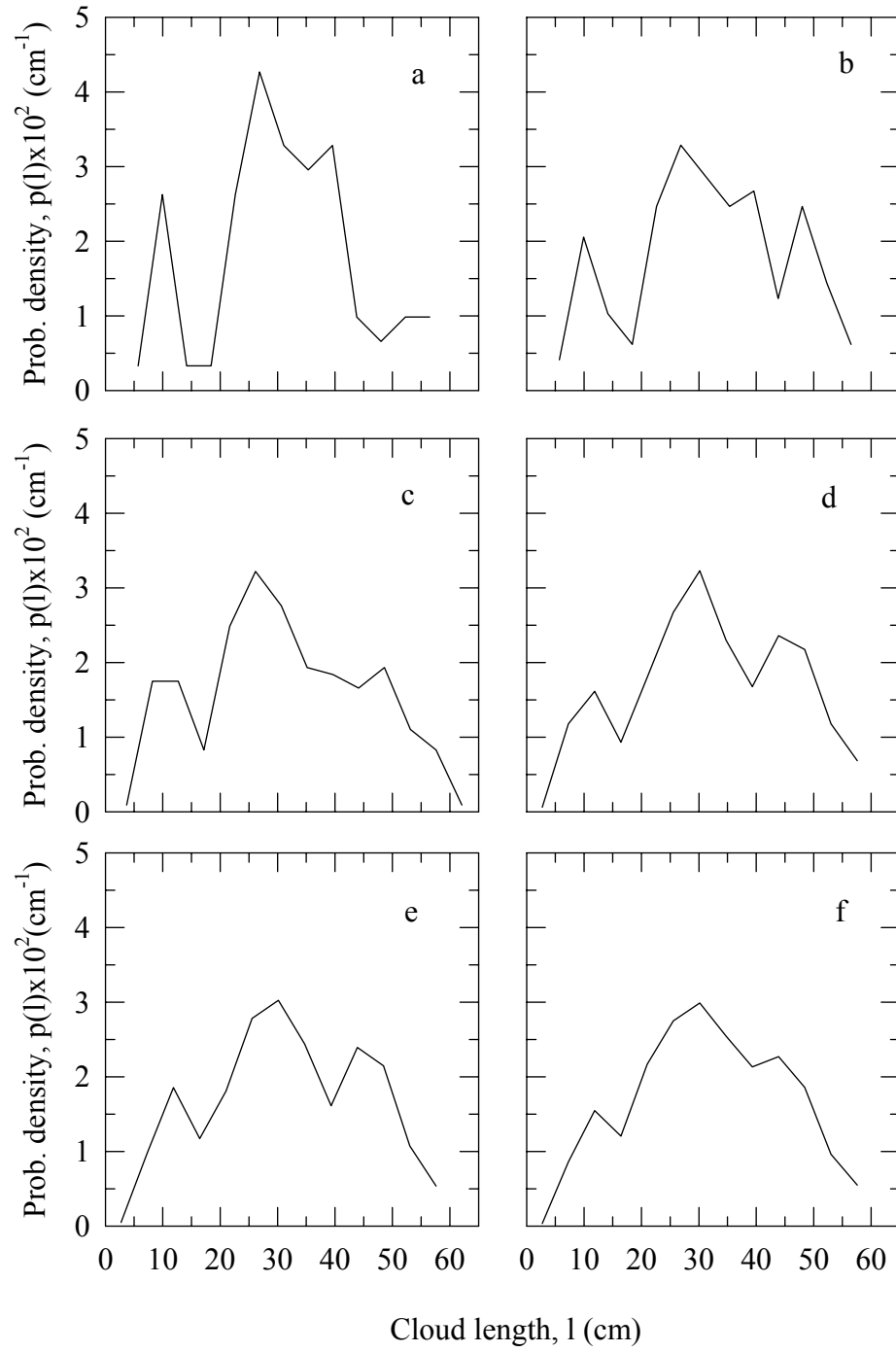


Figure 6.22 PDFs for cloud length from different number of realizations N : a) $N = 3$; b) $N = 5$; c) $N = 10$; d) $N = 15$; e) $N = 20$; f) $N = 30$. (Wind 13 m s^{-1} .)

10, 15, 20, and 30 cloud events are shown respectively in panels (b), (c), (d) (e) and (f). Similar effect is perceived from Figure 6.23 a – f, where the peaks for initial ($\alpha_{\text{side}} \approx 0.9$) and residual ($\alpha_{\text{side}} \approx 0.4$) void fractions are seen for PDF constructed only from 3 realizations (Figure 6.23a) and from 30 realizations (Figure 6.23f). This result suggests that there are common features in the random cloud appearance and their probability structure can be revealed even from a few events.

A strong impression looking at the bubble cloud parameters' PDFs is how jagged they are. The preceding discussion showed that despite their shape, the PDFs are useful to draw some conclusions for the probability behavior of the cloud parameters. Still, the ups and downs in PDFs curves make their association with some known distribution very difficult. One reason for this notched trend is that two or more processes taking place during the cloud lifetime overlap when the PDFs are constructed on the base of all observed values. (Recall the example in Figure 6.11a: the bubble cloud at moment t_3 has all stages (new, developed and decaying plumes) at once.) For instance, it is easy to recognize in the void fraction shape (Figure 6.20a) two peaks and to interpret them as the voids associated with the initial and later moments in the cloud life. To check this hypothesis, let us separate the entire sequence of cloud images into two groups representing the initial and residual stages. The first group consists roughly of the images in which the cloud is located before and beneath the wave crest. The second group includes the images in which the cloud is behind the crest and in the trough. The parameter values associated with these groups of images form two realizations and two

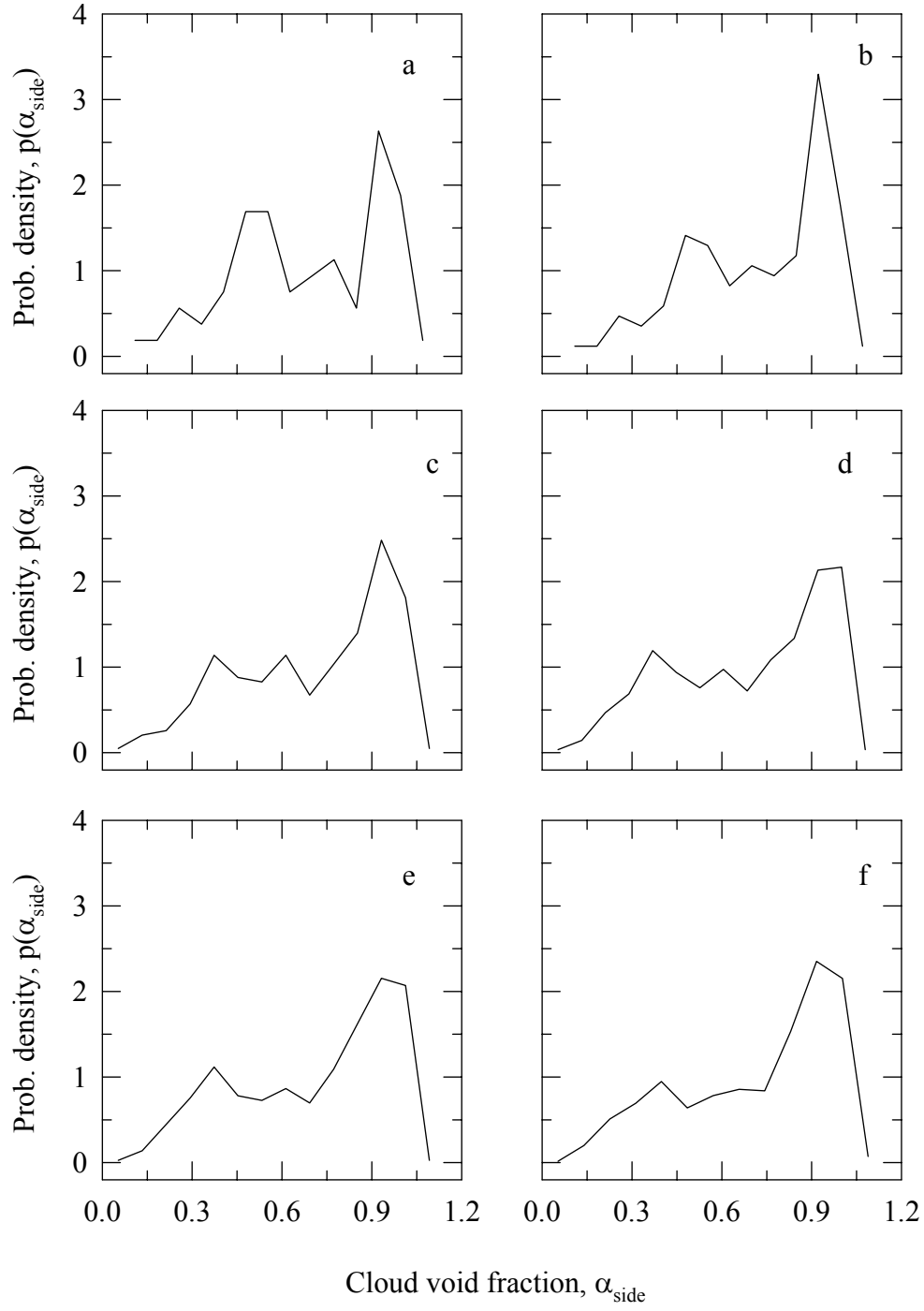


Figure 6.23 PDFs for cloud void fraction from side view obtained from different number of realizations N : a) $N = 3$; b) $N = 5$; c) $N = 10$; d) $N = 15$; e) $N = 20$; f) $N = 30$. (Wind 13 m s^{-1} .)

PDFs are constructed. The result in Figure 6.24a shows clear separation of the void fractions for initial (dotted line) and residual (dot – dash line) stages. It confirms the suggestion that two processes form the PDF for the entire cloud lifetime (Figure 6.24a, solid line) . However, this idea does not work well for the other cloud parameters. In Figure 6.24b an example is given for the bubble cloud length PDFs constructed from the realizations for the entire, initial and residual processes. There are some differences in the probabilities attributed to the different stages: the lengths around 25 cm appear mostly during the initial stage, while the residual stage contributes with higher probability for the shortest (around 10 cm) and longest (around 45 cm) cloud lengths. But more or less all three characteristic peaks are present in the PDF shapes of both initial and residual stages.

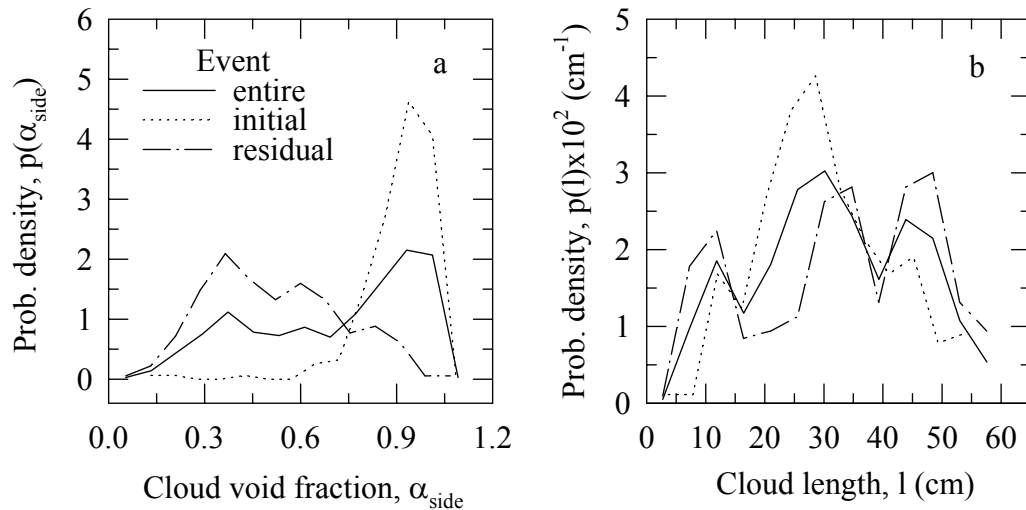


Figure 6.24 Interpretation of the PDFs features for: a) cloud void fraction from side view; b) cloud length. (Wind speed 13 m s^{-1} ; 20 realizations.)

The conclusions for bubble cloud thickness and penetration depth PDFs are similar to those for bubble cloud length PDFs. Perhaps the entire process should be broken into finer stages in order to find out which parameter values with which stages of the cloud life are coupled. Whatever these stages are, it seems reasonable to state that the uneven PDF shape is due to the overlapping of two or more particular processes (or different stages of one process) happening at different moments during the cloud lifetime.

The PDF shapes for the different cloud parameters are fitted with different known distributions. The void fraction of the residual process seems to follow the Rayleigh distribution (Figure 6.25), while the void fraction at the initial moment can not be associated with known distribution.

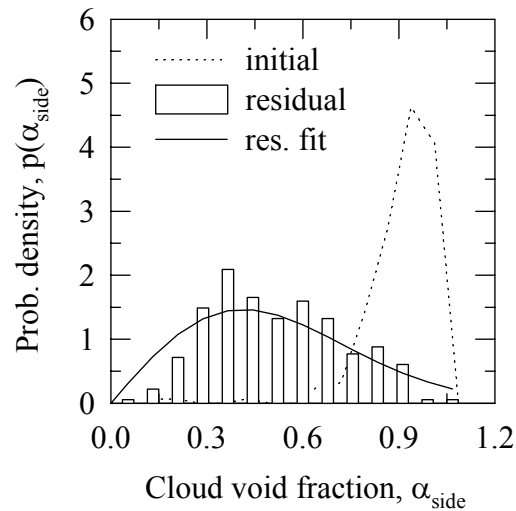


Figure 6.25 Distribution fit to the separate branches of the cloud void fraction.

6.4.4.2 Mean Values

It was mentioned earlier that it would be helpful to derive from the analysis some compendious number for each cloud parameter. It is true that this number would hide the temporal information of the studied process, but it would allow some summarizing parameter value to be associated with a given wind speed. Some mean value of the data available seems to be adequate for this purpose. The question then is how to get the most meaningful average value for nonstationary data? As the time evolutions of the cloud parameters are with different duration (recall Figure 6.5a), hence the realizations are with different lengths, the traditional ensemble average could not be applied. Three other methods, described in §6.3.3.3, were considered. The values of means and variances for bubble cloud length l , bubble cloud penetration depth d and “side” void fraction α_{side} at wind speed 13 m s^{-1} obtained with the three methods are listed in Table 6.5.

Table 6.5

Wind m s^{-1}	$l \text{ cm}$ σ_l			$d \text{ cm}$ σ_d			α_{side} σ_α		
	Method 1	Method 2	Method 3	Method 1	Method 2	Method 3	Method 1	Method 2	Method 3
10	19.344	19.747	21.071	6.110	6.267	6.563	0.660	0.666	0.630
	11.226	8.798	5.059	1.828	1.230	1.126	0.268	0.088	0.207
12	29.370	29.63	31.056	10.228	10.121	10.495	0.659	0.664	0.666
	14.381	10.68	8.429	3.257	1.992	1.621	0.244	0.090	0.220
13	32.316	32.634	34.618	10.558	10.521	10.851	0.654	0.658	0.640
	14.702	6.277	10.462	3.051	1.312	1.956	0.250	0.061	0.220
14	37.070	37.315	37.248	11.269	11.318	11.249	0.647	0.656	0.627
	15.171	9.080	10.585	3.312	1.615	2.593	0.245	0.089	0.245
16	37.002	38.875	39.188	11.807	11.964	12.288	0.672	0.689	0.702
	17.488	11.215	12.530	3.944	1.831	2.819	0.259	0.086	0.235

With the first method for each cloud parameter (l , d , h , w , or α) at a given wind speed the mean and variance of one long realization, consisting of all ten time evolutions for the parameter, are delivered (columns "Method 1" in Table 6.5) . The variance in this case is quite wide, 30 - 50% of the mean. With the second method the means and variances for each of the ten time evolutions are first found, then the mean and variance of the realization of means (10 points) are reported for each parameter (columns "Method 2" in Table 6.5) . The variances in this case are lower: 10 to 30 % of the means. With the third method the values for each parameter are sorted in six groups related to wave phase, a realization of the means for each "phase" group is then formed and the mean of this realization is reported for the parameter (columns "Method 3" in Table 6.5) . There is a difference not only between the variances of the averaging methods used, but also between the variances of the various parameters. Commonly, the variances for the cloud length l are widest; for the penetration depth d and the void fraction α_{side} they are at most 30% of the mean.

The means and variances in Table 6.5 can not be considered strictly in terms of the standard statistics. Perhaps it is more properly to think of them as the center around and the range over which the cloud parameter changes rather as the fluctuations of the parameter values around its mean. In other words, it is inappropriate to say that at wind of 13 m s^{-1} the clouds have mostly lengths of 32 cm. This would be a statement with an approximately 47 % error (refer to column "Method 1" for parameter l at 13 m s^{-1} -wind in Table 6.5) . It is more informative to say that for 13 m s^{-1} -wind the lengths of

the generated clouds are $\pm 47\%$ around 32 cm, i.e., one might expect clouds to be 17 cm long and 47 cm as well. The use of the numbers in Table 6.5 then is to know for a given wind speed in which range to expect the cloud parameters values.

6.4.5 Wind Dependence of the Cloud Parameters

The means and variances obtained with the second method of averaging for each cloud parameter at different wind speeds are used to depict their trend with increasing wind (Figure 6.26) . As expected, all dimensional bubble cloud parameters (l , d , h , w) show increase with increasing wind, but with different rates. Over the wind range from 10 to 16 m s^{-1} the bubble cloud length increases from 20 cm to 35 cm, Figure 6.26a. The bubble cloud penetration depth d increases only with 4 cm (from 6 to 10 cm), Figure 6.26b. The cloud width increases from 30 to 50 cm, Figure 6.26c. Interestingly enough, the void fraction α_{side} stays around an average value of 65% over this wind range, Figure 6.26d. The amount of air entrained is probably increasing with the wind speed, however this air volume is spread in larger cloud volumes as all cloud sizes increase with the wind too, so that ultimately the void fraction remains almost constant within the bubble volume. In addition, the values used for the wind dependency of the void fraction are averaged and they do not reflect the time variance of the voids. Probably the trend of increasing void fraction with the wind speed, observed by Walsh and Mulhearn (1987) and modeled by Wu (1992b) would appear if the voids are tracked for some specific moment (e.g. when the cloud has its maximum length) or at some specific wave phase (e.g., when the cloud is beneath the crest) . A new look at Figure

6.18d reveals that the last suggestion might be true in some cases (for $\varphi = 90^\circ$) and false in others (for $\varphi = 180$ and 270°), but also shows unnoticeable changes of the voids with wind in all other “phase” groups (for $\varphi = 45, 135$, and 225°) .

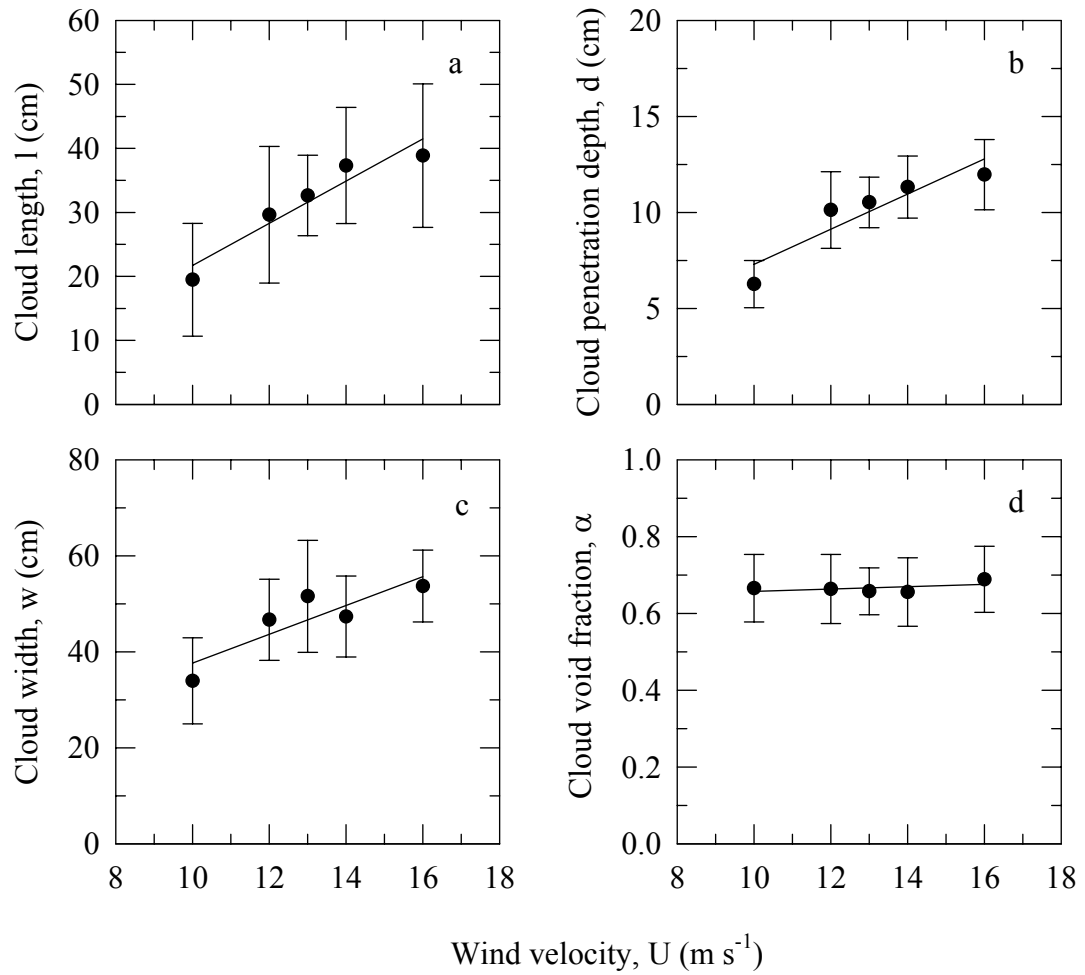


Figure 6.26 Wind dependence of the bubble cloud parameters: a) cloud length; b) cloud penetration depth; c) cloud width; d) cloud void fraction from side view.

6.4.6 Temperature Effect

The discrepancies in bubble size distributions obtained from different researchers are attributed to the temperature effect (§3.6.4) . Deliberate laboratory investigation of the temperature influence on bubbles was made by Hwang et al. (1991) . The main conclusion was that the low temperatures restrict the depth of penetration to lower values and inhibit the inception of the bubble formation. This result was generally consistent with the facts observed in field experiments: the low temperatures cause narrowing of the range of bubble sizes and decreasing of the penetration depths in winter compared with those in fall (Thorpe, 1982) . However, the fact that in laboratory bubble formation stopped at about 11°C, while field measurements in cold water (2 - 3°C) gave considerable amount of bubbles (Johnson and Cooke, 1979) points to the inconclusiveness of the studies on the temperature effect. Wu (1988b) considered the effect of water temperature on the whitecap coverage, a manifestation of the underwater bubble clouds. His results indicated that there are no systematic variations of the whitecap coverage with the water temperature, but only for the temperatures near zero. Later, Wu (1992b) more specifically pointed to the sharp drop-off of the whitecap coverage for water temperatures less than 10°C to zero. Over the range of higher temperatures (above 10 to about 30°) the data could be presented with a horizontal line, but the doubt that the trend of constant whitecap coverage with increasing temperature remains. The theoretical considerations (§2.6) show that the growth of a thermally controlled bubble is inhibited. All these facts together with the scarce results in the literature on the effect of water temperature on

bubble clouds, make the prediction of the temperature influence difficult.

The experimental observations listed above are supported by general physical considerations of the water properties changes with temperature. With decrease of water temperature the following phenomena are expected. First, the surface tension of the water increases, which means that more work is necessary to create a new area or to expand existing ones in the water (§2.7.2), therefore, the formation of the bubbles would be hindered. Second, the difference of the temperatures of the water and air entrained, encapsulated in the bubbles, would eventually give temperature gradients sufficient to make the bubble dynamics thermally controlled. This in its turn would hamper further the bubble formation. Third, the water becomes denser and this eventually would restrict the penetration of the bubbles in depth. Also, it would lead to smaller traveling distance from the surface and hence smaller residence time of the bubbles in the water. Finally, the diffusion would be less in a system with less internal energy, which would restrict the depth penetration additionally. Overall, with a decrease of the water temperature it is expected that less and smaller bubbles be formed (hence smaller void fractions), their penetration depth be less, and their lifetime in the water shorter. In contrast, with an increase of the water temperature an enhancement of the process of formation (i.e., higher void fractions) and an increase in downward movement and bubble lifetime are anticipated. However, it is difficult to predict how all these processes would reveal, if at all, when the influence of a random wind-produced wave field is acting.

The procedures for recording, digitizing, extracting the parameters' values and analyzing of the data at different water temperatures are identical to those for 20°C

described earlier (§§6.2 and 6.3) . The results obtained for each water temperature (13, 20, and 27°C) and wind speed (10, 13, 16 m s⁻¹) are based on sets of 5 time evolutions. The discussion in §6.3.3 justified the usage of less number of time records N for obtaining statistical values.

6.4.6.1 Time Evolutions

Time evolutions of bubble cloud dimensions (l, d, h, and w) for wind speed 13 m s⁻¹ and at three different water temperatures (13, 20, and 27°C) are plotted in Figure 6.27a-d. First, similar to the results for room temperature (20°C), the duration of the process in warmer and colder water is less than a second. However, close observation of the figure shows that for all parameters with an increase of the water temperature the duration of the time evolutions slightly increases as well. This is one sign for the expected increase of the bubble cloud lifetime. Second, the anticipated enhancement of the bubble cloud development with an increase of the water temperature, expressed through the cloud dimensions increasing, is almost ideally revealed. For each of the cloud parameters the values for 13°C are lowest and those for 27°C are highest. However, the comparison among various arbitrary chosen time evolutions for the three temperatures shows that this trend is not always so ideal. Another set of time evolutions of cloud dimensions at different water temperatures is plotted in Figure 6.28a-d. Some unexpected behavior is

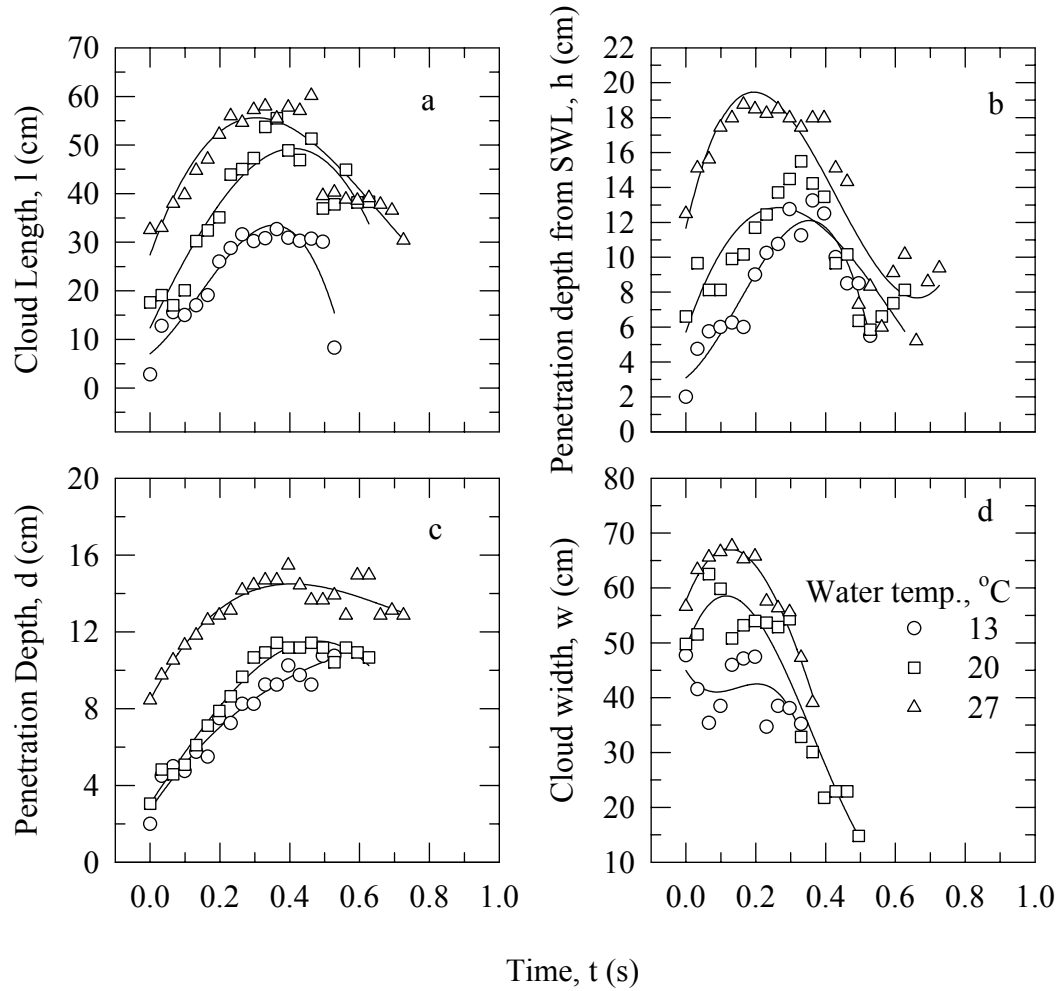


Figure 6.27 Time evolutions of the bubble cloud at different water temperatures, wind 13 m s^{-1} : a) cloud length; b) cloud penetration depth; c) cloud penetration depth below still water level; d) cloud width. The solid lines are best polynomial fit.

obvious: In panel (a) the cloud length values at 13°C (circles) exceed those at 20°C and 27°C in some moments. In panel (b) the values of the cloud thickness d are almost the same for the three temperatures for the half of the clouds lifetime, then the values for 27°C go down quite differently from the others. Panel (c) shows approximately equal values for

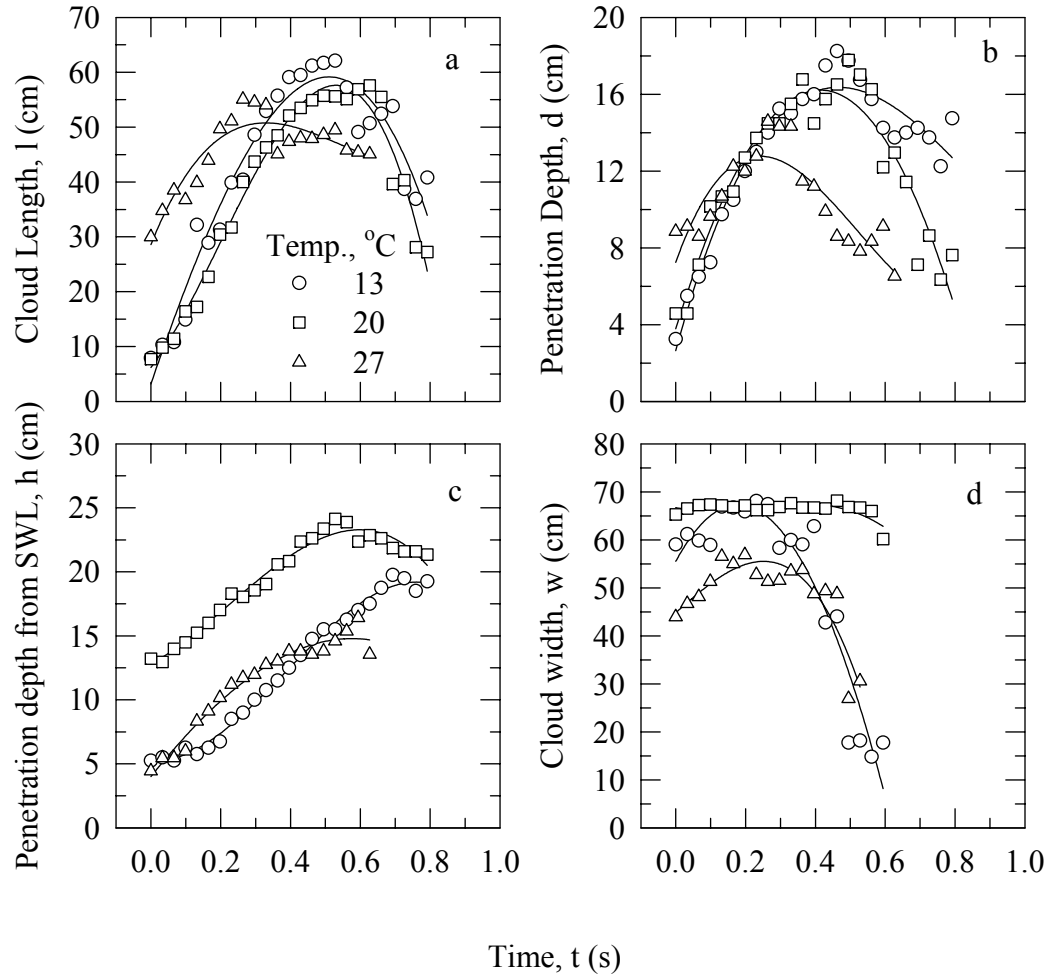


Figure 6.28 Another set of bubble cloud parameters' time evolutions at different water temperatures. Wind speed 13 m s^{-1} . The solid lines are the best polynomial fit.

the penetration depth h for both low and high temperatures, while in panel (d) no ordered behavior for cloud width w is either observed. The results for cloud dimensions are repeated in the trends for the void fractions from side and top view α_{side} and α_{top} at the three water temperatures. These results are in contrast with the laboratory study made by

Hwang et al. (1991) . One suggestion explaining the discrepancy between the two studies is the mechanism of bubble clouds generation: wave winds in the one case and water jet in the other. Previous experiments with water jet (Koga, 1982; Detsch and Sharma, 1990; Hwang et al., 1991) demonstrated that the surface tension and jet velocity governed the bubble production. Obviously, at a fixed jet velocity the surface tension, which is a function of the temperature, remains the only important parameter and the results followed an ordered trend. It is quite possible that in the case of wind waves the role of the surface tension in the bubble clouds production, respectively cloud parameters, is influenced by the wave field conditions, especially the wave phase velocity. The band of wave frequencies, consequently the range of wave periods, lengths and phase velocities, characterizing the random wave field at fixed wind speed would cause a range of possible cloud dimensions. Changes in the cloud parameters brought by the temperature can be masked by the wave-field-caused changes. So that, even if the temperature has some influence on the cloud parameters, it is vaguely revealed from the time evolutions.

6.4.6.2 Statistical Characteristics

Does the temperature change the probability structure of the cloud parameters? It seems the answer is affirmative. Moreover, the probability curves reveal the temperature effects better than the time evolutions. And still, the trend of the changes is not always very clear, especially for cold water.

Figure 6.29a-d represents the bubble cloud parameters' (l , d , w , and α_{side}) PDFs for wind 13 m s^{-1} at the three different water temperatures. The range of possible cloud lengths at 27°C narrows from the shorter side (Figure 6.29a, dotted line), i.e. clouds shorter than about 20 cm are not observable in warm water. This is a second sign for the

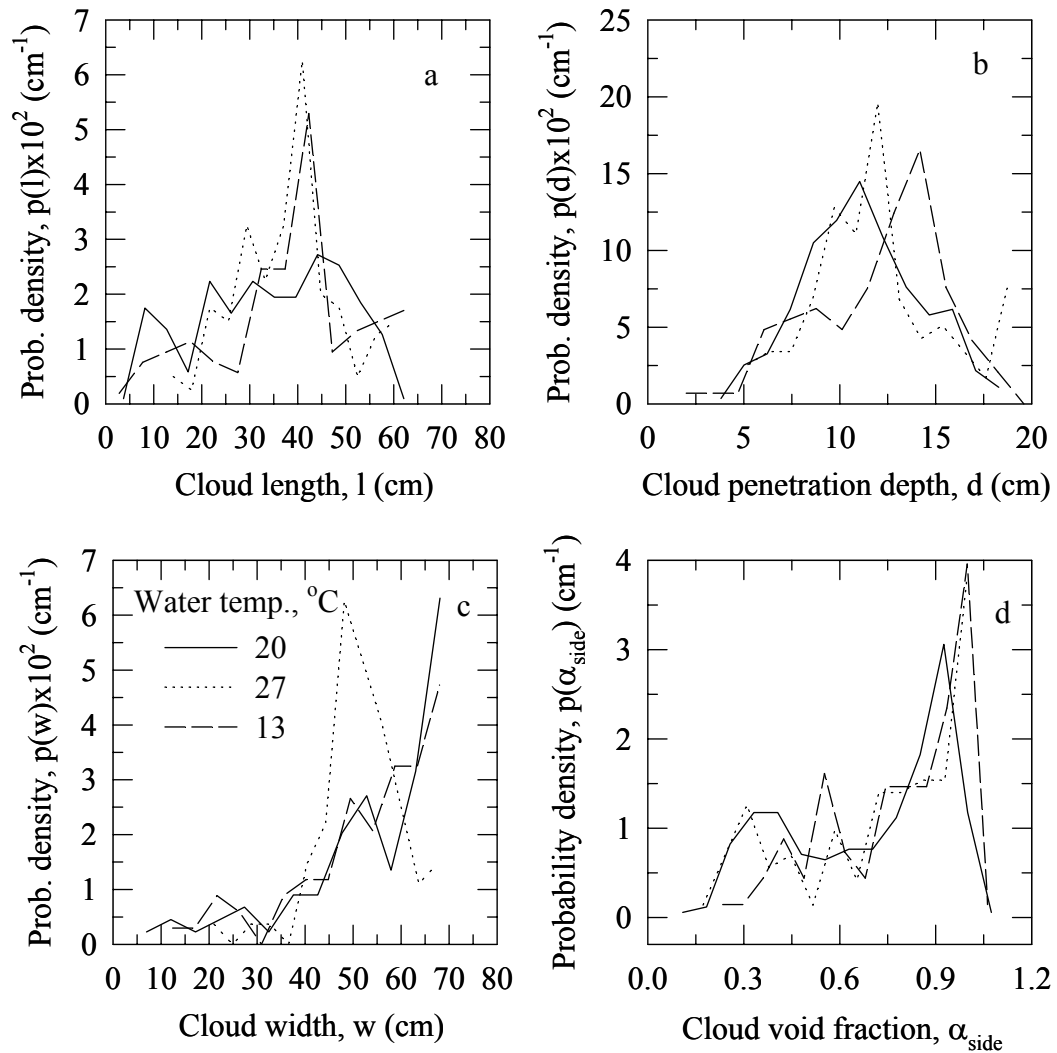


Figure 6.29 PDFs for bubble cloud parameters l , d , w , and α_{side} at different water temperatures. (Wind speed 13 m s^{-1} .)

eventual enhancement of the cloud length with increasing water temperature. In addition, the probability of measuring different lengths is not spread over the whole range, as in the case of 20°C. In contrast, it concentrates around a specific value reaching 30% (= 6 x 5 cm bin) for the band centered at 40 cm. For cold water (dashed line in Figure 6.29a) the range of possible lengths overlaps that for 20°C and increases up to 67 cm. Again, the probability for a specific value concentrates: 25% for the band around 40 cm. The cloud penetration depth PDF (Figure 6.29b, dotted line) for warm water decidedly shifts toward higher values and the probability of observing depths around 12 and 18 cm is 19 and 8 % (bin 1 cm), respectively. The range of possible depths at 13°C (dashed line in Figure 6.29b) also moves toward higher values, but the probability peaks for depths around 14 cm and after that quickly decreases. Though not very clearly (the range of depths for cold and room temperatures are similar), this result confirms the previous observations that the cold water hampers the penetration of air bubbles, while the warm water facilitates this act. The cloud width PDFs (Figure 6.29c) for both warm (dotted line) and cold (dashed line) water broaden very slightly toward higher values, compared with room temperature, but reach maximum probability for different sizes. In warm water the most probable (30%) cloud widths are around 47 cm, while in cold water clouds assume sizes around 65 cm with 25% probability. This result seems reasonable considering that the cold water hinders the penetration, hence in cold water the cloud spreading is mainly in the horizontal direction since it is prevented from going deeper, whereas the enhanced penetration of air in warm water results in confinement of the cloud to narrower horizontal zones. While the

temperature effect is not very strong for cloud dimensions, possibly masked by the wave action, for the void fraction, the surface tension eventually overcomes the wave conditions. This can be inferred from the displacement of the peaks of the void fractions associated with the initial and residual stages of the clouds for warm and cold waters (Figure 6.29d, dotted and dashed lines respectively) . For both cases (13 and 27°C) the initial voids are higher than those at room temperature (0.96) and are observed with higher probability (28% vs. 21% for room temperature) . But the residual peaks are shifted. For warm water the void fraction of the remnant bubbles goes below 0.3, which implies that the bubbles decay slower and survive longer in the wave trough. There, in the flat elongated trough before the violent intrusion of the next wave the bubble motion is affected by the buoyancy and surface tension. Indeed, according Figure 6.12g the vertical velocity of the bubbles in the wave trough has a value close to that of their rise velocity, and as in warm water the surface tension is lower, the bubble contraction is weak, so that they are more long-lived. In contrast, for cold water the probability to observe voids less than 0.45 is less than 7%. The maximum probability for residual voids in cold water are around 0.5, which implies that the bubbles live less because they are at shallower depths, and the higher surface tension squeezes them quicker.

In summary, the changes of the probability structure of the cloud parameters in warm and cold water generally points towards expected behavior. However, this is much better expressed in the trends in warm water than in cold water. There are occasions when the behavior of the cloud parameters in cold water is surprising, especially in comparison with that for 20°C. It is possible that the difference

between the temperatures of the air in the bubbles (always 20°C) and the water around them is not sufficiently high (7°C) for clear establishment of the trends. Further, the saturation of the water with gases may play a role for the nondistinctive appearance of the effect. When the water is warm, the water is closer to its saturation and the mass flux from the bubbles is less, whereas cold water is less saturated and the flux of gases from the bubbles is larger so that they dissolve so quickly that other effects can not happen.

All observation of the changes in the probability structure due to temperature differences of the water described for 13 m s⁻¹-wind above are repeated for 10 m s⁻¹ (Figure 6.30a and b) . The shifts of the probability peaks for warm and cold water are the same; the magnitude of these shifts are different. For 16 m s⁻¹ wind speed (Figure 6.30c) the peak in the probability curve for warm water behaves as for the other winds, in that it moves towards higher depths. For cold water, however, the consistency is lost and the peak moves to the lower depth values. Actually, this is what is expected and the ideal temperature effect – increasing the penetration depth with temperature increase – is well established for 16 m s⁻¹. This is further evidence in support of the vaguely observed temperature effects until now. Further, a sign for the temperature influence is that: if the probability peaks for 20 and 27°C are tracked for the three wind speeds (solid and dotted lines in all panels), it is seen that the increase of the penetration depth with wind increase is stronger for 27°C as warm water facilitates the penetration of bubbles.

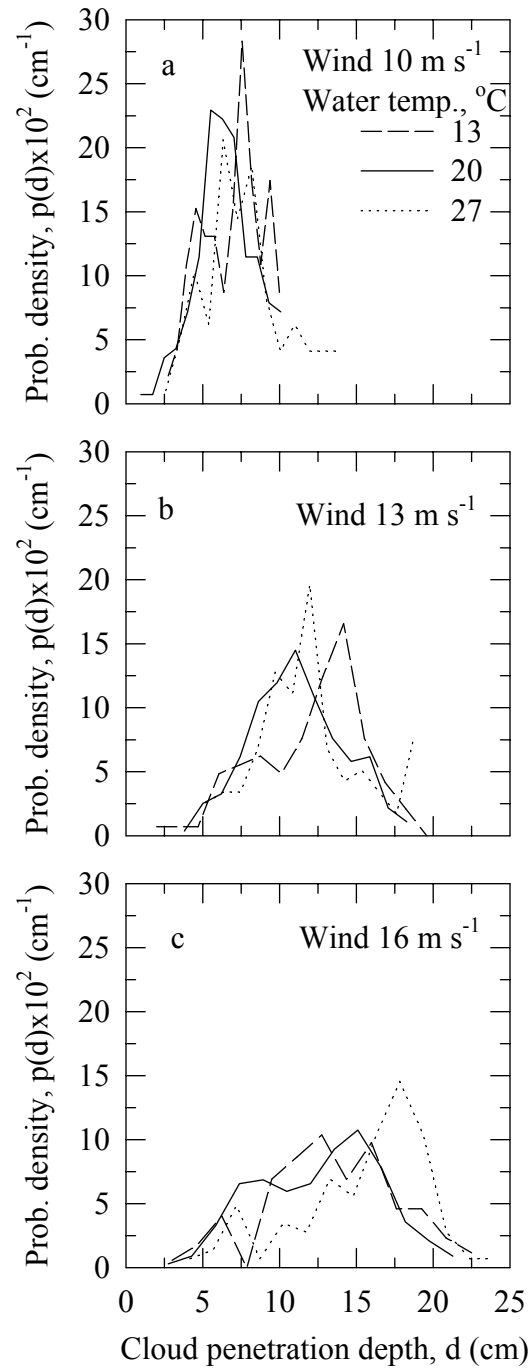


Figure 6.30 PDFs for bubble cloud penetration depth at different water temperatures and wind speeds of 10 m s^{-1} (a), 13 m s^{-1} (b), and 16 m s^{-1} (c).

The compendious numbers for bubble cloud length, l , penetration depth, d , and “side” void fraction, α_{side} , for the three water temperatures and wind speeds 10, 13, and 16 m s⁻¹, obtained with the second method of averaging, are listed in Table 6.6.

Table 6.6

Wind m s ⁻¹	l			d			α_{side}		
	13 °C	20 °C	27 °C	13 °C	20 °C	27 °C	13 °C	20 °C	27 °C
10	19.58	19.94	25.75	6.48	6.081	7.19	0.66	0.648	0.648
	6.389	8.885	3.81	0.75	1.631	1.43	0.17	0.087	0.067
13	35.81	31.45	35.76	11.37	9.99	11.32	0.761	0.685	0.707
	8.663	6.06	7.25	1.361	1.67	1.5	0.090	0.062	0.075
16	41.62	46.94	44.04	12.74	13.06	14.75	0.777	0.734	0.749
	13.81	5.651	7.14	2.499	1.262	1.36	0.058	0.079	0.046

6.4.6.3 Temperature and Wind Dependence

With these numbers the temperature and wind dependencies of the three cloud parameters (l , d , and α_{side}) are plotted in Figures 6.31 and 6.32. The comparison of these dependencies supports most clearly the suggestion that the temperature effect is present but is weak, and is easily masked by the stronger wind influence. Although the variances in Figure 6.31 are large and the experimental points a few, lines of a best polynomial fit are drawn for each wind speed only to show more clearly that there is a very slight increase of the cloud parameters with the temperature; sometimes there is no trend at all. This observation is consistent with the Wu’s conclusion (1988b, 1992b) of a lack of some systematic trend of the whitecaps coverage with the water temperature. Inasmuch, in Figure 6.32 a - c the trend of increasing of cloud parameters with the wind is stronger. It worth noting that observed trends are equally small for both, temperature

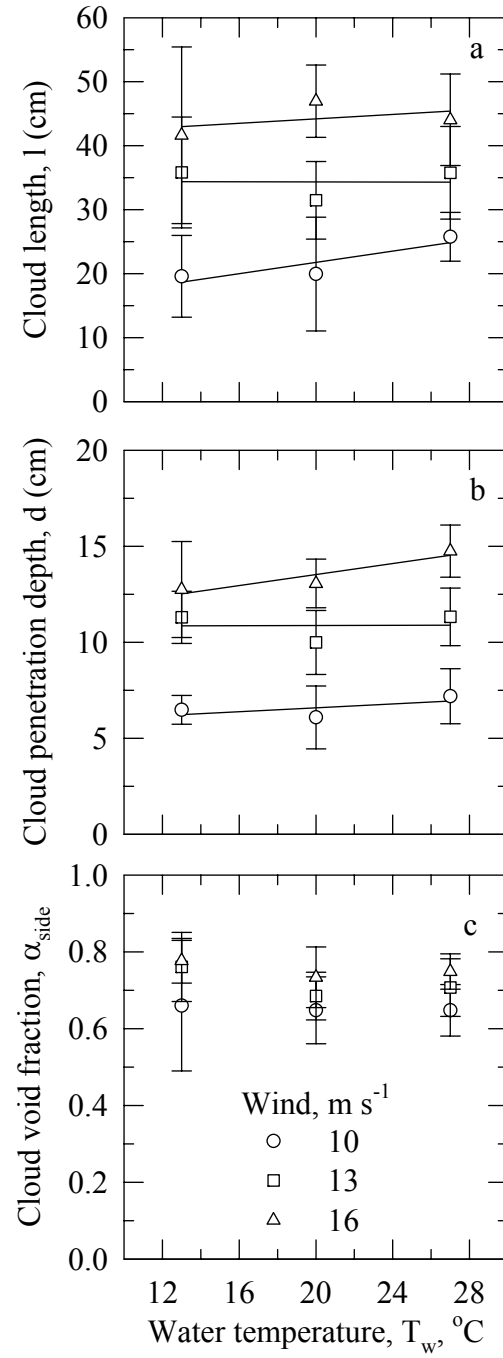


Figure 6.31 Temperature dependence of the bubble cloud parameters at different wind velocities: 10, 13, and 16 m s^{-1} : a) cloud length; b) cloud penetration depth; c) cloud void fraction from side view.

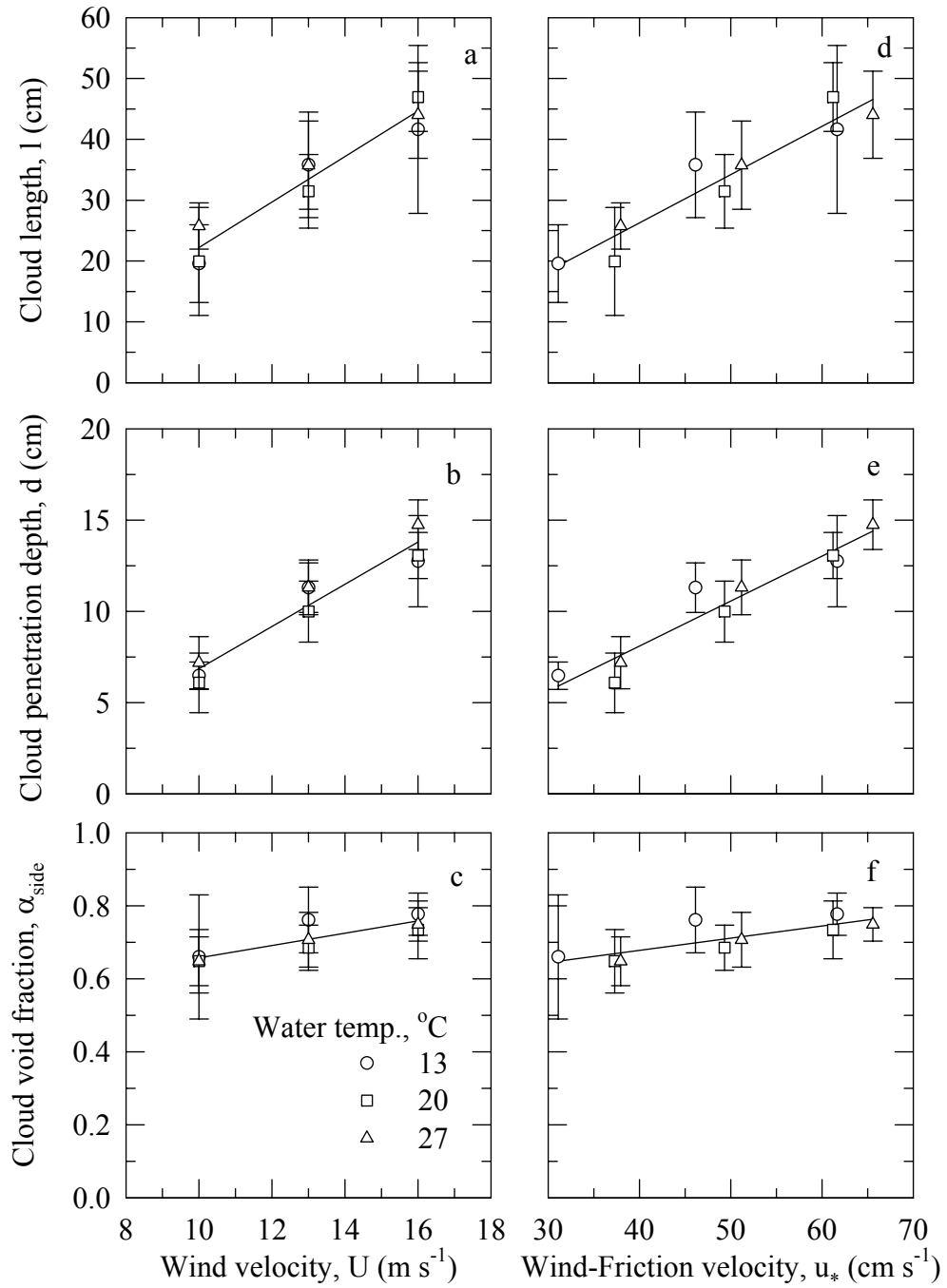


Figure 6.32 Wind dependence of the bubble cloud parameters at different water temperatures. Dependence on reference wind U : a) cloud length; b) cloud penetration depth; c) “side” void fraction. Dependence on wind-friction velocity u_* : d) l ; e) d ; f) α_{side} .

and wind, dependencies of the void fractions and the discussion in Figure 6.29d for the residual peaks of the voids loses its meaning when the average void fraction values are used. In Figure 6.32 a -c reference wind velocity, $U \text{ m s}^{-1}$, measured directly in the tank is used. As the conversion of U in friction velocity u_* , cm s^{-1} , uses drag coefficient C_D , which is temperature dependent (Smith, 1988), it is interesting to see how the bubble cloud parameters change with u_* . Using data from Smith (1988) for C_D at appropriate for this study water - air temperature differences ($\pm 7^\circ\text{C}$) the wind velocity U is converted in wind friction velocity u_* by a bulk formula $u_*^2 = C_D U^2$ (Geernaert, 1990). Wind dependence of the cloud parameters on u_* is plotted in Figure 6.32 d - f and examined. The results show that again the wind dependence of the cloud characteristics is stronger than the temperature dependence although the temperature effect on u_* is taken into account via C_D .

6.4.7 Bubble Size Distribution

6.4.7.1 Measured Bubble Size Distributions

The size distributions of the bubbles within the cloud were obtained from the images with a small FOV. The procedures of digitizing and extraction of the values of parameters necessary to be measured are presented in §6.3. The resulting bubble size distributions, $N(d)$ in $\mu\text{m}^{-1} \text{ m}^{-3}$, for three wind speeds, 10, 13, and 16 m s^{-1} , are given in Figure 6.33a. The slope of the distribution is better fitted with the law $N(d) \sim d^{-2}$ than with d^{-4} because the bubbles are rather big. This is consistent with Wu's considerations

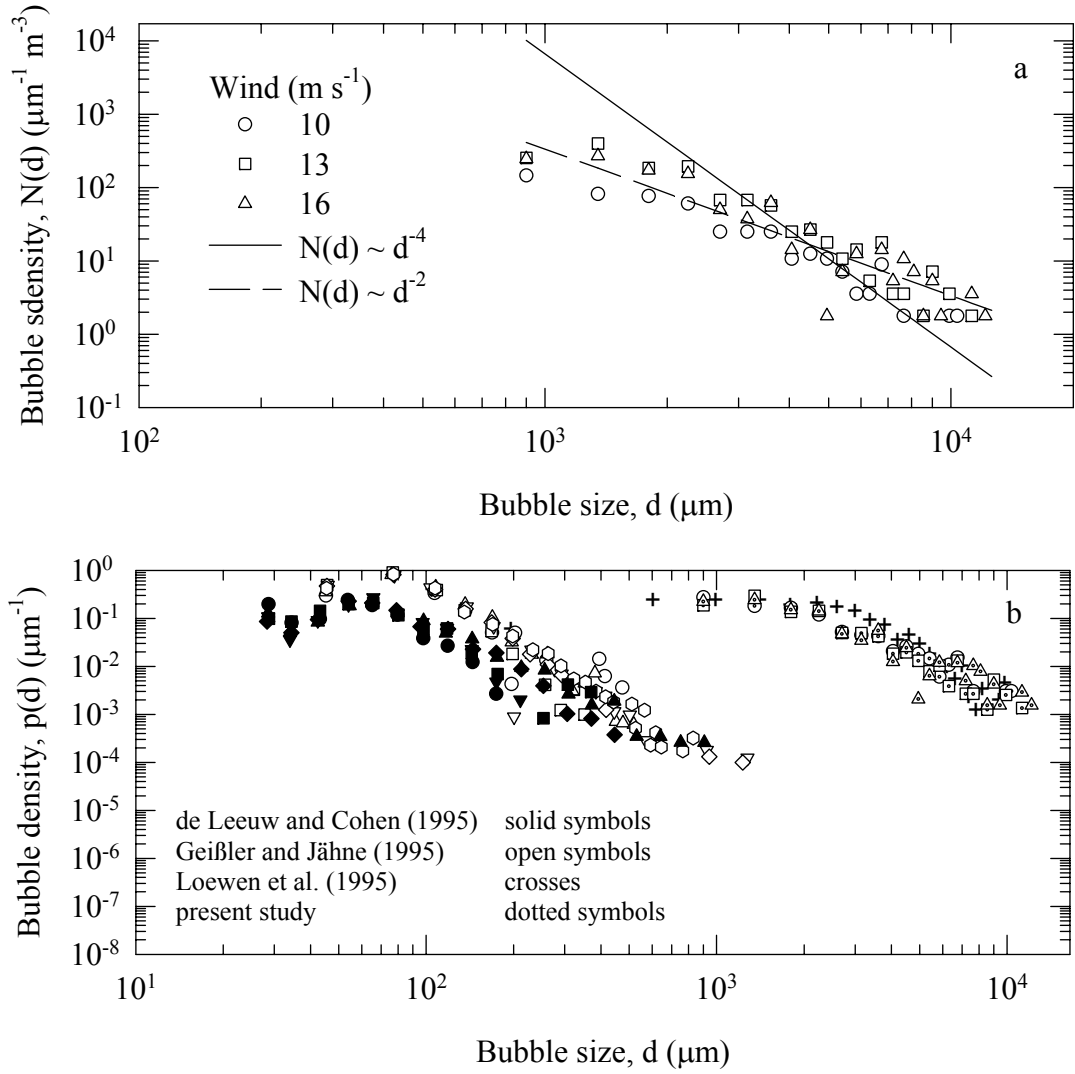


Figure 6.33 Bubble size distributions: a) measured; b) comparison with others.

(1994) that the bubbles in the background population, following d^{-4} , change this trend to d^{-2} for a while in the presence of the large bubbles produced by the breakers. The probability density $p(d)$, in μm^{-1} , is compared with those from the other experiments, introduced in §3.6.5, in Figure 6.33b. The agreement with the Loewen et al. (1995) data, which are for a similar size range (0.3 - 5 mm), is good, though Loewen's data may

follow well a d^{-4} law. This arises from only having a limited range, only one decade, of diameters. Note the confusing at first glance discontinuity between the sets for small and large bubbles in Figure 6.33b. The reason is the normalizing done in order to obtain the probability density $p(d)$.

6.4.7.2 Bubble Size Distributions from Measured Void Fraction

A worthy merit of the acoustical method in measuring the bubble population is the possibility to obtain bubble size distribution from measured void fraction. This was well exemplified by Melville et al. (1995) and discussed in §3.7.1. However, most of the techniques available for bubble sizing, including the acoustical, reach their limit in measuring the voids in the very initial moments after the breaking of the wave. A possibility to infer the bubble size distribution from measured void fraction of the clouds is considered here. The following describes the idea how to realize this goal and gives examples with data from the literature and from this investigation.

In Figure 6.34a data of bubble density (number of bubbles N in a unit volume, m^{-3} , and over a size band, μm^{-1}) from different investigations are gathered. The data are collected under various conditions (§3.6.5). For the diversity of measuring techniques and experimental conditions the agreement among the data and the theoretical expression proposed by Wu (1992a), is remarkable. An interesting observation in this figure is that apart from the general trend down of bubble density with the bubble size,

the sets of experimental points for small and large bubbles are not lying on one line. This clearly indicates the difference between the bubbles within the background and transient population obeying different physical processes. Also, the change of the power law from d^{-4} to less power is evident. Finally, the higher than expected values of bubble density for large bubbles supports the idea for their importance (Keeling, 1993). This points towards the necessity of further investigations in the range connecting the both sets (10^2 - 10^3 μm).

The coefficient in the Wu's expression for bubble size (Wu, 1992a) is derived on the base of data reported by Kolovayev (1976) and Johnson and Cooke (1979). A properly chosen coefficient with the same dependence on the bubble size (r^{-4}) would match the individual sets of data in Figure 6.34a very closely. Therefore, accepting the bubble size dependence from the general description of the bubbles (§3.6) over a proper range, it is necessary to find out the correct coefficient in the expression $N = Cr^{-4}$. It is possible to determine the coefficient C from the measured void fraction α . If there are N_i , $i = 1, 2, \dots$, bubbles with radii r_i in the range $[r_1, r_2]$, hence volumes $V_i = \frac{4}{3} r_i^3$, in a unit volume of gas-water mixture, the void fraction of it would be

$$\alpha = \int_{r_1}^{r_2} N_i V_i dr$$

The solution of this integral is

$$\alpha = \frac{4}{3} \pi C \times 10^{18} \ln \frac{r_2}{r_1}$$

where the coefficient 10^{18} comes from the units unifying. From this expression coefficient C is in the form:

$$C = \frac{4}{3\pi} 10^{18} \alpha \frac{1}{\ln \frac{r_2}{r_1}}$$

To use this expression for C to get bubble distribution from the void fraction, two assumptions have to be well justified. These are: 1) to use only the dependence $N \sim r^{-4}$ from the complete bubble size spectra, Figure 3.2, and 2) to chose the range of sizes $[r_1, r_2]$. The arguments for justifying the first assumption are the following: First, it is known, that the slope of the bubble distributions in its third segment of sizes ($> 100 \mu\text{m}$, §3.6) reported in the literature vary from -2 to -6 (Table 3.1) . However, the dependence r^{-4} , proposed by Wu is widely accepted and Figure 6.34a proves that it describes adequately the data originating from a wide range of conditions. Second, the void fractions obtained from the data in Figure 6.34a, plotted in Figure 6.34b, show clearly that the bubbles in this segment have the main contribution for α , though they are not the most numerous. Therefore, it is justified to use only the segment r^{-4} from all three parts in the complete bubble spectrum for the calculation of the coefficient C . Figures 6.34a and b also help in the choice of the range of size over which the calculation to be applied: the slope r^{-4} is equally well fitted for the sizes from 30 to 500 μm (Melville et al., 1995; Geißler and Jähne, 1995) and above 1 mm (Loewen et al., 1995). Also, the voids from the bubbles bellow 50 μm are negligibly small. A trial of this procedure is made over the size range 50 μm – 5 mm using the void fractions calculated from the three sets of data in Figure 6.34a.

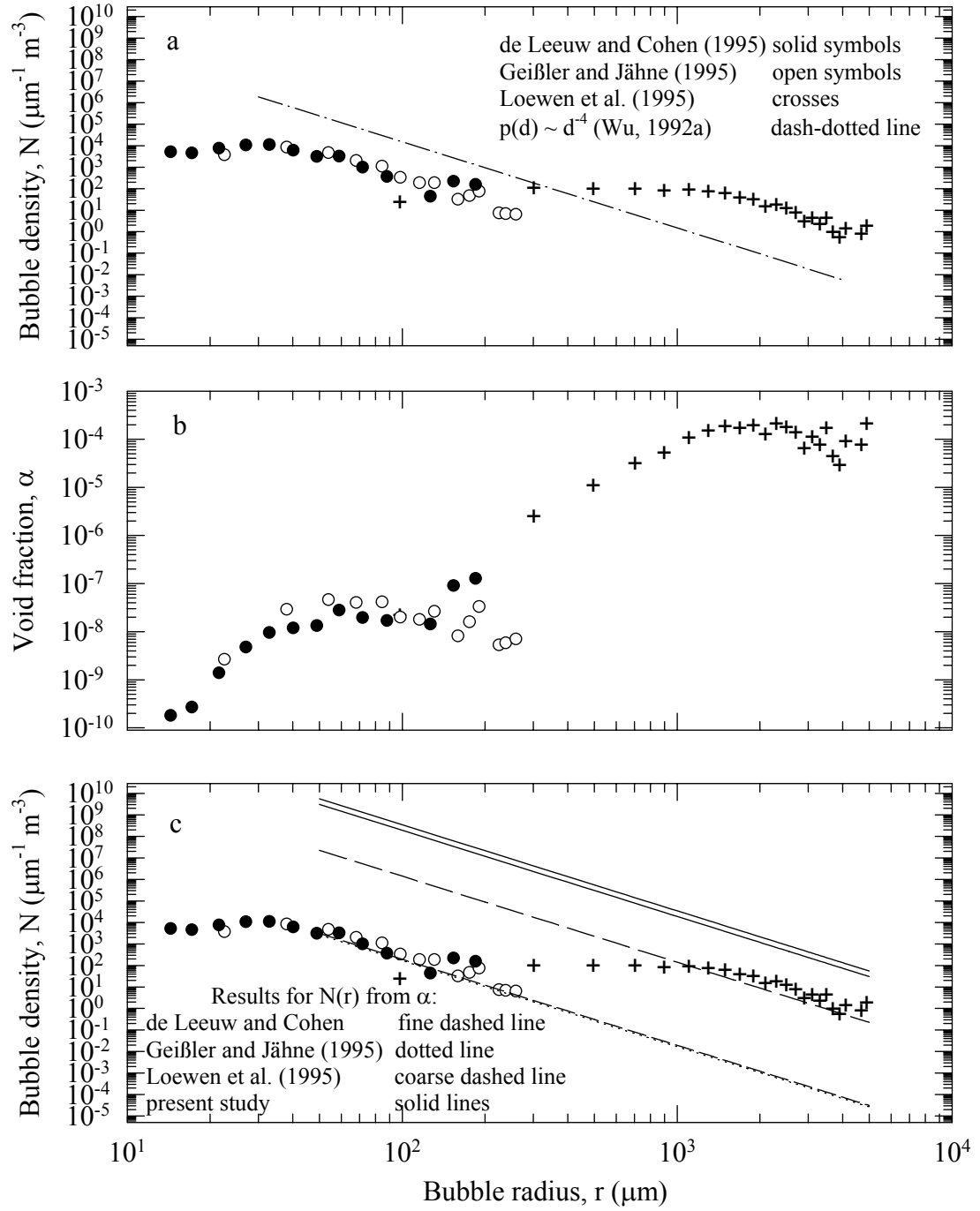


Figure 6.34 Bubble size distributions calculated from the measured void fractions: a) proper coefficients would match the sets; b) void fractions from the bubble size distributions; c) bubble size distributions (lines) calculated from measured void fraction (the symbols are real data for comparison) .

For each void fraction obtained from the corresponding size distributions a coefficient C is calculated and used to find the bubble density by $Cr^{-4} = N_{\text{calculated}}$. The calculated bubble densities are presented in Figure 6.34c with dashed and dotted lines and the real data from different authors are plotted for comparison. Cutting from these lines the parts beyond the resolution possible for a given technique, the bubble density calculated from the void fraction is obtained and it seems to represent the real data closely.

This procedure was applied for the mean values of the void fractions measured in this study from a side and top view, Table 6.4. The result is presented in Figure 6.34c with solid lines and shows that voids of order 60% are produced by a dense ensemble of 3.4×10^8 bubbles with radius 100 μm , from about 2000 bubbles with radius 2mm, and so on for all other radii. Since most of the bubble size distributions reported in the literature are for the background population, this numbers are too high in comparison with them. Results close to those are reported by Blanchard and Woodcock (1957): 10^8 bubbles over 100 - 500 μm . Monahan (1993) reports bubble concentration of order of $10^7 - 10^8 \mu\text{m}^{-1} \text{m}^{-3}$ for the initial bubble clouds, termed by him α -plumes.

6.4.8 Scaling of the Parameters

6.4.8.1 The Scaled Values

Laboratory versus field experiments is a dilemma challenging for all researchers. Each of the two approaches has its pros and cons. The laboratory conditions meet unavoidable constraints as limited wind fetch, confined water flow, insufficient water depth. However, the laboratory investigations can provide well controlled

experimental conditions in which major physical processes and relations can be systematically observed and quantified. Also, they provide data to improve the analytical and numerical models. Finally they guide how to overcome the problems and plan field measurements. The last ones are undoubtedly more important as the processes are natural and in their full complexity and interplay with all environmental parameters. Unfortunately, this exactly is the reason for intractable difficulties. The merit of the present laboratory study is the systematic observation and quantification of the main bubble cloud characteristics and their dependence on wind and temperature.

The bubble cloud dimensions, length l , thickness d , penetration depth h , and width w are scaled with the wave length L and significant wave height H_s . The time in cloud temporal variations is scaled with the wave period T . The absolute values presented in Figures 6.13, 6.15, and 6.16 are now plotted in Figures 6.35, 6.36, and 6.37 respectively, with these scaled values. The process of cloud appearance, growing and decaying can last for almost the entire wave period, Figure 6.35. All parameters reach their maximum values at around $0.8T$. But also, the whole process may finish for approximately half wave period, $0.6T$, at any wind speed as well, Figure 6.36. Figure 6.35 shows that the maximum bubble cloud length produced by a wave at 13 m s^{-1} wind is about $0.7L$; the maximum penetration depth (d or h) is about twice the significant wave height, $2 - 2.5H_s$; a cloud may easily spread at a maximum width close to one wave length, $0.98L$, and perhaps more than that (recall, there were restrictions of cloud width

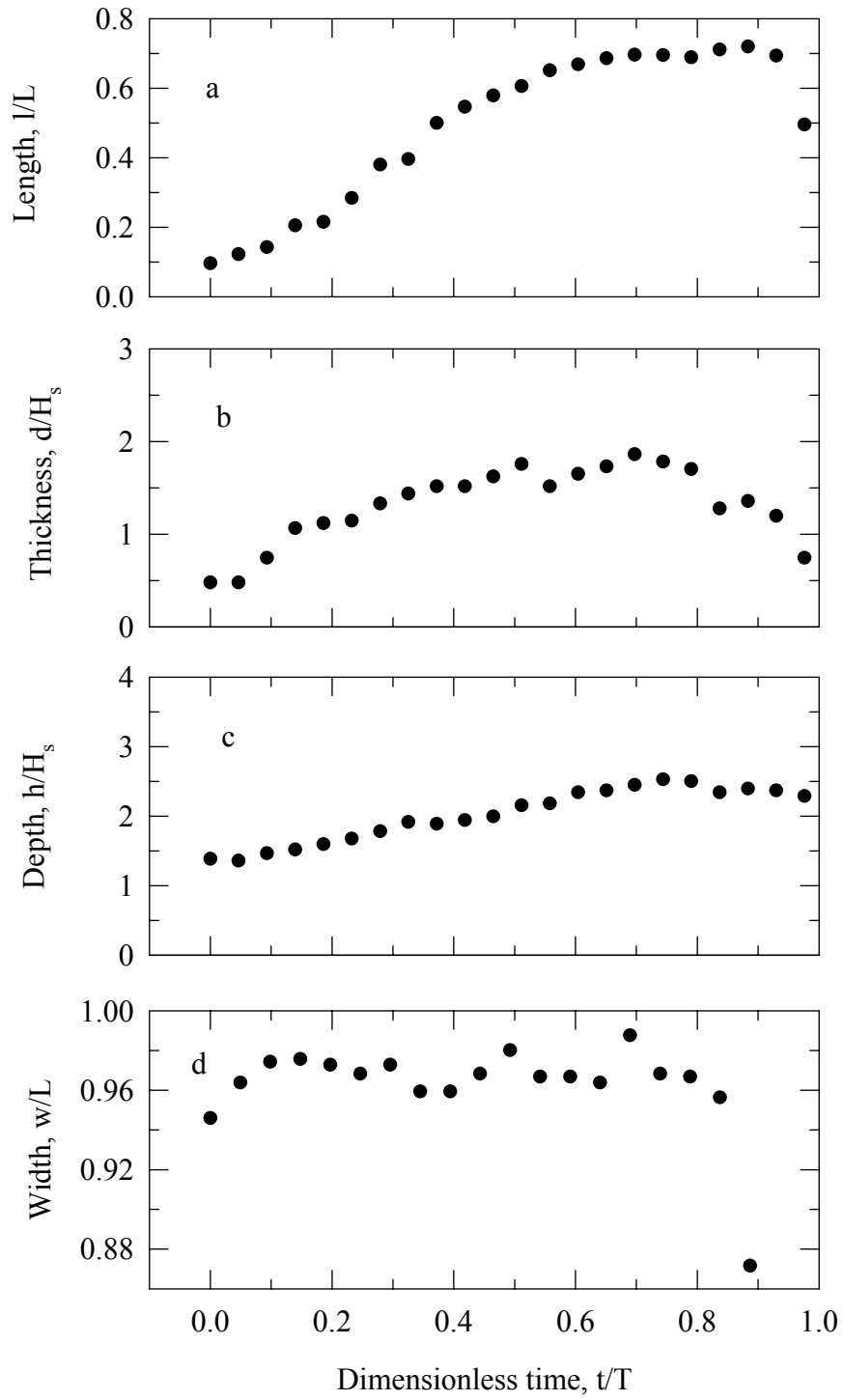


Figure 6.35 Time evolutions of the cloud parameters in Figure 6.13 scaled with the corresponding wave characteristics. (Wind speed 13 m s^{-1} .)

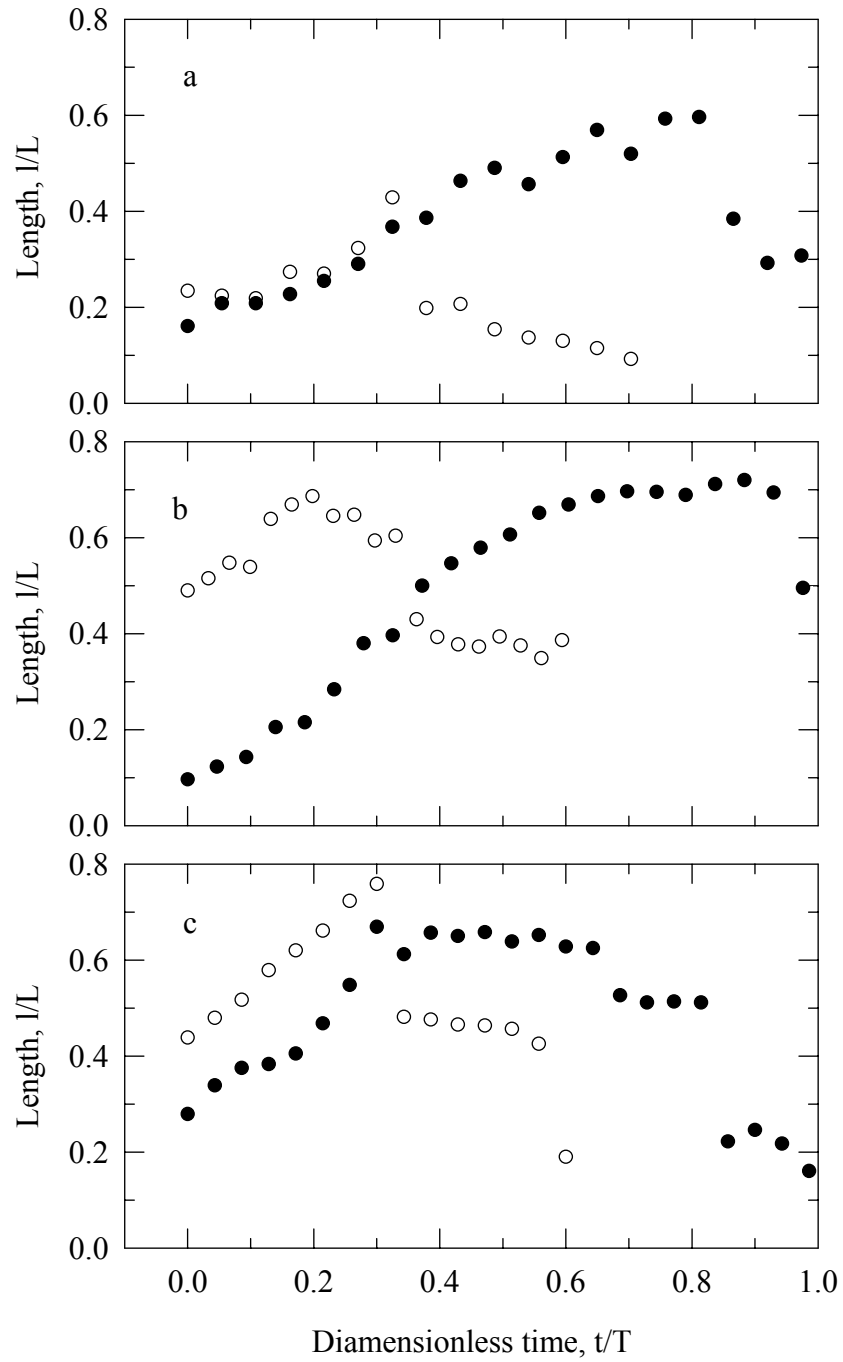


Figure 6.36 Same as Figure 6.15 scaled with the corresponding wave characteristics.

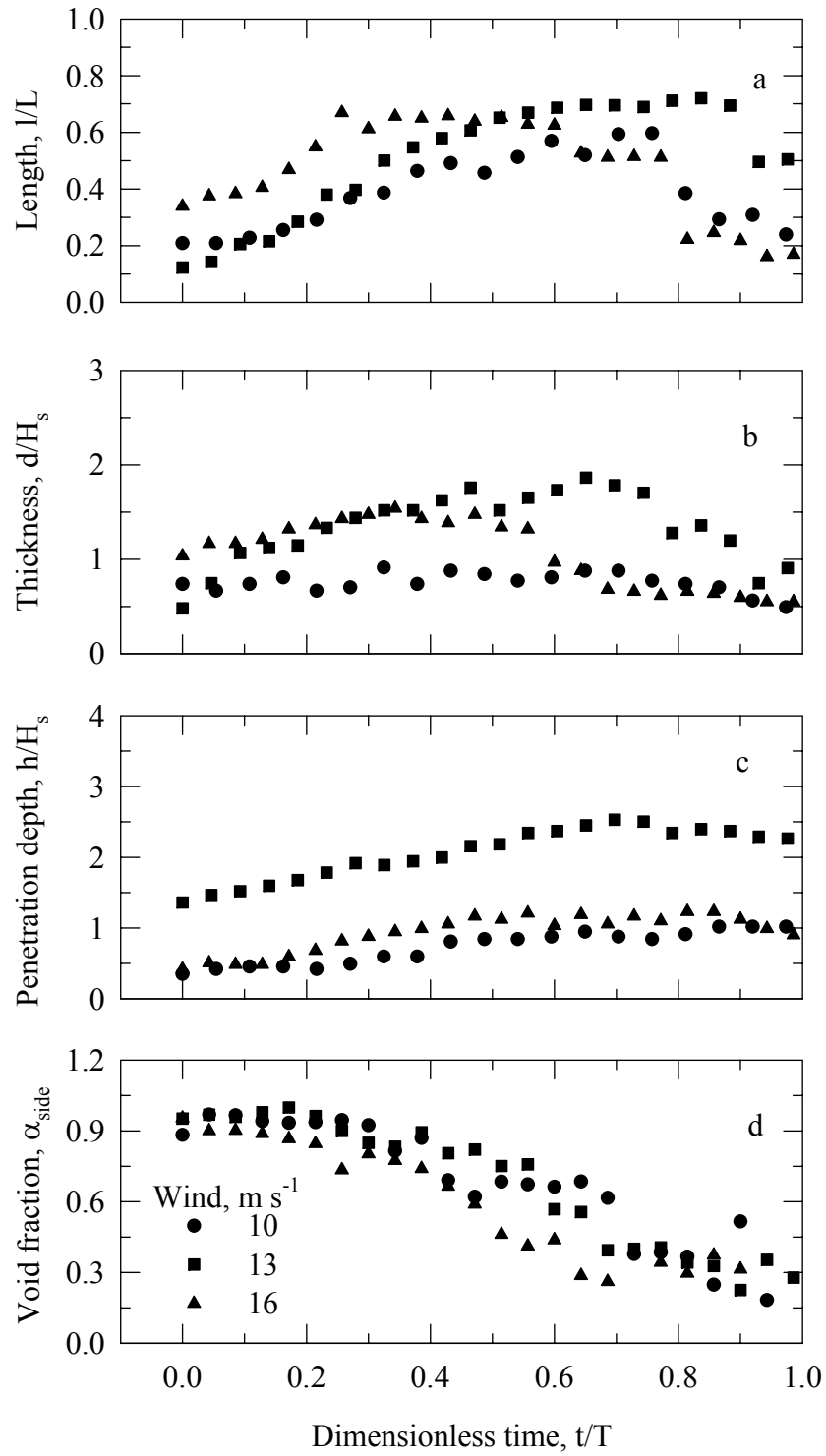


Figure 6.37 Same as in Figure 6.16 scaled with the corresponding wave characteristics.

observations from the tank walls) . Figure 6.37 depicts approximately the same maximum value of the cloud length for different winds and wider range for the maximum penetration depth ($1 - 2H_s$) . The void fraction of the clouds produced at different wind speeds is maximum at around $0.2T$, gradually decreases to 60% at about half the wave period ($0.5T$), reaches about 20% for one wave period T . Voids less than 20% persists to about $1.5 - 2T$.

The wind dependence of the averaged cloud parameters, Figure 6.38, shows that for range of winds $10 - 16 \text{ m s}^{-1}$ the cloud length increases from $0.3L$ to $0.5L$, the penetration depth from $0.9H_s$ to $1.2H_s$, cloud width starts with $0.6L$ and likely reaches one wave length. The void fraction does not show noticeable changes from the averaged values 63% as the increased volume of the entrained air is homogeneously mixed in steadily increasing volume of the cloud. Though the variances in these graphs are wide, reflecting the temporal changes of the cloud parameters, trends of increasing of these with the wind can be discerned. These trends are shown with the solid lines in all panels in Figure 6.38. They are plotted as the best fit of the experimental points to a power-law in the form $CP=aU^b$, where CP stands for Cloud Parameter, U is the wind velocity, and a and b are coefficients. With the specific coefficients for these lines, the cloud parameters' wind dependency is presented by:

cloud length	$l/L = 0.06U^{0.74}$
--------------	----------------------

cloud penetration depth	$d/H_s = 0.52U^{0.28}$
-------------------------	------------------------

cloud width	$w/L = 0.36U^{0.2}$
-------------	---------------------

$$\text{cloud void fraction } \alpha_{\text{side}} \quad \alpha_{\text{side}} = 0.58U^{0.05}.$$

The occasional limitations for the bubble cloud length and width brought for the highest wind (16 m s^{-1}) by the FOV and tank width, respectively, may cause the last experimental points in panels a and c, Figure 6.38, to limit the increasing trend. These trends change from the solid to dashed lines when last experimental point, for 16 m s^{-1} , is not taken into account. For these cases the power-law variations are presented by:

$$\text{cloud length} \quad l/L = 0.007U^{1.62}$$

$$\text{cloud width} \quad w/L = 0.124U^{0.64},$$

which are believed to be closer to the true variations.

As for many applications what is observable from the bubble clouds is their area on the water surface, the cloud area from top (and side) view is presented in Figure 6.39. The area ratios, A_{top}/L^2 or A_{side}/LH_s , exhibit maxima in their time evolutions similar to the time history of each of the parameters. The “top” area has a minimum value of $0.1L^2$ and may reach a maximum of $0.5L^2$ for the half of the wave period, $0.5T$, Figure 6.39a. By the end of the wave period, the area from top view decreases below $0.2L^2$ and probably only small patches persist for more than one wave period. For the “side” area the range of variations with wind speed is from $0.2LH_s$ to $0.6LH_s$, Figure 6.39b. The temporal development of the side area is different from that of the top area: some maxima occur about $0.7T$ while other at $0.3T$. Again, the reason could be the band of wave frequencies. In addition, as it was shown in the previous discussion, the cloud

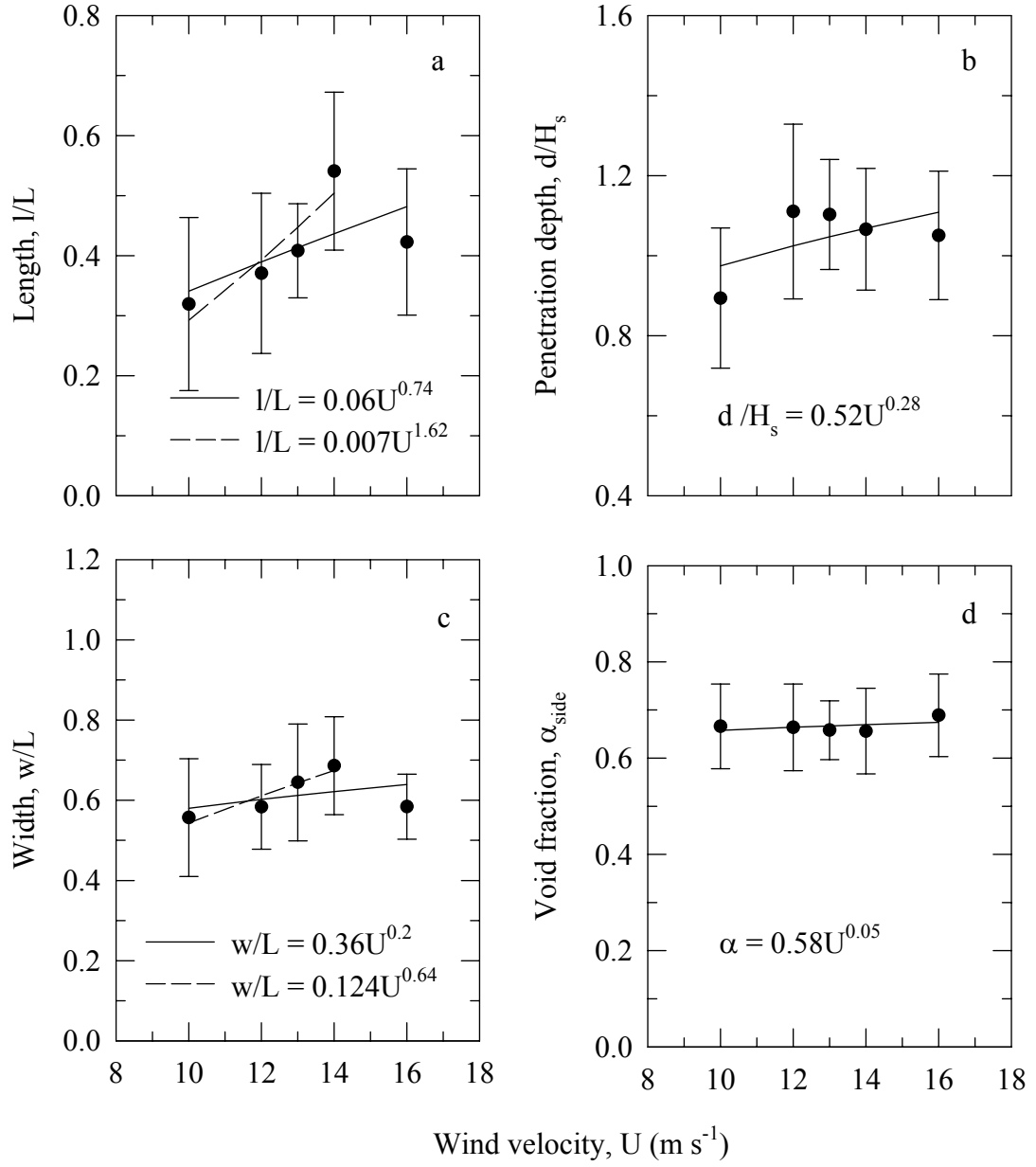


Figure 6.38 Wind dependence of the scaled bubble cloud parameters: a) cloud length; b) cloud penetration depth; c) cloud width; d) cloud void fraction. The solid lines are a power law fit to the experimental points. The dashed lines are a fit without the point for 16 m s^{-1} -wind.

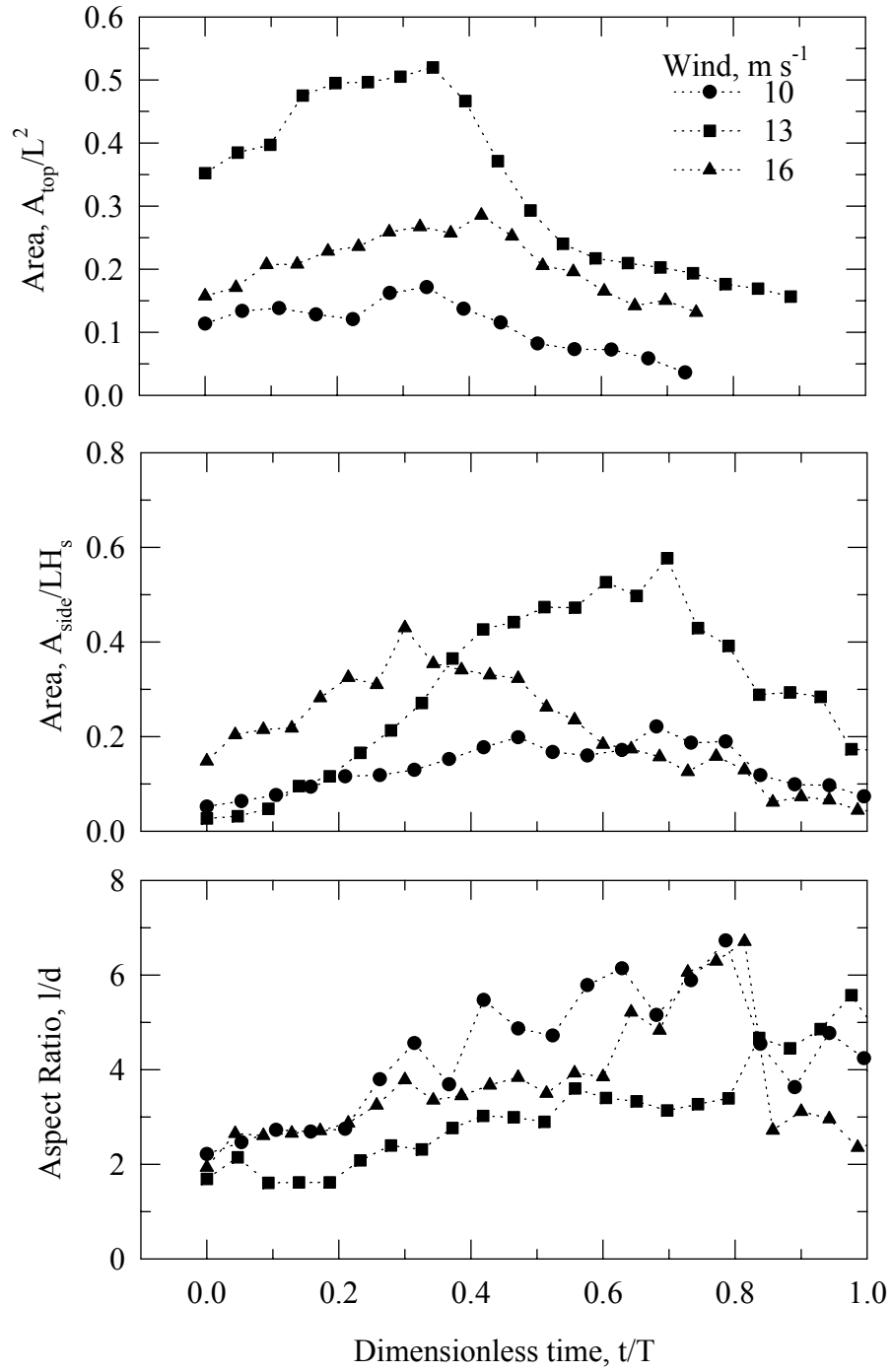


Figure 6.39 Additional cloud parameters scaled with the wave characteristics at different wind speeds: a) area from top view $A_{\text{top}} = wl/L^2$; b) area from side view $A_{\text{side}} = ld/LH_s$; c) aspect ratio l/d .

width increases at a higher rate than the penetration depth, hence the faster increase of the top area compared to the “side” area. The aspect ratio of the cloud given by the ratio of the cloud length and depth, l/d , generally increases from 2 to 6 up to $0.8T$, then no systematic behavior can be noted.

6.4.8.2 Comparison with Others

Kalvoda (1992) commenced the systematic investigation of the bubble clouds in Air-Sea Interaction laboratory and this study is a continuation of his work. As his results are for 16 m s^{-1} wind, the corresponding results from this study will be used. The FOVs, side and top, in both studies are very similar: side FOV 79 cm x 59 cm versus 77 cm x 62 cm (recall, the digitized part of the FOV in the present study is less); top view 66 cm x 50 cm versus 69 cm x 57 cm. Also, he considered three events from side view and five events from top view, which should be sufficient to reveal the basic cloud characteristics. The maximum values of the scaled cloud parameters plotted by Kalvoda are consistently lower than those reported here for all cloud parameters. The first guess for this discrepancy is the difference in the scaling parameters. Those reported by Kalvoda are smaller: average wave period of 0.71 s, hence wave length of 79 cm, and an average wave height of 12 cm versus 0.77 s, 92 cm and 11.39 cm respectively in the present study. A possible reason for the deviations in scaling parameters is the way of determining the wave characteristics: directly from the images in Kalvoda’s and from wave gauge in the present study. However, it was estimated that the differences in the scaling parameters can not account for the large differences in the absolute values of the

cloud parameters: 13 cm versus 67 cm for the length, 11 cm versus 21 cm for the penetration depth, and 8 cm versus 67 cm for the width. Therefore, it must be concluded that the clouds were differently defined in both studies. Kalvoda reported that only the clustered bubbles are considered to be in the cloud, and those which were far from clusters were not included, hence one must conclude that he considered one of the several plumes forming the cloud. Otherwise, the main trends in the temporal behavior documented by Kalvoda are similar to these reported here. Thus, it is reasonable to state that both studies complement each other, the one giving the parameters for one plume within the cloud and the other giving the parameters of the cloud as an integrity of several plumes.

The duration of the entire process of bubble cloud formation, growth and decay seldom exceeds 1 s for all realizations in this study. Lamarre and Melville (1991) also reported about the major temporal changes of variables related to breaking for a time up to one wave period. The results on temporal variations of whitecap area in field, manifestation of the bubble clouds beneath the water, reported by Snyder et al. (1983) showed almost exponential decrease in whitecap size after formation with a characteristic time constant of 1 s or less. At the other extreme are the field measurements of Dahl and Jessup (1995) who presented the entrainment depth of the bubbles for times after $3T_c$ (T_c being a characteristic time scale), and Thorpe (1982) and Melville et al. (1995), who provided observations of the bubble layer in the upper ocean for hours and days; obviously, the initial stages of bubble clouds are out of their scope. Note that all these are acoustic devices which are generally sensitive to the longer time scale evolution.

Penetration depths of bubbles in order of half the wave height is documented by Koga (1982) . Thorpe (1982) in field and Rapp and Melville (1990) in laboratory studies announced penetrations depth of order 2 - 4 wave heights, which are values consistent with those reported here.

The void fractions values cited in the literature are usually very low. The discussion in §3.7.3 notifies that the major problem is that the void ratios are reported for different volumes. Often the voids are calculated from the bubble size distributions. It is clear then that they give the voids of the background bubble population for a given volume, since only those can be counted. High void fraction values which are consistent with those reported here are that documented by Lamarre and Melville (1991) . Their average value for the void fraction is less than here (about 20% after 1/3 of the breaking moment), since they scale it with the tank width, while here the void are given in the frame of the cloud itself. Monahan (1993) summarizes void fraction values from different authors of order of 3 - 30%; the volumes, however, are not explicitly reported.

6.5 Implications of the Results

6.5.1 Mixing

The depth of penetration of the bubble clouds can be considered as the lowest bound to which the breaking waves induced turbulence extends, i.e., the near-surface mixing layer. According to results (Figure 6.38b), the depth of near-surface turbulence in this water tank increases from $0.9H_s$ for 10 m s^{-1} wind to $1.1H_s$ for 16 m s^{-1} .

Thorpe's suggestion (1992) that the bubbles can be used as tracers of the turbulence in the ocean is not conclusive. Probably it is a true statement for the small dirty bubbles that joined the background population: they behave as rigid bodies and are still small enough to follow the flow closely. But this suggestion is perhaps not correct for the large and thus more buoyant bubbles which constitute the major part of the clouds. On the other hand, the considerations on the bubble cloud velocity showed, that the downward forcing of the bubbles by the waves' action overcomes the buoyant force at least for 1/3 of the wave period (Figure 6.12). The cloud depth for this time span might give an indication of the depths reached by the turbulence associated with breaking. Assuming this as a correct statement, it would be informative to examine order of magnitude estimates of variables such as the vertical eddy diffusivity k_v and kinetic energy dissipation rate ε which can characterize the near-surface turbulence. A magnitude estimate of eddy diffusivity is given by $k_v \sim L_t^2/\Delta T$, where L_t is the integral length scale characterizing the turbulence evolving over the time interval ΔT (Tennekes and Lumley, 1972). The integral length scale L_t can be considered to be half the significant wave height, $H_s/2$. Taking the values for H_s at 10, 13 and 16 m s^{-1} wind at 20°C water temperature (Table 6.3) as a scale for the turbulent eddies associated with the wave-breaking process and $\Delta T = T/3 \approx 0.3$ s gives respectively $k_v \approx 4.1 \times 10^{-3}$, 7.6×10^{-3} and 1.1×10^{-2} $m^2 s^{-1}$. For the dissipation rate it is necessary to estimate the turbulent velocity scale, for example, taking the effective turbulent velocity $u \sim d_t/\Delta T$, and then the magnitude of the dissipation rate would be $\varepsilon \sim u^3/d_t$, where d_t can be taken as $d/2$ since the thickness of one plume within the cloud is approximately one half of the depth of

penetration d . Using for d the mean value for wind speed of 13 m s^{-1} (Table 6.4) and again $\Delta T = 0.3 \text{ s}$ the estimate for the turbulent velocity is $u \approx 0.175 \text{ m s}^{-1}$ and for the dissipation rate is $\varepsilon \approx 11 \times 10^{-2} \text{ W kg}^{-1}$.

6.5.2 Gas Exchange

With the results of this study it is possible to estimate the contribution of the bubbles with different size to the gas exchange in the initial moments after breaking. For this purpose two quantities are necessary to be estimated: the residence time of the bubbles and the area that they offer for gas exchange.

The bubble size distributions measured (§6.4.7.1 and Figure 6.33a) cover a range of bubble radii from $450 \text{ }\mu\text{m}$ to 6 mm . The rise velocity of the small bubbles ($450 \text{ }\mu\text{m}$) can be estimated from $V = gr^2/9\nu$ (Batchelor, 1967, p.368), where $g = 9.8 \text{ m s}^{-2}$ is the acceleration due to gravity, $r = 450 \text{ }\mu\text{m}$ is the bubble radius, and $\nu = 1 \times 10^{-6} \text{ m}^2 \text{ s}^{-1}$ is the kinematic viscosity. With these values the rise velocity of the small bubbles is estimated to be 22.05 cm s^{-1} . For the large bubbles, with an equivalent diameter $> 1.3 \text{ mm}$, a good approximate equation for the rise velocity in pure water is (Clift et al., 1978, p. 172)

$$V = (2.14 \gamma/\rho d + 0.505gd)^{1/2},$$

where $\gamma = 72 \text{ mN m}^{-1}$ is the surface tension, $d = 12 \text{ mm}$ is the bubble diameter, $\rho = 1000 \text{ kg m}^{-3}$ is the water density. With these values the rise velocity of the large bubbles is 26.9 cm s^{-1} , see also Figure 2.7. Since the water used for the measurements was not

purified, more appropriate value for the rise velocity is about 22 cm s^{-1} , which can be taken from the curve for contaminated water in Figure 2.7. Considering that the small bubbles would penetrate deeper than the large bubbles, the maximum and minimum penetration depths can be used to calculate the residence time of the small and large bubbles, $t = \text{depth}/\text{rise velocity}$. For these depths let chose the values for wind speed of 13 m s^{-1} , water temperature 20°C in Table 6.4: $d_{\min} = 3.81 \text{ cm}$ and $d_{\max} = 18.288 \text{ cm}$. Then the residence time for small bubbles is about 830 ms, and for large bubbles is approximately 170 ms, i.e. the small bubbles live in the water 5 times longer than the large ones.

Are these times enough long in order for gas diffusion to take place. Levich (1962) gives the time necessary for a steady diffusive exchange process to be established across the bubble wall by a time

$$t \approx (vr)^{2/3} / (U^{4/3} D^{1/3}),$$

where d is the bubble radius ($450 \text{ }\mu\text{m}$ or 6 mm), ν is the kinematic viscosity, $D = 1 \times 10^{-9} \text{ m}^2 \text{ s}^{-1}$ is the molecular diffusivity, U is the mean flow velocity taken here to be the initial horizontal velocity of the cloud (Figure 6.12) $U = 0.6 \text{ m s}^{-1}$. Then the for small bubbles steady diffusion is established after 1.8 ms, and for large bubbles after 10 ms. Both these times are much less than the residence times of the small and large bubbles, therefore all bubbles will participate in the gas exchange during their residence time.

As the gas exchange occurs on the bubble walls, it is necessary to estimate what is the contribution of area from the small and large bubbles. Again from the

measured distributions (Figure 6.33a), the number of bubbles with radius up to $450\text{ }\mu\text{m}$ (small bubbles) in a cubic meter is $N = 252\text{ }\mu\text{m}^{-1}\text{ m}^{-3}$, and the number of bubbles with radius in the band $4.275\text{ to }4.5\text{ m}$ (large bubbles) in a cubic meter is $N = 7\text{ }\mu\text{m}^{-1}\text{ m}^{-3}$. The total area provided from the small bubbles is $4\pi r^2 N = 6.41 \times 10^{-4}\text{ m}^2$ while the area from the large bubbles is $1.78 \times 10^{-3}\text{ m}^2$. Or, the area provided by a few large bubbles is about 3 times more than that provided by 252 small bubbles. Taking both, the residence time and the area provided by the bubbles, it can be stated that the gaseous flux provided by the small bubbles is enhanced 3 times simply by the presence of large bubbles. The enhancement is valid for about 1/5 of the cloud lifetime.

Using the bubble size distributions calculated by the measured void fraction (the solid lines in Figure 6.34c), similar estimation shows that the area provided for gas exchange by $\approx 3 \times 10^8$ bubbles with radius $100\text{ }\mu\text{m}$ is about 43 m^2 , and the area from 2156 bubbles with radius 2 mm is 0.1 m^2 . It can be generalized, therefore, that during the one second active lifetime of bubble clouds with high void fraction (about 60% in average) the gas exchange due to background bubble population is due to two factors: 1) the presence of a huge amount of small bubbles, and 2) the presence of large bubbles.

6.6 Summary

This chapter reports the experimental results on bubble cloud characteristics at various wind conditions (9 - 16 m s⁻¹) and at different water temperatures (13, 20, and 27°C) obtained with a photographic technique. The experimental equipment, conditions and the procedures for processing the data are described in detail. The wave characteristics are also obtained from wave gauge measurements in order to scale the bubble clouds parameters – length, l , penetration depth, d , width, w , and void fraction α .

Temporal and spatial evolutions of the bubble clouds dimensions and void fraction are extracted from 15-minutes video records from both side and top views. Probability density functions and generalizing values for a given wind speed for each bubble cloud parameter are calculated. Insights for the observable values that bubble clouds can assume are gained from these. Wind dependence of the cloud characteristics is found to follow power law with general trend of increasing the cloud dimensions with wind. Time averaged values for void fraction remain constant within steadily increasing cloud volume.

The temperature of the water is weakly revealed from time and space evolution of the cloud parameters and their statistical variables (PDFs and mean values). With increasing the water temperature a slight enhancement of the cloud parameters and lifetime are observed. The temperature dependence of the cloud characteristics is easily masked by the stronger influence of the wind generated wave field.

Individual bubble within the bubble cloud are observed in close view and bubble size distributions for different wind speeds are obtained. The initially generated bubbles cover a size range up to 10 mm in diameter. The size distribution follows d^{-2} law and is well compared with other measurements. The possibility of obtaining bubble size distribution from photographically measured void fraction is considered. The calculated size distributions are compared with the actually measured values and the results are encouraging.

The results obtained in this study are favorably compared with other laboratory and field data. Some implications of the results in determining the mixing layer and gas exchange in ocean are considered.